Volume 5
Number 19
7 October 2023
Pages 5157–5416

Nanoscale Advances

rsc.li/nanoscale-advances

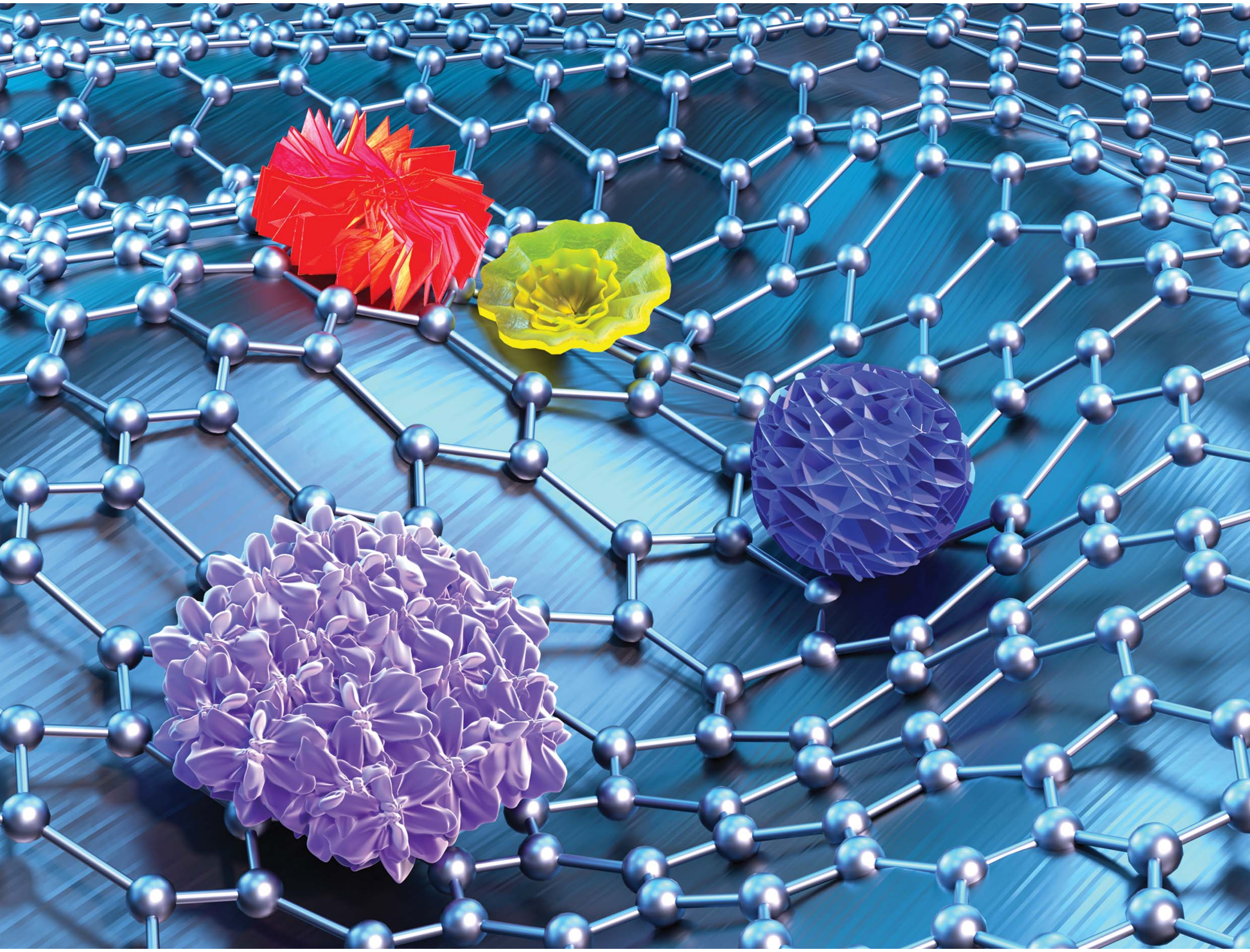

ISSN 2516-0230

ROYAL SOCIETY OF CHEMISTRY

REVIEW ARTICLE
Hongje Jang, Do Nam Lee *et al.*
Recent advances in nanoflowers: compositional and structural diversification for potential applications

NCNST

Nanoscale
Advances

REVIEW

View Article Online
View Journal | View Issue

Check for updates

Cite this: *Nanoscale Adv.*, 2023, **5**, 5165

Recent advances in nanoflowers: compositional and structural diversification for potential applications

Su Jung Lee,[a] Hongje Jang *[b] and Do Nam Lee *[a]

In recent years, nanoscience and nanotechnology have emerged as promising fields in materials science. Spectroscopic techniques like scanning tunneling microscopy and atomic force microscopy have revolutionized the characterization, manipulation, and size control of nanomaterials, enabling the creation of diverse materials such as fullerenes, graphene, nanotubes, nanofibers, nanorods, nanowires, nanoparticles, nanocones, and nanosheets. Among these nanomaterials, there has been considerable interest in flower-shaped hierarchical 3D nanostructures, known as nanoflowers. These structures offer advantages like a higher surface-to-volume ratio compared to spherical nanoparticles, cost-effectiveness, and environmentally friendly preparation methods. Researchers have explored various applications of 3D nanostructures with unique morphologies derived from different nanoflowers. The nanoflowers are classified as organic, inorganic and hybrid, and the hybrids are a combination thereof, and most research studies of the nanoflowers have been focused on biomedical applications. Intriguingly, among them, inorganic nanoflowers have been studied extensively in various areas, such as electro, photo, and chemical catalysis, sensors, supercapacitors, and batteries, owing to their high catalytic efficiency and optical characteristics, which arise from their composition, crystal structure, and local surface plasmon resonance (LSPR). Despite the significant interest in inorganic nanoflowers, comprehensive reviews on this topic have been scarce until now. This is the first review focusing on inorganic nanoflowers for applications in electro, photo, and chemical catalysts, sensors, supercapacitors, and batteries. Since the early 2000s, more than 350 papers have been published on this topic with many ongoing research projects. This review categorizes the reported inorganic nanoflowers into four groups based on their composition and structure: metal, metal oxide, alloy, and other nanoflowers, including silica, metal–metal oxide, core–shell, doped, coated, nitride, sulfide, phosphide,

Received 14th March 2023
Accepted 2nd August 2023

DOI: 10.1039/d3na00163f

rsc.li/nanoscale-advances

---

[a] *Ingenium College of Liberal Arts (Chemistry), Kwangwoon University, Seoul 01897, Korea. E-mail: donamlee@hanmail.net*

[b] *Department of Chemistry, Kwangwoon University, Seoul 01897, Korea. E-mail: hjang@kw.ac.kr*

Su Jung Lee received her PhD degree in Chemistry from Yonsei University, South Korea in 2015. She pursues her research work at Ingenium College of Liberal Arts (Chemistry), Kwangwoon University, Korea under the supervision of Prof. D. N. Lee. Her research focus is design and synthesis of silicon-based nanomaterials and its applications: optical materials for display and solar cells, and anti-bacterial and anti-cancer materials for biomedical application.

Hongje Jang is an Associate Professor in the Department of Chemistry at Kwangwoon University in the Republic of Korea. During his postdoctoral research in laser dynamics systems in nanomaterials at the Georgia Institute of Technology, he worked on real-time in vitro autophagy tracking platforms. His current research at KWU focuses on the design and synthesis of metal or metal oxide nanoparticles by controlling their size, morphology, and compositions. Expanding on this, he focuses on the precise physicochemical property control of nanosystems.

selenide, and telluride nanoflowers. The review thoroughly discusses the preparation methods, conditions for morphology and size control, mechanisms, characteristics, and potential applications of these nanoflowers, aiming to facilitate future research and promote highly effective and synergistic applications in various fields.

1. Introduction

Dr Richard Feynman introduced the idea and concepts of nanotechnology in his talk titled "There's Plenty of Room at the Bottom" at the American Physical Society's annual meeting in 1959, initiating the exploration of nanoscience and nanotechnology as new materials-science fields.[1] In the 1980s, various spectroscopic techniques, such as scanning tunneling microscopy (STM)[2–4] and atomic force microscopy (AFM),[5,6] were developed for the characterization and tuning of nanomaterials, facilitating the investigation of various types of nanomaterials, such as fullerenes,[7,8] graphene,[9,10] nanotubes,[11,12] nanofibers,[13,14] nanorods,[15,16] nanowires,[17,18] nanoparticles,[19,20] nanocones,[21,22] and nanosheets.[23,24] Recently, the applications of these nanomaterials have expanded to encompass a wide range of commercial fields, including electronics, energy-related fields, cosmetics, and biomedicine.[25]

Among them, flower-shaped hierarchical 3D nanostructures, called nanoflowers,[26] have attracted immense attention because of their higher surface-to-volume ratio compared to that of spherical nanoparticles, along with their low cost and eco-friendly preparation methods. Additionally, they enhance the stability of many catalytic reactions by the immobilization of enzymes and proteins.[27–31] Numerous publications report the potential utilities of these 3D nanostructures with peculiar morphologies, which are fundamentally based on nanoflowers. As we have explained in the previous paper, nanoflowers can be classified according to their compositions: inorganic, organic, and organic–inorganic hybrid.[32] First, inorganic nanoflowers are defined as being composed only of inorganic materials such as metals, metal oxides, alloys, and metalloids.[33–36] In addition, as introduced later in this paper, metalloid, carbon, nitride, sulfide, phosphide, selenide, and telluride coated or doped inorganic materials are also defined as inorganic nanoflowers.[37–44] Second, nanostructures that include inorganic elements as part of a medium composed of only organic molecules or in which organic molecules are the main components are called organic nanoflowers.[45–47] Reported findings have indicated that organic nanoflowers, characterized by an open structure, provide a greater number of accessible active sites and enable easy movement of ions.[48] Additionally, the intersecting extended nanopetals within these structures promote the efficient transportation of electrons. These nanoflowers have demonstrated promising outcomes in applications related to energy storage and electrocatalysis.[48,49] For example, one-pot synthesis of polyacrylonitrile (PACN) and its copolymer nanostructured particles with various superstructures (flower, pompom, hairy leave, and petal shapes) has been reported. PACN flowers (PACN-F) are prepared with acrylonitrile monomer (ACN) in acetone through free radical polymerization initiated by azobis(isobutyronitrile) (AIBN). Through stabilization and carbonization steps, these PACN flowers are converted to carbon flowers. The morphology is controlled by the incorporation of different co-monomers or by employing various solvents. These carbon flower materials may be applied as promising candidates for various energy, environment, or electronic applications.[48] Zheng's group introduced nitrogen, phosphorus, and fluorine doped carbon NFs (NPF@CNFs) by ultrasound-induced polycondensation and pyrolysis. The synthesized NPF@CNF exhibited enhanced activity ($E_{1/2}$ = 0.85 V (oxygen reduction reaction, ORR), $E_{j=10}$ = 1.56 V (oxygen evolution reaction, OER) *vs.* RHE) and cycling stability (retention above 90% after cycling for 50 000 s) as a bifunctional electrocatalyst toward the ORR and OER during the discharging and charging process of zinc–air batteries, which is even superior to those of commercial Pt/Ir-based catalysts.[50] Third, hybrid nanoflowers are described as all components of inorganic nanostructures associated with organic materials.[51] Hybrid nanoflowers, which combine biomolecules and inorganic components, have found extensive applications in biosensors, bioassays, biocatalysis, biomedicine, and diagnostics.[52–55] This is attributed to their straightforward synthesis, remarkable effectiveness, and ability to improve enzyme stability.[52] The fabrication process of hybrid organic–inorganic nanoflowers under mild conditions involves utilizing copper(II) ions as the inorganic element and natural amino acids as the organic element. Asparagine (Asn)-incorporated nanoflowers with diameters in the range of 10–15 μm closely resemble the shape of Dahlia in nature and have hierarchical structures with high surface-to-volume ratios. The nanoflowers have a Brunauer–Emmett–Teller (BET) surface area of 32.0 m^2 g^{-1} and an average pore size of 112.5 nm. The nanoflowers incorporating amino acids exhibit catalytic activity based on a reaction principle like Fenton's reagents. The presence of copper ions enables self-

Do Nam Lee received her B.S. and M.S. in chemistry from Yonsei University in South Korea. She earned her PhD from the same university in 1992 under the supervision of Prof. Chang Whan Kim and completed postdoctoral research as a member of the group of Prof. Robert West at University of Wisconsin–Madison, USA. She worked as a visiting scholar at Peking University, China in 2003. She is currently an associate professor at Kwangwoon University in South Korea and is mostly focusing on research of functional metal–organic frameworks, nanoflowers, and drug delivery.

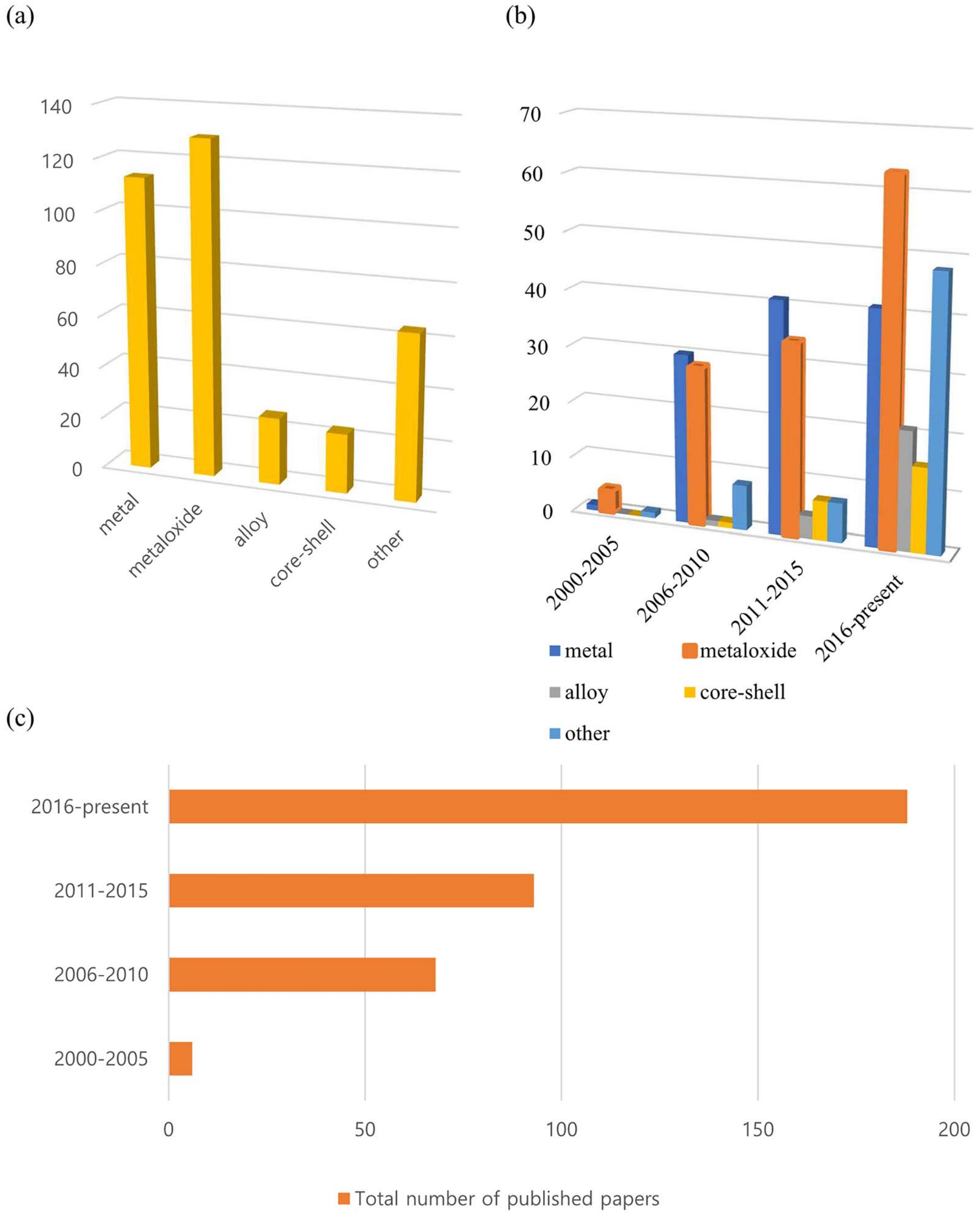

Fig. 1 Publications on flower-shaped nanostructures since 2000. (a) The number of articles, categorized by the material composition and structures of the nanostructures reported, (b) the number of such publications in the past 20 years, and (c) the number of papers published on flower-shaped hierarchical 3D nanostructures in the past 20 years.

assembly between amino acids and copper phosphate, resulting in intrinsic peroxidase-like activity in the amino acid-incorporated nanoflowers. These amino acid–inorganic hybrid nanoflowers are expected to have significant applications in biosensors, bioanalytical devices, pharmaceuticals, and industrial biocatalysis.[56] In particular, inorganic nanoflowers are attracting researchers' attention because of their catalytic efficiency and optical characteristics, depending on the composition, crystal structure, and local surface plasmon resonance (LSPR).[32] Thanks to these properties, inorganic nanoflowers are widely used in electro, photo, and chemical catalysts, sensors, supercapacitors and batteries. Moreover, in the synthesis of inorganic nanoflowers, as will be discussed in detail later, the availability of diverse synthesis methods and the ability to regulate reaction conditions make it easier to achieve precise control of form and composition. However, there have been very few reviews of inorganic nanoflowers, and this is the first review of inorganic nanoflowers for catalyst, sensor, supercapacitor, and battery applications.

To the best of our knowledge, more than 350 such reports on inorganic nanoflowers have been published since the early 2000s, with an increasing number of studies being published currently. As shown in Fig. 1, many of the published papers are on metal and metal oxide nanoflowers, with the number of papers on metal oxides increasing rapidly. Additionally, numerous studies on alloys, core–shell structures, doped systems, and so on, have been published recently. They investigate the preparation method, morphology, size-control conditions, characteristics, and potential applications of nanoflowers composed of metals, metal oxides, alloys, core–shell, and doped systems. Recent research has primarily focused on optimizing their morphologies and composition ratios for practical applications.

In this review, nanoflowers have been categorized as metal, metal oxide, alloy, and other nanoflowers, depending on their compositions. Synthetic methodologies, experimental parameters' effects on the morphology and size, mechanisms, physical, chemical, and biological properties derived from the physical properties of inorganic materials, synergistic effects among composition ratios, morphologies, and structural effects, with regard to potential applications as photocatalysts,[57] electrocatalysts,[58] anode materials for lithium-ion storage,[59] supercapacitor electrodes,[60] and gas sensors[61] are primarily considered.

2. Methods for preparing nanoflowers

Continuous research efforts have been made to develop new synthesis methods for the nanoflowers.[62–66] According to Kulkarni's book: Nanotechnology: Principles and Practices, nanomaterials are prepared by four types of methods, namely, physical, chemical, biological, and hybrid.[67] The preparation of inorganic nanoflowers also uses the same or modified technology as the conventional nanomaterial synthesis technology, as depicted in Fig. 2.

First, the physical technique is mainly represented by physical vapour deposition in the inorganic nanoflower synthesis. For example, Bi_2S_3 nanoflowers are prepared on a Si substrate *via* a simple vapour deposition method.[68] The morphology of the Bi_2S_3 nanoflowers is modulated by tuning the partial pressure of the reactant. The second technology is the chemical synthesis method, such as hydrothermal,[69] solvothermal,[70] sonochemical,[35] colloids,[71] sol–gel[72] and microwave synthesis.[73] TiO_2 nanoflowers are synthesized by a hydrothermal method.[74] The solvothermal reaction is used to synthesize Pd nanoflowers in the presence of oleic acid.[75] IrCo and IrNi nanoflowers are ultrasonicated with $IrCl_3 \cdot xH_2O$, $Co(acac)_2$ or Ni(acac) and oleylamine and heated in a hot oil bath.[35] Hierarchical $NiCo_2O_4$ nanoflowers are synthesized using the microwave synthesis method.[73] Third, the biological strategy is an environmentally benign and biomimetic approach using natural material extracts, such as *Kalanchoe daigremontiana*,[76] *Dodonaea angustifolia*,[77] *Ocimum sanctum* (*Tulsi*) leaves,[78] and *Azadirachta indica* leaves,[79] without utilizing any toxic materials.

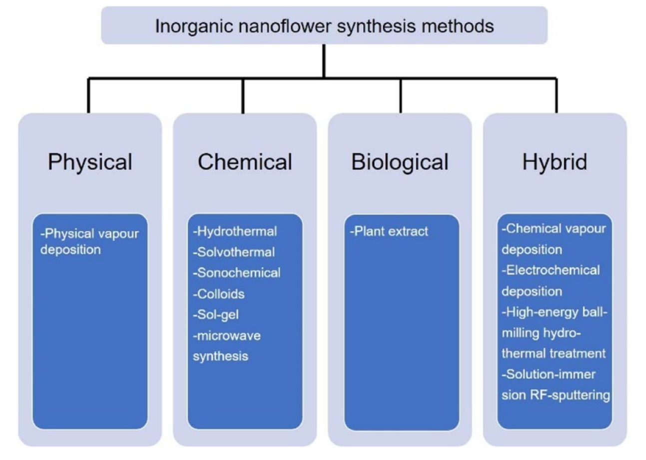

Fig. 2 Commonly used synthesis technology of inorganic nanoflowers: physical, chemical, biological, and hybrid.

The last synthesis technology is the hybrid synthesis strategy that combines physical, chemical, and biological methods: chemical vapour[80] and electrochemical[81] deposition, high energy ball-milling hydrothermal treatment,[60] and the solution-immersion RF-sputtering method.[82]

As we introduced above, inorganic nanoflower synthesis can utilize various techniques and methods. This can be used differently depending on the material and application of the nanoflower to be synthesized. We will illustrate some commonly used nanoflower synthesis methods with examples for each.

2.1. Physical method

2.1.1. Physical vapor deposition. Physical vapor deposition (PVD) is a process used to deposit thin films and coatings of nanomaterials onto a substrate. The PVD method is useful to prepare metal- and metal oxide- based nanomaterials.[68,83] However, only a few studies on nanoflower synthesis through the PVD method have been reported so far, mainly due to the high cost and elevated reaction temperatures. The controlled growth of nanoflowers using PVD techniques is an area that holds great promise and potential for further exploration.

For instance, Yu *et al.* have described a vapor deposition technique for the synthesis of exquisite Bi_2S_3 nanoflowers on a silicon substrate.[68] The researchers utilize a horizontal tube furnace for the vapor deposition process. Bi_2S_3 powder and S powder are used as the starting materials. In the furnace tube, a ceramic boat containing Bi_2S_3 powder is positioned at the center, while sulfur powder is placed between the Bi_2S_3 and the gas inlet. Silicon wafers are positioned downstream, a few centimeters away from the Bi_2S_3 powder. The tube is tightly sealed and flushed with high purity argon gas. The temperature is then gradually increased to 650 °C at a heating rate of 8 °C min^{-1} and maintained at that temperature for 2 hours. Subsequently, the temperature is gradually decreased to room temperature. Throughout the thermal treatment, argon gas is continuously allowed to flow at approximately 100 sccm (standard cubic centimeter per minute) to provide both protection and carrier gas functions. Additionally, they have demonstrated the ability to adjust the shape of the Bi_2S_3 nanostructures, ranging from flower-like structures to bundles of nanorods, by controlling the partial pressure of the reactants.

Table 1 Nanoflowers are synthesized by a hydrothermal process under diverse reaction conditions

Nanostructure/morphology	Size	Reaction conditions	Time and temperature in the autoclave	Surfactant or template	Ref.
TiO_2 nanoflowers on a Ti substrate	360–420 nm	10 mL H_2O_2 (37%) + 60 mL NaOH (1 M)	5 h, 120 ± 2 °C	—	92
Anatase and brookite TiO_2 nanoflowers	—	7.8 mL tetrabutyl titanate (TBOT) + 1.10 g NaCl + 68 mL aqueous $NH_3 \cdot H_2O$	24 h, 180 °C	—	93
ZnO nanoflowers	3 µm	0.549 g, $C_4H_6O_4Zn \cdot 2H_2O$ (2.5 mmol) + 0.735 g, sodium citrate (2.5 mmol)+ 4 mL NaOH (4.0 M)	8 h, 120 °C	—	94
ZnO nanoflowers	4 µm	($Zn(CH_3COOH)_2$_$2H_2O$) + (1 mM) + NaOH (10 mM)	8 h, 140 °C	PEG-20000	95
Porous NiO nanoflowers	15.0 (PEG), 16.7 (PVP) nm	2.9080 g of $Ni(NO_3)_2 \cdot 6H_2O$ or 2.4884 g of $Ni(CH_3COO)_2 \cdot 4H_2O$ + HMTA solution (0.5 M)	6 h, 110 °C	PEG, PVP	96
Sparse-type and close-type NiO nanoflowers	5 (CTAB), 2 (SDS) µm	0.475 g $NiCl_2 \cdot 6H_2O$ + 0.300 g urea	8 h, 160 °C	CTAB, SDS	97
CuO nanoflowers	1 µm	6 mL $NH_3 \cdot H_2O$ (1 M) + 10 mL $Cu(NO_3)_2$ (0.01 M)	6 h, 100 °C	—	98
Flower-like CuO nanostructures with porous nanosheets on the alumina tube	—	0.3 M $Cu(CH_3COO)_2 \cdot H_2O$ + 25 mL $NH_3 \cdot H_2O$ (17 M) + 1.0 g NaOH	24 h, 180 °C	—	99

There is a need for research aimed at exploring novel methods and improving existing PVD approaches to achieve precise control over the formation and arrangement of nanoflowers. This involves investigating various parameters such as deposition conditions, precursor materials, and substrate properties to optimize PVD processes specifically tailored for nanoflower growth.

2.2. Chemical method

2.2.1. Hydrothermal and solvothermal methods. The hydrothermal method is one of the most well-known and widely employed methods for the synthesis of diverse nanostructured materials, including nanoflowers. This method is simple, cost-effective, eco-friendly, and easily controllable.[84,85] These characteristics make it highly advantageous for the large-scale synthesis of nanoflowers. The precise control of temperature and pressure in the hydrothermal process enables the formation of hierarchical 3D nanostructures with isotropic growth in all directions. Moreover, facile manipulation of reaction parameters such as composition and concentration of precursors and reducing agents and the reaction time, and the ability to adjust the presence or type of templates or surfactants enable precise control over the morphology and size of the nanoflowers (Table 1). However, it is important to address the aggregation tendency of nanomaterials, as it can negatively impact the uniform distribution and morphology of the resulting structure.[84,85] The solvothermal method is similar to the hydrothermal method, with the only distinction being that it is conducted in a non-aqueous medium (Table 2).

For instance, in the first step, 5 mM of $Cu(NO_3)_2 \cdot 3H_2O$ powder is dissolved in 100 mL of deionized water. In the second

Table 2 Nanoflowers are synthesized by a solvothermal process under diverse reaction conditions

Nanostructure/morphology	Size	Reaction conditions	Time and temperature in the autoclave	Surfactant or template	Ref.
TiO_2 nanoflowers	47.56–274.36 nm	NaOH (0.024 M) + 8 mL $TiCl_3$ + 60 mL ethanol	18 h, 130 °C	—	34
Porous NiO nanoflowers	—	0.5 g $Ni(ac)_2 \cdot 4H_2O$ + 0.25 g urea + 30 mL ethanol	3–24 h, 190 °C	—	100
Zn-doped CuS nanoflowers	1 µm	0.25 mmol CuCl + 0.25 mmol $Zn(Ac)_2 \cdot 2H_2O$ + 0.75 mmol S powder + 15 mL ethanol	24 h, 180 °C	—	101
Mo-doped Bi_2Se_3 nanoflowers	100–200 nm	0.85 mmol $Bi(NO_3)_3 \cdot 5H_2O$ + 0.15 mmol $(NH_4)_6Mo_7O_{24} \cdot 4H_2O$+ 18 mL *N*,*N*-dimethylformamide + ammonia + Se powder + Na_2SO_3	20 h, 160 °C	—	102
$Bi_2O_{2.33}$ nanoflowers	—	0.11 g $NaBiO_3$ + 20 mL ethanol, + 5.0 mL distilled water + 2.0 mL 1 M HNO_3 solution	3–5 h, 100 °C	PVP	103

step, a 1 mM aqueous solution of hexamethylenetetramine is mixed with 100 mL of deionized water. In the third step, the solutions from steps 1 and 2 are combined and 1 mL of 30% NaOH is added. The resulting solution is continuously stirred for 60 minutes at room temperature. Subsequently, the suspended mixture is transferred into an autoclave and securely sealed. The autoclave is then placed in an oven and maintained at 110 °C for 3 hours. After completing the entire process and allowing the oven to cool to room temperature, the resulting solution is centrifuged and washed with deionized water. Finally, the product, characterized by its black color (CuO nanoflowers), is obtained after drying in a vacuum oven at 60 °C for 2 hours.[86]

In recent studies, it has been frequently reported that a combination of the hydrothermal method with other synthesis techniques is employed to synthesize nanoflowers with diverse structures. Qu *et al.* reported a novel approach for the controlled synthesis of three types of 3D fluffy ZnO nanoflowers with distinct nanostructures. This method involves a simple ultrasonic treatment followed by a hydrothermal process.[87] One type, denoted as ZnO-0, is directly formed through the hydrothermal reaction without prior ultrasonic treatment, resulting in smooth edges. The other two types, namely ZnO-250 and ZnO-950, are obtained by subjecting the samples to ultrasonic treatment at 250 W and 950 W, respectively, prior to the hydrothermal process, resulting in jagged margins. The experimental findings revealed that increasing the intensity of ultrasonic treatment leads to a decrease in the size, specific surface area, crystallite dimension, intrinsic donor defects, and the signals of reactive radicals in the ZnO nanoflowers.

2.2.2. Colloidal synthesis. Colloidal synthesis offers the advantage of combined control over the morphology and composition of nanoflowers, making it a relatively inexpensive and scalable method. To demonstrate, the synthesis of $M_{1-x}W_xSe_2$ nanoflowers with precise control over both composition and morphology is demonstrated through the utilization of colloidal synthesis.[71] Interestingly, a wide range of nanoflowers with diverse compositions and complex structures: $MoSe_2$,[88] Ru-doped $MoSe_2$,[89] homogeneously Co-doped and Co-edge doped $MoSe_2$,[90] and Au nanoparticles decorated Bi_2Se_3 (ref. 91) nanoflowers have been synthesized through colloidal synthesis methods.

Here is an overview of the experimental procedure for synthesizing $MoSe_2$ nanoflowers using the colloidal method: in a 100 mL three-neck flask, a mixture of 20 mg (0.1 mmol) of Na_2MoO_4, 8 mL of oleic acid, and 2 mL of 1-octylamine is prepared and degassed under vacuum at 120 °C for approximately 10 minutes. The reaction vessel is then purged with Ar(g) and slowly heated to around 240 °C at a rate of approximately 5 °C per minute, resulting in the formation of a clear, dark, red-brown solution. Subsequently, 2 mL of the ODE-Se stock solution (0.1 M), which is 1-octadecene and Se solution, is continuously injected at a rate of 0.1 mL min^{-1} using a syringe pump. After the injection is completed, the solution is aged for an additional 30 minutes at a final temperature of approximately 300 °C. The reaction mixture is then rapidly cooled by removing the flask from the heating mantle. The resulting $MoSe_2$ particles are precipitated by adding 10 mL of toluene and 10 mL of ethanol, followed by centrifugation. The black precipitate is washed three times using a 1 : 1 mixture of toluene and ethanol (with centrifugation steps in between washes), and finally suspended in ethanol to form a dark purple colloidal suspension.[88]

2.2.3. Microwave synthesis. The microwave synthesis method offers notable advantages due to its rapidity, simplicity, environmental friendliness, and cost-effectiveness.[104] To the best of our knowledge, microwave reactions are utilized for producing various nanoflowers based on Ni through the interaction of molecules, which is facilitated by localized indirect heating within the solution.[73,105,106]

For example, 40 mmol of $Ni(NO_3)_2\cdot 6H_2O$ is dissolved in 50 mL of distilled water. Subsequently, 5 wt% of the cationic surfactant cetyltrimethyl ammonium bromide (CTAB) is added, and then 3 mL of ammonia is introduced into the solution. The resulting solution is stirred for 10 minutes. The solution, contained within a polypropylene-capped autoclave container, is subjected to microwave irradiation at a power of 300 watts for a duration of 15 minutes. The green precipitates obtained are washed multiple times with distilled water and ethanol to eliminate soluble impurities. Subsequently, the precipitates are dried in a hot oven at 80 °C for 12 hours to obtain $Ni(OH)_2$ samples. The as-prepared powder samples are then subjected to calcination in air at 400 °C for 2 hours to yield NiO nanoflowers.[105] The researcher also employed a hydrothermal method using the same amount of precursor, surfactant, and ammonia, with the reaction conducted at 140 °C for 15 minutes. In scanning electron microscopy (SEM) analysis, the microwave treatment process results in the formation of nanostructures that exhibit the same flower-like morphologies but with a higher degree of agglomeration compared to the samples grown through the hydrothermal method. This can be attributed to the indirect heating of molecules through microwave radiation.[105]

2.3. Biological method

2.3.1. Green synthesis. Green synthesis, also known as biosynthesis, of metal nanoparticles using plants, herbs, or microorganisms has garnered significant attention,[107] particularly in the field of medicine. The use of plant extracts for the production of metal nanoparticles has gained popularity due to its straightforward, scalable, and non-toxic method.[76] However, it should be noted that the synthesis of nanoflowers using this method is currently in its nascent stages, with only a scant number of research papers dedicated to this particular approach.

Ag nanoflowers are obtained using natural materials extract: *Kalanchoe daigremontiana*, as a natural reducing agent.[76] The green synthesis of nanospindles of CuO and their subsequent assembly into nanoflowers has been successfully achieved by modifying the solvents used, such as water and ethanol, in combination with the extract obtained from *Dodonaea angustifolia*.[77] Also, CuO nanoflowers are synthesized using eugenol (4-allyl-2-methoxyphenol), which is extracted from the leaves of *Ocimum sanctum* (*Tulsi*), serving as a natural reducing agent.[78] A simple, environmentally friendly, biomimetic method is employed to fabricate Au/ZnO hybrid nanoflowers using *Azadirachta indica* (neem) leaf extract as both a reducing agent and a capping agent.[79]

Upon closer examination of one of these methods, the synthesis of ZnO nanoflowers has been achieved by employing *Withania coagulans* extract as a reducing agent. For the synthesis of ZnO nanoflowers, a solution is prepared by dissolving 0.2 g of zinc acetate in 50 mL of distilled water. The pH of the solution is adjusted to 12 using a 2 M solution of NaOH. Subsequently, 5 mL of *Withania coagulans* plant extract is added to the solution, which is then heated at 90 °C for 5 hours with continuous stirring. To obtain the final product, the reaction mixture is subjected to centrifugation at 6000 rpm for 15 minutes. The resulting ZnO nanoflowers are collected and further incubated at 37 °C overnight.[108]

2.4. Hybrid method

2.4.1. Electrochemical deposition. Electrochemical deposition is a highly popular technique employed for the synthesis of nanoflowers. Synthesis by electrochemical deposition has been recognized as a potentially superior method compared to other techniques due to its advantageous features. These include: (1) the capability of being performed in a single step at room temperature, resulting in reduced process time; (2) effective control over the size and shape of the particles, leading to the formation of uniform deposits with high purity; (3) ease of securely anchoring the particles onto the substrate; (4) environmentally friendly characteristics.[109,110]

A simple and reproducible technique for producing 3D Pt nanostructures on silicon substrates has been reported at ambient temperature using potentiostatic pulse plating.[111] An aqueous solution containing 1 M H_2PtCl_6 and 1 M H_2SO_4 is mixed and stirred for 5 hours at room temperature. The Pt catalyst is then electrodeposited onto a flat silicon substrate using potentiostatic pulse plating in a three-electrode cell system with a saturated calomel reference electrode (SCE). The positive potential pulse (+0.05 V) lasted for 5 ms, while the negative potential pulse (−0.02 V) lasted for 1 ms. This bipolar pulse electrodeposition method facilitates the synthesis of 3D Pt nanoflowers on the Si substrate. Following Pt electrodeposition, the sample is washed with deionized (DI) water to remove surface contamination and dried under ambient conditions.

Also, the galvanic replacement method is used to create monomorphic single-crystalline Pt nanoflowers by transforming Te nanowires into a fully-formed Pt nanostructure.[112] The template-free ultrasonic electrodeposition method is employed to produce Pt nanoflowers directly on the bare Au electrodes.[110] This method is utilized for synthesizing not only Pt nanoflowers but also Ag, Pd, AuPt, and AuAgCu nanoflowers.[113–116]

2.4.2. Multi-step synthesis for complex structures. With the increasing diversity of composition and complexity in nanoflower structures, there have been reports of employing a combination of various synthesis methods to fabricate them. Zhao *et al.* reported the synthesis of Ag@NiO core–shell nanoflower arrays through a one-step solution-immersion process followed by the RF-sputtering method.[82] In the initial stage, the bulk ilmenite $FeTiO_3$ undergoes ball-milling, followed by a mild hydrothermal treatment in an aqueous NaOH solution. This process leads to the formation of nanostructured $FeTiO_3$, which exhibits a distinctive nanoflower morphology.[60] MnO_4 nanoflowers are fabricated utilizing a microwave-assisted hydrothermal synthesis under alkaline conditions.[117]

3. Experimental parameters' effect

The morphology of nanoflowers plays a crucial role in various applications and scientific studies. The unique and intricate structures of nanoflowers offer distinct advantages: a large surface area-to-volume ratio and enhanced catalytic properties. By understanding the morphology and controlling the growth conditions and parameters, researchers can manipulate the size, shape, and arrangement of nanoflower structures, leading to improved performance in sensing devices, energy storage systems, drug delivery platforms, and more. Here, we aim to introduce how various experimental conditions can influence the size and shape of nanoflowers, using several examples.

Porous nanoflower- and nanourchin-like structures are synthesized using the hydrothermal method, employing either hexamethylenetetramine (HMTA) or urea as a precipitant, with or without the addition of surfactants such as poly(ethylene glycol) (PEG) or poly(vinyl pyrrolidone)(PVP).[96] Based on the information provided in Table 3, it can be observed that NiO precursors synthesized using HMTA as a precipitant exhibited a morphology resembling nanoflowers, while those prepared with urea as a precipitant displayed a shape similar to that of nanourchins. NiO-HMTA, NiO-HMTA-PEG, NiO-HMTA-PVP, and NiO-urea samples exhibit a high surface area ranging from 31 to 66 $m^2\ g^{-1}$. Also, NiO-HMTA-PVP possesses the highest BET surface area and pore volume. As a highly active catalyst, NiO-HMTA-PVP exhibits the highest surface area, highest concentration of oxygen adspecies (O_{ads}), and the best reducibility. It demonstrates superior catalytic performance with a $T_{50\%}$ of 253 °C and $T_{90\%}$ of 266 °C.[96]

Sparse-type and close-type NiO nanoflowers are successfully synthesized using a hydrothermal process with the assistance of CTAB and sodium dodecyl sulfate (SDS) as surfactants, respectively. The performance of the close-type NiO nanoflowers is found to be superior, and this can be attributed to several factors. Firstly, the close-type nanoflower architecture exhibits a higher degree of porosity and compactness. Additionally, there are more nanojunctions between adjacent nanosheets, creating a well-connected structure. Furthermore, the ultrathin nanosheets assemble abundant micro reaction rooms. Finally, the thickness of the petal structures is smaller than twice the Debye length.[97]

In another study, in the hydrothermal synthesis, nanorods and nanoneedles assembled NiO nanoflowers are synthesized using different surfactants, namely CTAB and ethylene glycol (EG), respectively. Based on TEA and SEM analysis, it is determined that the nanorods have an average diameter of approximately 900 nm and a length of approximately 6 μm. On the

Table 3 Preparation parameters, crystal phases, crystallite sizes, morphologies, BET surface areas, average pore sizes, and pore volumes of the as-prepared NiO samples. Reprinted with permission from ref. 96. Copyright © 2012 Elsevier B.V. All rights reserved

Sample code	Precipitating agent	Ni/precipitating agent molar ratio	Surfactant	Crystal phase	Crystallite size[a] (nm)	Morphology	BET surface area ($m^2 g^{-1}$)	Average pore size (nm)	Pore volume ($cm^3 g^{-1}$)
NiO-HMTA	HMTA	1 : 1	—	Cubic	19.1	Irregular nanoflower-like spheres	31.5	26.4	0.202
NiO-HMTA-PEG	HMTA	1 : 1	PEG	Cubic	15.0	Nanoflower-like spheres	56.1	26.2	0.296
NiO-HMTA-PVP	HMTA	1 : 1	PVP	Cubic	16.7	Nanoflower-like spheres	66.3	22.9	0.414
NiO-urea	Urea	1 : 1	—	Cubic	25.2	Nanourchin-like spheres	30.5	9.6	0.103
NiO-bulk	—	—	—	Cubic	78.6	—	5.6	—	—

[a] The crystallite sizes are calculated according to Scherrer's equation using the FWHM of the (200) line of the XRD patterns.

Table 4 Dimensions, band gap and sheet resistance of ZnO nanoflowers synthesized at different times. Reprinted with permission from ref. 119. Copyright © 2019 Elsevier Ltd. All rights reserved

Reaction time (min)	Crystallite size (nm)	Petal width (nm)	Petal length (nm)	Single flower length (nm)	Band-gap energy (eV)	Sheet resistance ($M\Omega\ sq^{-1}$)
05	14.73	288 ± 27	714 ± 81	1523 ± 151	3.21	38.5000
10	22.22	345 ± 45	740 ± 90	1674 ± 180	3.27	18.5000
15	24.11	327 ± 48	772 ± 57	1653 ± 154	3.10	0.01020
30	24.06	370 ± 50	772 ± 85	1785 ± 150	3.28	0.00344

other hand, the nanoneedles exhibit a thicker structure at the roots with sharper emanative ends. Each needle has a length of around 2.5 μm and a diameter of approximately 80 nm at the middle.[118]

Borbón *et al.* conducted a hydrothermal study to examine how the reaction time affects the size and morphology of ZnO nanoflowers. They observe that well-defined flower-like structures are formed within 5 minutes of the reaction. Regardless of the reaction time (10, 15, and 30 minutes), the nanoflowers exhibit similar high-density morphologies. The dimensions of the petals in each nanoflower increase as the crystal growth continued over time, with the nanorods becoming wider and larger (Table 4). However, between 10 and 15 minutes, there is no significant change observed. The research also showed a decrease in sheet resistance from 38.5 $M\Omega\ sq^{-1}$ at 5 minutes to 0.00344 $M\Omega\ sq^{-1}$ at 30 minutes. The reduction in the resistivity of the samples could be attributed to a decrease in crystal defects and an increase in crystallite size as the reaction time increased, as confirmed by XRD results. This suggests that the electrical resistance can be adjusted by varying the reaction time.[119]

A hydrothermal method is employed to synthesize well-defined and uniformly sized spherical mesoporous nanoflowers. The synthesis process involves using a solvent mixture of cyclohexane and water, with cetylpyridinium bromide (CPB) acting as the template, tetraethyl orthosilicate (TEOS) as the source of inorganic silica, and urea as the hydrolysis additive. The study aims to investigate the effects of solvent composition ($V_{cyclohexane}/V_{water}$), hydrothermal temperature, and Si to CPB molar ratio on the morphology and structure of the nanoflowers.[120]

First, various solvent compositions are examined, including higher cyclohexane content (7 : 5, 1 : 1) and lower cyclohexane content (5 : 7, 1 : 2). Results show that a higher cyclohexane content leads to uniform flowers with a loose flower structure, while a relatively lower cyclohexane content results in a more compact structure and uniform-sized flowers. However, changing the ratio to 1 : 3 or 0 caused the spherical morphology of the nanoflowers to be severely disrupted. Nonetheless, the XRD patterns of the samples still indicate favorable mesoporous characteristics. This suggests that the mesoporous structure is primarily determined by the template, while cyclohexane plays a crucial role in shaping the spherical morphology of the nanoflowers.

Second, spherical nanoflowers are synthesized at various hydrothermal temperatures ranging from 80 °C to 140 °C. Interestingly, all four samples, synthesized at 80 °C, 100 °C, 120 °C, and 140 °C, respectively, displayed uniform flower sizes and maintained the fundamental spherical morphology, indicating that temperatures within the investigated range do not significantly affect the basic shape of the nanoflowers. When comparing the samples synthesized at 80 °C and 100 °C, there is no noticeable variation in flower size, but the petals of the latter appeared more elongate and exhibit better overall appearance. At 120 °C, there is a significant change in both flower size and petal shape. The diameter decreases to less than 200 nm, and the nanostructure becomes looser. However, when the temperature is increased to 140 °C, the flower size increased to 400 nm, but the petals do not fully expand.

Third, the synthesis of the samples involves using different molar ratios of TEOS to CPB. The results clearly demonstrate that this ratio has a significant impact on the morphology of the materials. When the TEOS/CPB ratios are 4.37 and 6.02 (sample B and D), the nanoflowers exhibit a diameter of approximately 200 nm. On the other hand, when the ratios are 3.58 and 5.21 (samples A and C), the diameter increased to approximately 500 nm. Additionally, the mesostructures or petal structures of the materials varied noticeably across the different TEOS/CPB ratios in the four samples. For instance, the wrinkled structure observed in the sample with a ratio of 4.37 (sample B) stretched further compared to the sample with a ratio of 6.02 (sample D). Furthermore, the BET measurement results revealed that the surface area of sample B is 501 $m^2\,g^{-1}$, which is higher than that of sample D (352 $m^2\,g^{-1}$).

ZnO nanoflowers, referred to as ZnO-0, are synthesized through a hydrothermal process. Additional types of ZnO nanoflowers, namely ZnO-250 and ZnO-950, are created by subjecting them to ultrasonic treatments using different ultrasonic devices prior to the hydrothermal procedure. The nanosheets within the ZnO-0 nanoflowers have smooth edges, while the edges of ZnO-250 and ZnO-950 nanoflowers display jagged margins resembling carnations.[87] Analysis of the materials yielded the following findings: the average diameter of the ZnO nanoflowers decreases from 2.31 μm to 1.95 μm as the intensity of ultrasonic treatment increased. This reduction in size is also observed in the nanosheets constituting the nanoflowers. Specifically, the average thickness of the nanosheets decreases from 40.32 nm to 18.72 nm, and their average length varied from 350.35 nm to 270.21 nm with higher ultrasonic intensity. As a result, ZnO-950 nanoflowers exhibit the smallest size, primarily attributed to the more pronounced acoustic cavitation induced by the ultrasonic treatment.

Ag nanoflowers (Ag NFs) with hierarchical structures consisting of large buds (250–580 nm) and thin petals (9–22 nm) are synthesized.[121] The size of the buds increases significantly with higher concentrations of ascorbic acid (0.1–1 M), as a reducing agent, resulting in the formation of Ag NFs named Ag NF I, II, III, IV, and V. The use of higher concentrations of ascorbic acid leads to a more spontaneous reduction and larger bud size. The specific surface area of the Ag NFs, measured from the BET adsorption isotherm,[122,123] also increases with higher concentrations of ascorbic acid (2.08, 3.82, and 5.15 $m^2\,g^{-1}$ for Ag NF I, III, and V). However, when the concentration of ascorbic acid is too high (2 M), the flower structure with thin petals cannot be maintained. Changing the reaction time (10 s ∼120 min) does not affect the bud size of Ag NF III (0.3 M of $AgNO_3$ and 0.3 M of ascorbic acid), confirming its spontaneous anisotropic growth. The bud size of Ag NF III is not affected by changes in temperature below 80 °C, but the petal structure of the flower changes when the reaction temperature exceeds 90 °C.

Ag hierarchical assemblies are formed in a solution with the help of small acid molecules, without the use of polymer surfactants or capping agents. As shown in Fig. 3a, irregular Ag particles with Ag+ reduced by ascorbic acid (no extra acid added) are observed, with approximately 1 μm size. A magnified image of the Ag particle shows that it comprises 50–100 nm thick Ag nanosheets (Fig. 3b), with the structure resembling Ag nanoparticles obtained through a similar procedure. The addition of citric acid forms perfect microspheres with a diameter of ∼2 nm composed of numerous close-packed 20 nm thick Ag nanosheets (Fig. 3c and d). In the presence of mandelic acid, flower-like Ag particles are formed from loosely packed 50 nm thick Ag nanosheets (Fig. 3e and f), while using toluene sulfonic acid forms microscale Ag yarn-balls assembled from cross-linked 50 nm thick Ag nanosheets (Fig. 3g and h).[124]

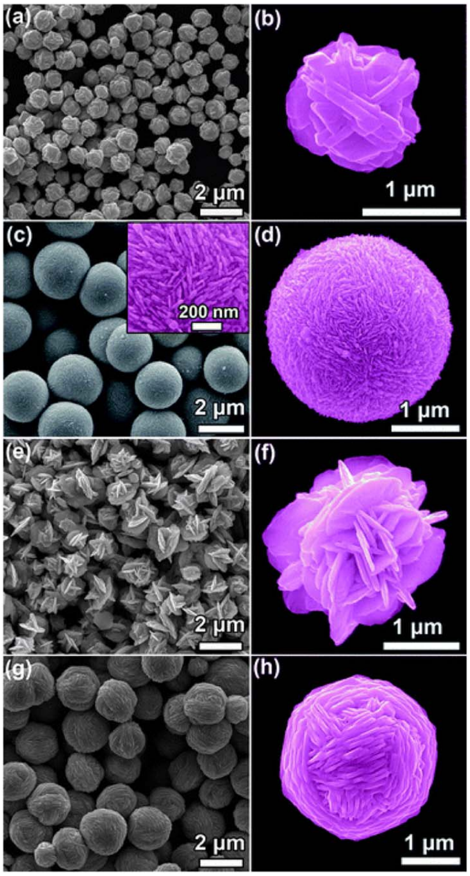

Fig. 3 SEM images of Ag structures prepared through a chemical reduction of Ag+ ions ($AgNO_3$) by ascorbic acid as the reducing agent, without using any polymersurfactant or capping agent. Before ascorbic acid is added to initiate the reduction reaction, (a and b) no acid, (c and d) citric acid, (e and f) mandelic acid, and (g and h) toluenesulfonic acid are added to the reaction system to control the assembly of the produced Ag nanostructures. Adapted with permission from ref. 124. Copyright © the Royal Society of Chemistry 2011.

Flower-shaped NiO nanostructures are currently being synthesized using microwave and hydrothermal methods. The hydrothermally reacted sample exhibits cubic phase NiO nanostructures with a reduced particle size of 8 nm, as observed in the XRD patterns. In contrast, the microwave-reacted sample has a larger particle size of 12 nm. The UV band gap curves confirm a blue shift, indicating the quantum confinement effect of the NiO nanostructures, and this is further supported by the photoluminescence spectrum. The SEM analysis of the

Table 5 Summary of the BET surface area, pore volume, pore diameter and size of SiO_2 NPs formed in a number of co-solvents, varying from C-3 to C-8 alcohols. Reprinted with permission from ref. 126. Copyright © 2019 Elsevier B.V. All rights reserved

Co-solvent	Solvent	Size of NPs (nm)	BET surface area ($m^2\ g^{-1}$)	Pore diameter (nm)	Pore volume ($cm^3\ g^{-1}$)
Propanol	Methyl phenyl ether (anisole)	505	567	3.26	0.564
Butanol		480	580	3.27	0.603
Pentanol		440	621	3.27	0.768
Hexanol		385	705	3.44	0.996
Heptanol		385	702	3.45	1.015
Octanol		380	711	3.45	1.021

hydrothermally processed samples reveal an abundance of flowers with minimal agglomeration. These flowers form clusters with a diameter ranging from 1 to 2.5 μm. Conversely, the nanostructures produced through the microwave treatment process exhibit similar flower-like morphologies but show higher levels of agglomeration compared to the hydrothermally grown samples due to indirect heating of molecules caused by microwave radiation.[105]

The researcher conducts an investigation into the diameter distribution of Pd–Ag nanoflowers, taking into account the composition ratio of Pd to Ag. The Pd_1Ag_2 nanoflowers obtained in their original state exhibited a narrow size distribution, with an average diameter of approximately 29.27 ± 3.74 nm. This size is significantly smaller than that of Pd_1Ag_1 (33.20 ± 4.23 nm) and Pd_1Ag_3 (32.48 ± 4.27 nm).[125]

Uniform-sized silica nanoflowers with a large accessible surface area are successfully synthesized using a visible light-driven green chemistry route. The synthesis process involves the use of CTAB as a structure-directing agent in combination with various co-solvents. The size, BET surface area, pore volume, and pore diameter of the resulting SiO_2 nanoparticles are analyzed and summarized in Table 5. CTAB molecules within a mixture of water, anisole, and hexanol self-assemble into micelles that play a crucial role in providing the necessary template derived from these micellar aggregates. This template subsequently controls the shape and size of the nanoparticles. Therefore, due to the interaction between co-solvents and CTAB, the shape and size of Si nanoparticles can be influenced. As the number of alcohol co-solvents increases from C-3 to C-8, the size of the nanoparticles decreases, while the BET surface area and pore volume increase.[126]

4. Mechanism

Nanoflowers are complex nanostructures composed of nanoscale petals or branches arranged in a flower-like pattern. They are typically synthesized using various techniques, as introduced in Section 2. Methods for preparing nanoflowers. The specific mechanism of nanoflower formation depends on the materials and fabrication techniques employed. Here, we will provide a general overview of commonly used approaches with representative examples.

The first mechanism involves synthesizing surfactant-free, template-free, and seedless nanoflowers. The synthesis of NiO nanoflowers is initiated with the chemical reaction and the subsequent hydrothermal process, leading to the formation of $Ni(OH)_2$ nuclei. The growth process of nanoflowers typically commences with the formation of small nuclei. The chemical reaction can be described as follows:

$$CO(NH_2)_2 + 3H_2O \rightarrow NH_4HCO_3 + NH_3\cdot H_2O \rightarrow OH^- + NH_4^+ \quad (1)$$

$$Ni^{2+} + NH_3 + H_2O \leftrightarrow [Ni(H_2O)_{6-x}(NH_3)_x]^{2+} \quad (2)$$

$$Ni^{2+} + OH^- \rightarrow Ni(OH)_2\downarrow \rightarrow NiO \quad (3)$$

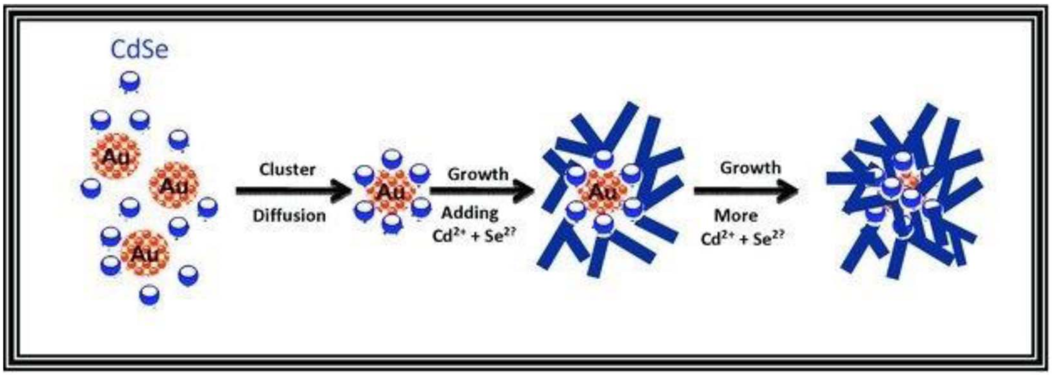

Scheme 1 Proposed mechanism for the formation of the Au@CdSe nanoflowers. Reprinted with permission from ref. 128. Copyright © 2011 WILEY-VCH Verlag GmbH & Co. KGaA, Weinheim.

Subsequently, the nuclei grow into nanosheets. With an extended hydrothermal time, the surface energy decreases, leading to a gradual self-orientation of thin nanosheets. This self-orientation process ultimately results in the formation of flower-like hierarchical structures composed of $Ni(OH)_2$. Following that, the obtained $Ni(OH)_2$ structures are subjected to calcination at 500 °C. This calcination process transforms the $Ni(OH)_2$ into NiO nanoflowers, characterized by the assembly of smooth nanosheets.[127]

The following mechanism encompasses the creation of nanoflowers through a process that eliminates the use of surfactants and templates, relying on seed mediation. The Au@CdSe and Ag@CdSe core–shell nanoflowers are synthesized *via* a one-pot hot-injection method.[128] Initially, gold clusters act as heterogeneous nucleation sites for the growth of CdSe nanocrystals. As CdSe clusters with a magic-size, which refers to a specific size of stable CdSe clusters due to their bulk crystalline atomic packing and fully closed outer shell, and zinc blende crystal structure begin to form, they diffuse towards the gold nanocrystals and bind to surface defect sites. Through a multiple injection process involving the addition of more Cd and Se ions, additional CdSe species attach to the CdSe core clusters on the gold surface. These attached species undergo a transformation into wurtzite and adopt a multiple-branched structure, ultimately resulting in the formation of nanoflower shapes. The proposed mechanism is illustrated in Scheme 1. Third, seedless NiO nanoflowers assembled with nanorods or nanoneedles are synthesized using two surfactants: CTAB and EG.[118] The synthesis process involves the following steps. In the case of nanorod-assembled NiO nanoflowers, ammonia aqueous is used as an alkaline reagent to release OH^- ions. CTAB, a surfactant with a hydrophobic part, interacts with $Ni(OH)_2$ and preferentially absorbs onto the CTA^+ heads, causing the $Ni(OH)_2$ nanoparticles to connect and form nanorods. CTAB acts as an adhesive, facilitating the gathering of the nanorods. Finally, driven by the minimum surface energy theory, the nanorods self-assemble into flower-like architecture. For the formation of nanoneedle-assembled hierarchical NiO nanoflowers, Ni^{2+} and $C_2O_2{}^{-4}$ form a $NiC_2O_4 \cdot 2H_2O$ polymer type ribbon due to the complexation of Ni+ and $C_2O_2{}^{-4}$. EG, a surfactant with symmetrical structures and functional group-OH, acts as a ligand to Ni and blocks the crystal surface parallel to the [0,1,1] direction. The microstructures formed by $NiC_2O_4 \cdot 2H_2O$ are connected along the [0,1,1] direction, resulting in needle-like structures. Over time, the $NiC_2O_4 \cdot 2H_2O$ nanoneedles aggregate and assemble into hierarchical needle-flowers. Finally, NiO nanoflowers are obtained through thermal calcination.

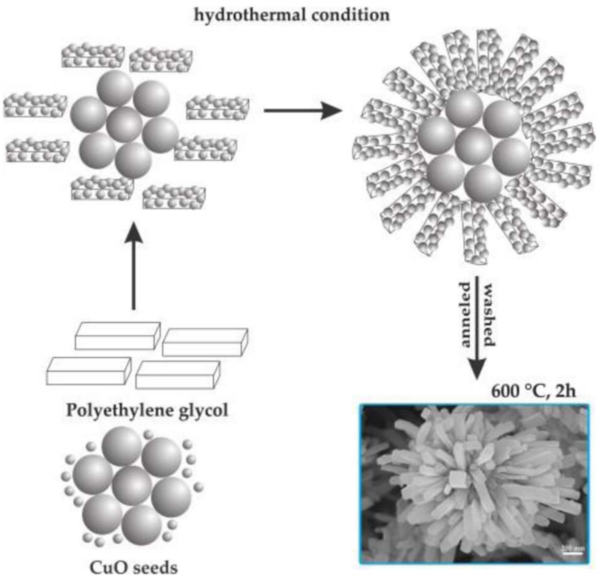

Fig. 4 Formation mechanism of flower-like CuO hierarchical nanorods. Reprinted with permission from ref. 129. Copyright © 2014 Elsevier Ltd. All rights reserved.

The growth mechanism of seed mediated flower-like CuO nanostructures utilizing PEG 4000 as a surfactant and template can be explained as follows.[129] Initially, the formation of $CuCO_3$ precipitate occurs through the following chemical reaction:

$$2Cu(NO_3)_2 + NH_4HCO_3 \rightarrow 2CuCO_3 + 5NO + NO_2 + 5H_2O \quad (4)$$

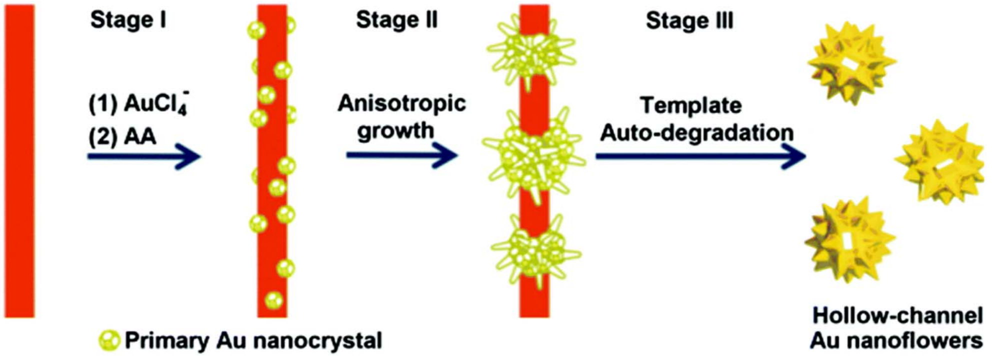

Fig. 5 Schematic illustration of the proposed mechanism for the formation of hollow gold nanoflowers: stage (I) Au nucleates on the template surface; stage (II) Au primary crystal undergoes anisotropic growth to form branches; stage (III) the as-formed Au nanoflowers catalyze the degradation of the template in the presence of AA, leaving the open hollow channel and releasing the individual HAuNFs. Adapted with permission from ref. 130. Copyright © The Royal Society of Chemistry 2016.

Under hydrothermal conditions, $CuCO_3$ undergoes a transformation into CuO through the following reaction:

$$CuCO_3 \rightarrow CuO + CO_2 \tag{5}$$

The formation of flower-like CuO nanostructures is likely guided by the proposed mechanism depicted in Fig. 4. According to this mechanism, PEG plays a role as a soft template for the development of CuO nanoflowers. In the initial stage, the combination of Cu^{2+} aqueous solution and PEG leads to the generation of initial nucleation seeds, serving as the starting point for particle growth. PEG, being a nonionic surfactant with a molecular structure of $H(–O–CH_2–CH_2)_n–OH$, tends to form chain-like structures when dissolved in water. When the nucleation seeds reach a critical size, the PEG chains act as templates by absorbing smaller particles through the end OH bonds for the formation of the CuO flower nanostructure. Subsequently, these absorbed particles aggregate around the larger CuO seeds. Following a 2-hour annealing process at 600 °C, the PEG templates are removed, resulting in the formation of flower-like CuO nanostructures.

Finally, the fabrication of hollow-channel Au nanoflowers is achieved through a simple one-step synthesis method, utilizing a bifunctional template composed of an auto-degradable nanofiber.[130] This templated synthesis involves three primary steps (Fig. 5). (1) *In situ* nucleation: the initial formation of primary Au nanocrystals occurs on the template composed of methyl orange–$FeCl_3$ (MO–$FeCl_3$). This is facilitated by strong interactions, including the coordination between Au(III) and azobenzene in MO molecules, as well as the electrostatic interaction between $AuCl_4^-$ ions and Fe^{3+}. The absorption of $AuCl_4^-$ onto the MO–$FeCl_3$ nanofiber takes place due to these interactions, achieved through the reduction of $HAuCl_4$ by ascorbic acid (AA). After the introduction of the reducing agent AA, Au nuclei form on the surface of the template, resulting in the generation of primary Au nanocrystals. (2) Anisotropic growth: the primary nanoparticles experience anisotropic growth, resulting in the formation of flower-like structures. This growth process leads to the development of the hollow-channel Au nanoflowers. (3) Auto-degradation of the template: the presence of AA catalyzes the auto-degradation of the template. As a result, the as-formed Au nanoflowers contribute to the degradation process, leading to the dissolution of the nanofiber template.

5. Synthesis methods and characterization of inorganic nanoflowers

5.1. Nanoflowers with metallic composition

In this section, the synthesis methods and characteristics of nanoflowers having a metal constituent, such as Au, Pt, Pd, and Ag, are mainly reviewed. Various shapes, surfaces, densities of corners and edges of nano-petals, particle size distribution, and growth mechanisms are also described.

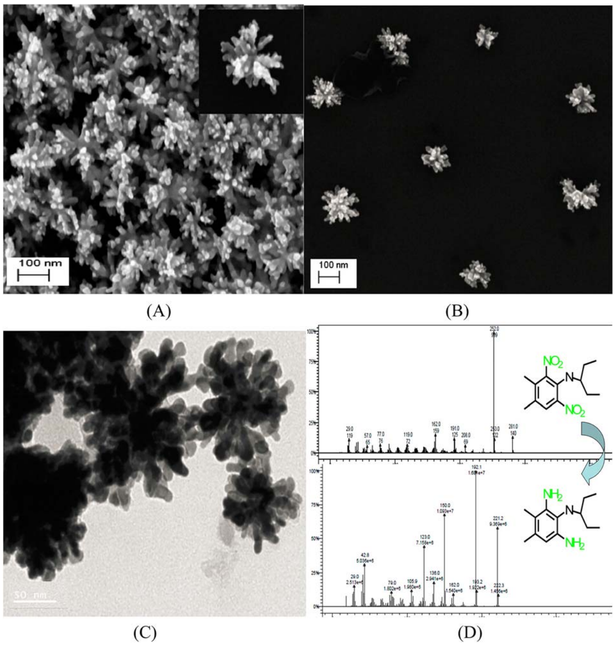

Fig. 6 (A and B) SEM and (C) TEM images of gold nanoflowers that are synthesized; mass spectral data of (D) show the process of degradation of pendimethalin (above) to *N*-(1-ethylpropyl)-2,6-diamino-3,4-xylidine (below). Reprinted with permission from ref. 139. Copyright © 2014, American Chemical Society. All rights reserved.

5.1.1. Au nanoflowers.

5.1.1. Au nanoflowers. Hierarchical branched Au nanostructures (labeled nanoflowers), with sharp peaks and valleys on the surface of multibranched Au nanoparticles, have recently received considerable attention because of their high total surface-to-volume ratios, forming potential hotspots for localized near-field enhancements.[131] Depending on their structural features, they also exhibit interesting optical properties.[130,132] Thus, branched nanomaterials can be applied in several fields, including catalysis,[133],[134] sensors,[132] drug delivery,[135] and photothermal therapy.[136]

The branched Au[137,138] nanomaterials are obtained in the presence of (1-hexadecyl) trimethyl ammonium chloride (CTAC), or gemini amphiphiles, as capping agents.

In addition, the anisotropic Au flower-shaped nanomaterials are synthesized using a surfactant-free biocompatible Good's buffer, such as 2-[4-(2-hydroxyethyl)-1-piperazinyl] ethanesulfonic acid (HEPES).[131] Synthesis of hollow-channel Au nanoflowers using MO–$FeCl_3$ nanofiber as a bifunctional template is also reported.[130]

Interestingly, unlike other synthetic strategies, relatively monodisperse Au nanoflowers[139] without seeds and other surfactants have been formed using the nontoxic chemical hydroxylamine (NH_2OH) without stabilizers or adjustment of the pH environment. First, 50 μL of aqueous $HAuCl_4$ solution (wt 1%) is added to 2.5 mL of deionized water. Subsequently, 10 μL of aqueous NH_2OH solution (wt 50%) is injected into the solution with stirring and reacted for an additional minute. An Au nanoflower dispersion is obtained, with Au nanoflowers of approximately 100 nm diameter, with relatively narrow size

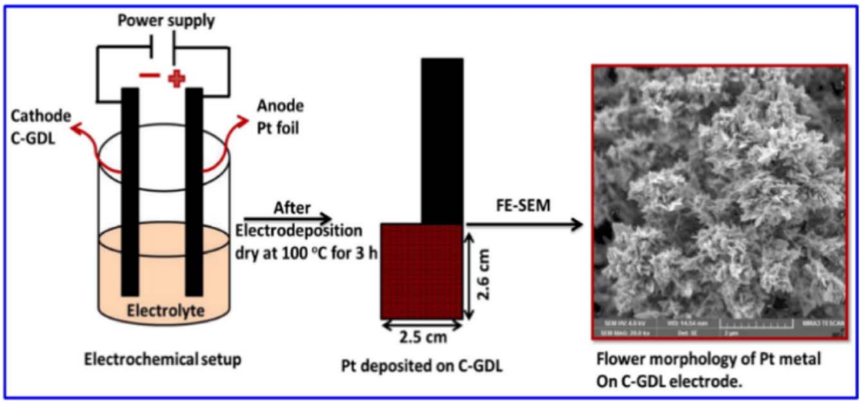

Scheme 2 Illustration of Pt metal nanoparticles, directly deposited on carbon-coated GDL, and its surface morphology. Reprinted with permission from ref. 154. Copyright © 2020 Elsevier Inc. All rights reserved.

distribution, based on SEM and high-resolution transmission electron microscopy (HR-TEM) analyses (Fig. 6A–C). These Au nanoflowers can be used as a nitroaromatic pesticide degradation platform, to catalyze the otherwise impossible reduction of pendimethalin by $NaBH_4$. This novel degradation platform could be beneficial for environmental protection, including the remediation of soil contamination and sewage treatment.

5.1.2. Pt nanoflowers. Pt nanomaterials have extensive research potential because of their unique physical and chemical properties. Their catalytic activity has been utilized in many applications, such as the production of hydrogen gas from cyclohexane,[141] control of vehicle emissions,[142,143] sensing,[144] and fuel cell applications (as electrocatalysts).[145] The catalytic efficiency and selectivity of Pt nanomaterials are highly dependent on their size, shape, composition, crystallinity, and surface structures.[146] Therefore, many research groups have developed Pt nanostructures of different shapes.[147–152] The synthesis of flower-shaped Pt nanoparticles, described in detail in this section, has attracted considerable attention.

According to Table 7, although the liquid phase synthesis[153] has also been reported for preparing flower-shaped Pt nanomaterials, one of the most widely used methods is electrodeposition, such as potentiostatic[111] and galvanic methods,[112] as well as sonoelectrodeposition.[110]

The 3D ultra-fine Pt nanoflowers deposited on the surface of a carbon-coated gas diffusion layer electrode (C-GDL) are also prepared by a one-step electrodeposition method (Scheme 2).[154] The morphological features of the Pt nanomaterials are modified from nanospheres to 3D nanoflowers by a difference in current density. The Pt nanoflowers electrodeposited at a current density of -24 mA cm^{-2} for 15 min exhibit high peak power density of 660 mW cm^{-2} at 0.6 V in polymer electrolyte fuel cells (PEFCs).

Zuo *et al.* used the galvanic replacement reaction of Te nanowires (Te NWs) to synthesize monomorphic single-crystalline Pt dendritic flowers with enriched edge and corner atoms.[112] As shown in Scheme 3, after the addition of the as-prepared Te NWs to the CTAB aqueous solution, H_2PtCl_6 (pH = 7) is injected into the mixture of Te NWs and CTAB to generate a metastable Te@Pt structure. Subsequently, H_2PtCl_6 (pH = 7) is injected for a second time when the color of the solution turns amber, to form Pt nanoflowers. The Pt nanoflowers exhibit excellent catalytic activity for glycerol electro-oxidation under acidic conditions, with higher mass activity and better structural stability than commercial Pt/C (20% Pt), indicating their potential utility in direct-glycerol fuel cells.

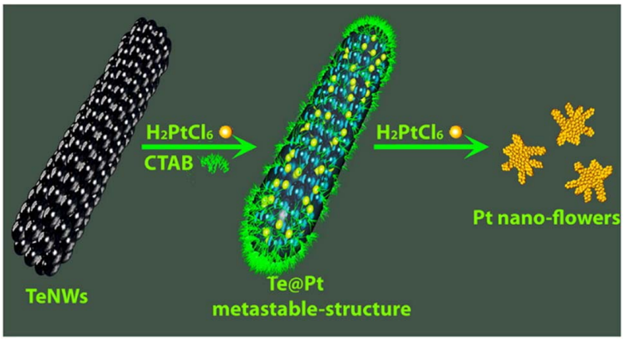

Scheme 3 Schematic illustration of the evolution from Te NWs to Pt nanoflowers with well-defined morphologies. Reprinted with permission from ref. 112. Copyright © 2015, American Chemical Society. All rights reserved.

5.1.3. Pd nanoflowers. Pd is often considered to be an alternative catalyst to Pt for the oxygen reduction reaction and direct alcohol oxidation due to their similar properties (they belong to the same group in the periodic table, exhibit FCC (face-centered cubic) crystal structures, and have similar atomic sizes). Furthermore, Pd is approximately 50 times more abundant than Pt and much less expensive.[161]

In recent years, Pd nanostructures have attracted immense research attention because of their larger surface-area-to-volume ratio and numerous active centers due to their unique morphology.[162–165] The key factors affecting the properties and functions of a material are architecture, crystallographic features, size, shape, and specific crystal planes.[166–169] Among the various nanostructures, 3D Pd nanomaterials, with a porous nature, large surface areas, and numerous active centers, have been considered as promising catalytic materials.[166,170] This section introduces the fabrication methodologies and applications of Pd nanoflowers.

The Pd nanoflowers have been synthesized by liquid phase synthetic methods[171] and electrodeposition[172] (Table 8), like the Au and Pt nanomaterials.

For instance, Maniam and Chetty reported the electrodeposition of shape-controlled Pd nanoflowers on an electrochemically activated carbon-black substrate (Vulcan XC-72R) using a potentiostatic technique, with/without different concentrations of PEG-6000 as an additive.[172] The PEG polymer surrounding the crystal nuclei hinders crystal growth and generates a steric hindrance effect to reduce particle–particle aggregation.[173] Additionally, the concentration of PEG strongly influences particle aggregation. Electrodeposition of Pd with 10^{-2} mM PEG changes the morphology from spherical to flower-like, forming well-dispersed nanoflowers with 0.2 mM PEG. The PEG acts as a scaffold for the nucleation sites at an optimum concentration (0.2 mM), to form flower-like shapes without any nucleation. In terms of the electrochemical surface area (ESA) and mass-specific current density, the electrodeposited Pd nanoflowers exhibit three- to four-fold enhanced electrocatalytic activities compared to spherical Pd deposits in the oxygen reduction reaction, formic acid oxidation, and CO stripping reaction.

What is noteworthy is the development of green chemistry research. Pd nanoflowers are synthesized using carrageenan as the capping agent, which is a natural macromolecule from the ocean, and L-ascorbic acid as the reducing agent (Fig. 7).[171] Experimental data indicate that the critical factor for the synthesis of Pd nanoflowers is the use of carrageenan, while the concentration of L-ascorbic acid affects the length of thorns grown on Pd nanoflowers. To investigate the effect of concentration on the surface morphology of Pd nanoflowers, Pd products are prepared using 20, 40, 60, 120, and 180 mg L-ascorbic acid in synthetic solutions and labeled Pd-AA20, Pd-AA40, Pd-AA60, Pd-AA120, and Pd-AA180, respectively. Pd-AA60(0) indicates the synthesis of Pd-AA60 without carrageenan. As shown in the SEM image (Fig. 8), the average particle size of Pd-AA60 is approximately 280 ± 30 nm, with Pd-AA60 exhibiting the longest and thinnest thorns (approximately 132 ± 15 nm long and 25 ± 7 nm thick). All Pd products using carrageenan exhibit flower-like morphology, except Pd-AA60(0).

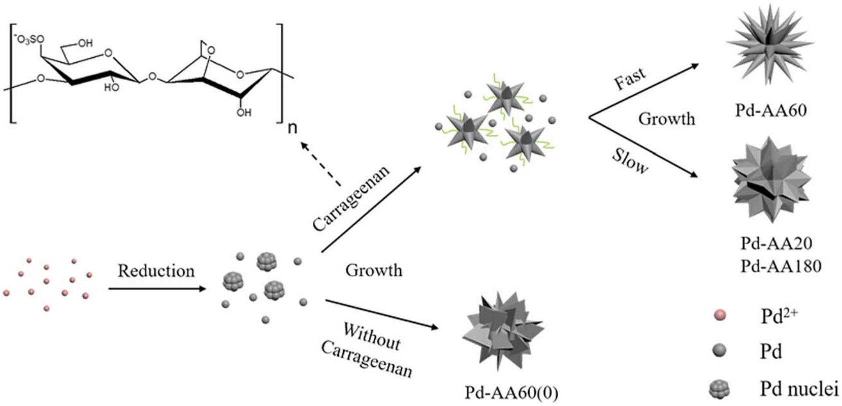

Fig. 7 Schematic illustration of the formation mechanism of Pd nanoflowers. Reprinted with permission from ref. 171. Copyright © 2017, American Chemical Society. All rights reserved.

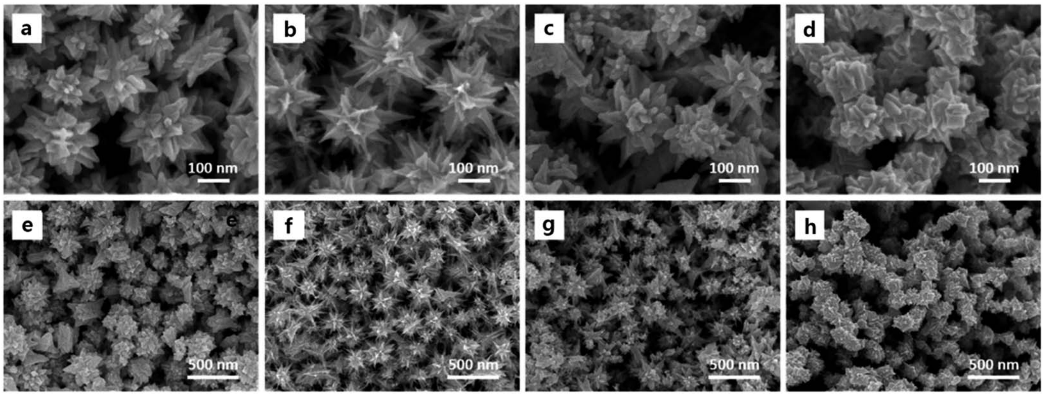

Fig. 8 SEM images of Pd-AA20 (a and e), Pd-AA60 (b and f), Pd-AA180 (c and g), and Pd-AA60(0) (d and h). Reprinted with permission from ref. 171. Copyright © 2017, American Chemical Society. All rights reserved.

The electrocatalytic activity of the synthesized Pd nanoflowers toward ethanol oxidation is investigated in an alkaline medium.

Pd-AA60, with the longest thorns, exhibits higher catalytic current density (1160 mA mg^{-1}) than commercial Pd/C, the reported Pd/C samples,[174] and other prepared Pd products (Pd-AA20, Pd-AA180, and Pd-AA60(0)) with short thorns exhibit better cycle stability, with catalytic activity maintenance of above 96% after 300 cycles.

5.1.4. Ag nanoflowers. Ag has been employed as an electrically conductive component in electronic devices. Ag particles with various morphologies have been investigated, with special emphasis on their size and structural effects on their electrical properties.[178–181] The Ag nanoparticles and their potential technological applications, such as water remediation, catalysis, and medicine have also been intensively studied owing to their chemical and physical properties, which are different from those of bulk systems.[182–186] At present, various Ag nanomaterials have been studied, such as, nanowires,[187] nanocubes,[188] nanoclusters,[189] nanoflowers,[190] and so on.[191] The 3D hierarchical nanostructures (with many external curved regions and nanogaps) could be promising candidates for highly sensitive SERS substrates for sensing applications.[124,192] Additionally, flower-shaped Ag nanoparticles with high electrical conductivity could be used for printable and flexible electronics.[121]

In this section, since Ag nanoflowers (Table 9) are also synthesized with the aforementioned strategies for manufacturing Au, Pt, and Pd nanoflowers, we would like to introduce some unique generation methods for Ag nanoflowers.

Zhang *et al.* reported the fabrication of novel self-assembled silver hierarchical structures by incorporating a small amount of acid in conventional solution chemistry, without using any polymer surfactant or capping agent.[124] This acid-directed synthesis inhibits the sorption of polymer molecules on metal surfaces, forming Ag particles with coarse morphology, which can be utilized as substrates to detect chemical or biological molecules through SERS. As we explained in Section 3. Experimental parameters' effect, the SEM images in Fig. 3 show the Ag assemblies prepared with the assistance of different acids at low and high concentrations, with uniform-structure Ag particles also being produced, corresponding to the acid incorporated by the acid-directed process. The irregular Ag particles, composed of Ag+ ions reduced by ascorbic acid, have an approximate size of 1 μm. They are made up of Ag nanosheets with a thickness of 50–100 nm. Adding citric acid forms perfect microspheres with a diameter of about 2 nm, which are composed of closely packed Ag nanosheets measuring 20 nm in thickness. In the presence of mandelic acid, flower-like Ag particles are formed, consisting of loosely packed Ag nanosheets with a thickness of 50 nm. Using toluenesulfonic acid results in the formation of microscale Ag yarn-balls assembled by cross-linked Ag nanosheets with a thickness of 50 nm. The obtained Ag particles with rough surfaces are promising SERS platforms for sensing applications, and the fabricated core–shell Ag wires exhibit high SERS sensitivity toward melamine, with a detection sensitivity of 5 ppm.

Long-range ordered Ag nanoflower arrays on patterned wafers are fabricated using a lithographic template-guided method based on the optical interference method and the difference in hydrophilicity between silicon and the photoresist.[192] As shown in Fig. 9a, 1D and 2D ordered array templates are obtained for supplying alternate relative hydrophilic and

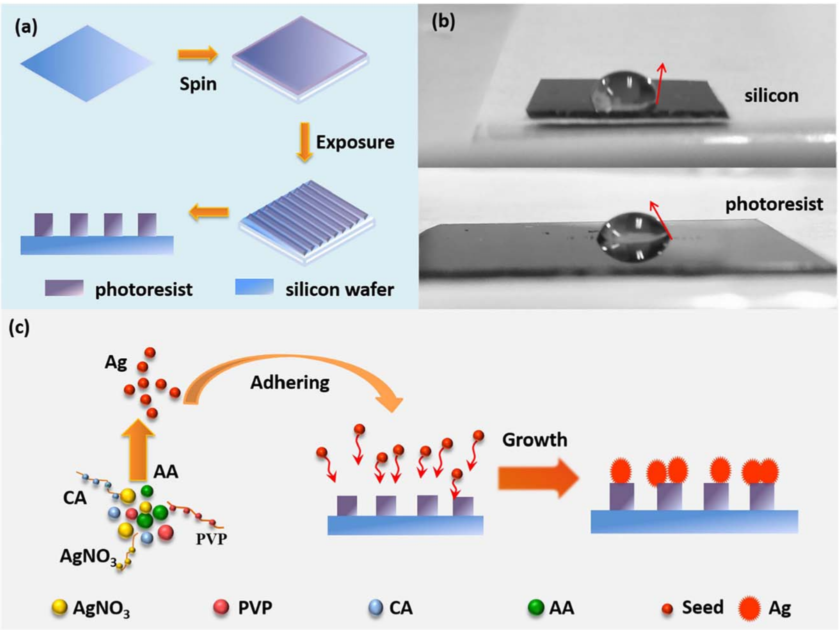

Fig. 9 Schematic diagram of fabricating the LROSNA structure. (a) Preparation of lithographic templates. (b) Optical image of the contact angle for hydrophilicity difference between silicon (the top) and photoresist (the bottom). (c) Schematic diagram of preparing the LROSNA structure. Reprinted with permission from ref. 192. Copyright © 2019 Elsevier B.V. All rights reserved.

hydrophobic regions, using holographic technology. The photoresist part is more hydrophilic than silicon, as shown by the contact angle of the droplet in Fig. 9b.[193] As shown in Fig. 9c, the prepared photolithographic template is immersed in the reaction solution containing $AgNO_3$, PVP, ascorbic acid, and citric acid, to form Ag nanoparticles. Ag seeds are induced on the photoresist surface owing to the difference in hydrophilicity between the photoresist and silicon. Finally, the seeds grow into silver nanoflowers with abundant hotspots.

As SERS substrates, the 1D and 2D pattern structures demonstrate high sensitivity with low detection limits of 5×10^{-10} M and 5×10^{-9} M, respectively, using rhodamine 6G as a probe molecule to investigate the hotspot effect of the nanogaps within/between the Ag nanoflowers.

5.1.5. Other-metal nanoflowers. Metal nanoflowers composed of Ni, Co, and Cu are summarized in Table 10.

5.1.6. Conclusion. Metal nanoflowers are one of the main topics of nanoflower research. Metal nanoflowers composed of Au, Pt, Pd, Ag, Ni, Co, and Cu are synthesized using various methods, such as liquid phase synthesis, electrodeposition, and green synthesis (also called biosynthesis) (Tables 6–10). As summarized in Tables 6–10, metal nanoflowers can be utilized

Table 6 Synthesis methods and applications of flower-like Au nanostructures. (Interestingly, all reactions used $HAuCl_4$ as a precursor.)

Variety of formed nanostructures	Synthesis method	Application	Ref./year
Fluorescent Au nanoflowers	Seedless, surfactantless room temperature synthesis using 5-hydroxyindole-3-acetic acid	SERS and electrocatalyst	134/2008
Au nanoflowers	Vesicle-directed generation using gemini amphiphiles	SERS	137/2010
Au nanoflowers	Melanin assisted seedless, template free synthesis	Catalysis, biochemistry, and Raman fields	140/2012
Hydrangea flower-like hierarchical Au nanostructures	One-pot, seedless synthesis using ascorbic acid and CTAC	SERS-based sensors	138/2015
Au nanoflowers with sheet-like petals	Seedless, reduction synthesis using ascorbic acid and silver nitrate	SERS substrates and sensors	132/2016
Hollow-channel Au and Ag nanoflowers	One step fabrication using an auto-degradable MO–$FeCl_3$ nanofiber as a bifunctional template	Catalysts and SERS probes	130/2016
Au nanoflowers, nanostars, and nanosnowflakes	Seed-less and surfactant-free approach using catechol as the reducing and structure-inducing agent	Catalyst and photothermal therapy	136/2019

Table 7 Synthesis methods and applications of flower-like Pt nanostructures

Variety of formed nanostructures	Synthesis method	Application	Ref./year
Pt nanoflowers with thin projections (petals)	Stabilizing reagent-free synthesis using $NaBH_4$	Surface-assisted laser desorption/ionization mass spectrometry of biomolecules	155/2007
Pt nanoflowers on a Si substrate	Potentiostatic pulse plating method	Electrocatalysts toward methanol and CO oxidation	111/2009
Porous Pt nanoflowers on clean indium tin oxide (ITO)	One-step and template-free electrodeposition method	Electrocatalysts for the methanol electro-oxidation of direct methanol fuel cells (DMFCs)	142/2010
Pt nanoflowers on the bare Au electrodes	Template-free ultrasonic electrodeposition method	Nonenzymatic glucose sensors	110/2012
Pt nanoflowers composed of an ordered array of nanoparticles	Ethanol reduction of H_2PtCl_6	Electrocatalysts for DMFCs and catalyst in C–C coupling reaction	153/2013
3D Pt nanoflowers on porous silicon	Electroless plating method	Electrocatalysts for monolithic integrated micro DMFCs	156/2013
Pt nanoflowers	Sonoelectrodeposition method	Electrocatalysts and nonenzymatic sensors	157/2014
Pt needle-like nanoflowers on a glassy carbon electrode (GCE) substrate	Template-free electrochemically potentiostatic method	Electrocatalysts for methanol oxidation reaction in DMFCs	158/2015
Pt nanoflowers	Chemical reduction and seed-mediated growth using tri-sodium citrate and ascorbic acid	—	159/2016
Nanoflower-shaped Pt on GCE	One-step electrochemical deposition method	Sensor for simultaneous detection of lead and cadmium at trace levels	160/2019

Table 8 Synthesis methods and applications of flower-like hierarchical Pd nanostructures

Variety of formed nanostructures	Synthesis method	Application	Ref./year
Pd porous single-crystalline nanoflowers	Seed mediated growth method using ascorbic acid and CTAB	Electrocatalysts for ethanol electro-oxidation	174/2014
Porous Pd nanoflowers	Polyol process using Pd(acac)$_2$ and oleylamine	Electrocatalysts for methanol electro-oxidation	175/2009
Spinous flower-like, cone-like, flower and coral reef-like Pd dendrites on glassy carbon plates	Electrochemical methods using cyclic voltammetry	Electrocatalysts toward formic acid electro-oxidation of microfluidic fuel cell channels	81/2013
Pd nanoflowers	Green synthesis (seedless chemical reduction method) using HEPES	Electrocatalysts for methanol electro-oxidation in alkaline media	170/2013
3D Pd nanoflowers on Ni-YSZ (yttria-stabilized zirconia) anode	Galvanic displacement reaction	Catalysts for direct ethanol solid oxide fuel cells	114/2016
Pd nanoflowers	Radiolytic reduction of Pd^{II}(acac)$_2$ in ethanol under a CO atmosphere	Plasmonic photocatalysts for the Suzuki–Miyaura cross-coupling reaction	176/2019
Pd nanoflowers on Ti film or on GCE	Electrodeposition process	Electrocatalysts in the reduction of Cr(VI)	177/2019

Table 9 Synthesis methods and applications of flower-like Ag nanostructures

Variety of formed nanostructures	Synthesis method	Application	Ref./year
Rose-, spike-, and snowflake-shaped Ag nanostructures	One-pot reduction method using ascorbic acid, poly(ethylene glycol), sodium acetate, and sodium citrate	SERS matrices	194/2007
Branched Ag nanoflowers	Biosynthesis using biofriendly molecule-rutin	SERS and antibacterial activities against *Pseudomonas aeruginosa*, *S. Faecalis*, and *Escherichia coli* bacterium	195/2009
Ag nanoflowers with multiple petals on ITO glass	Double-potentiostatic electrodeposition method	SERS	196/2012
Ag nanoflowers	Trisodium citrate-assisted biosynthesis using trisodium citrate and *Canarium album* foliar broths	SERS substrates	197/2013
Ag nanoflowers with nanogaps	Ice-water bath method using citric acid, and PVP	Broadband scatterers for high performance random lasers	198/2017
Ag nanoflowers on fluorine-doped tin oxide (FTO) glass (nanorods, dendrites, decahedrons, and icosahedrons are also formed)	Cyclic scanning electrodeposition method	Catalysts of non-enzymatic electrochemical glucose biosensors	199/2017
3D and 2D Ag nanoflowers	Seedless green liquid reduction method using AgNO$_3$, ascorbic acid, and sodium citrate	Multiple phase SERS-based molecule detection of food additives and environmental pollutants	200/2019
Ag nanoflowers	Green synthesis using *Kalanchoe daigremontiana* extract	Photocatalysts in the dye degradation of methylene blue and antibacterial activities against the Gram-negative bacteria *Escherichia coli* and the Gram-positive *Staphylococcus aureus*	76/2019
Ag nanoflowers with nanoleaves	Electrochemical deposition approach	SERS sensing substrates	113/2019

as electro-, photo-, and chemical-catalysts, gas- and biosensors, antibacterial agents, and so on, because of their unique morphologies and elemental effects. Initially, research mainly focused on new synthetic methods, shapes, formation mechanisms, and the application-based chemical, physical, and optical property testing of elemental nanoflowers. Many studies have been recently conducted to control the morphology and size of nanoflowers, to optimize their properties for applications.

5.2. Nanoflowers with metal oxide composition

Here, the unique properties of each metal-oxide material are introduced, and methods and properties of synthesizing nanoflowers using these materials are summarized.

5.2.1. TiO$_2$ nanoflowers. Here, TiO$_2$ has three crystalline phases: anatase (tetragonal), rutile (tetragonal), and brookite (orthorhombic).[204] Rutile TiO$_2$ is the most stable form, and the anatase and brookite phases can be transformed into the rutile

Table 10 Synthesis methods and applications of flower-like metal nanostructures

Compound	Variety of formed nanostructures	Synthesis method	Application	Ref./year
Ni	Ni nanospheres, nanowires, and nanoflowers	Surfactant-free non-aqueous sol–gel approach	—	201/2008
	Ni nanoflowers	Capping agent assisted and Ag-catalyzed growth	Catalysts	202/2010
Co	Co nanoflowers	Solvothermal synthesis using $RuCl_3 \cdot xH_2O$ (35 wt% Ru) and hexadecylamine	Catalysts for hydrogenolysis of glycerol to propylene glycol	33/2009
Cu	Cu nanoflowers	Capping agent assisted reduction process using oleylamine and CTAB	Catalysts in oxygen reduction reactions	203/2018

Table 11 Synthesis methods and applications of flower-like hierarchical TiO_2 nanostructures

Variety of formed nanostructures	Synthesis method	Application	Ref./year
Anatase and brookite TiO_2 nanoflowers	Hydrothermal process using tetrabutyl titanate, NaCl and $NH_3 \cdot H_2O$	Photocatalysts in the photodegradation of methyl orange	93/2009
Flower-like TiO_2 nanostructures	Low-temperature hydrothermal process using Ti powder and HF	Photocatalysts for the degradation of methylene blue dye	228/2010
Rutile TiO_2, stacks of multilayered nanoflowers with hexagonal nanopetals	Acid vapor oxidation method	Catalysis, solar cells, and electronic devices	229/2011
Hierarchically flower-like TiO_2 superstructures	Surfactant-free alcohothermal strategy in a $HF–H_2O–C_2H_5OH$ mixed solution using titanate nanotubes	Photocatalysts for decomposition of acetone in air and methyl orange in aqueous solution under UV illumination	230/2011
TiO_2 nanoflowers	Hydrothermal method using titanium(IV) butoxide and acetic acid	Photoelectrodes for dye-sensitized solar cells (DSSCs), photocatalysts for aqueous methylene-blue photo-oxidation	231/2011; 232/2020
Rutile-TiO_2 nanowires and nanoflowers on FTO glass and glass	Hydrothermal method using titanium(IV) butoxide and HCl	Solar cells, gas sensors, optoelectronics *etc.*	233/2015
Rutile/anatase TiO_2 heterojunction nanoflowers	Hydrothermal approach using titanium tetrachloride, urea, and CTAB	Photocatalysts for the photodegradation of real-dye waste water	234/2015
TiO_2 nanoflowers on ITO	PVP surfactant assisted liquid phase deposition technique using $(NH_4)_2TiF_6$, PVP, and boric acid	Photovoltaic materials of the photoelectrochemical cell	62/2015
TiO_2 nanoflowers on TiO_2 seed layer coated *p*-Si substrates	Hydrothermal method using titanium butoxide and HCl	Electron field emission and self-powered ultraviolet photodetector	235/2016
Hierarchical 3D TiO_2 nanoflowers on Ti substrate	Low temperature hydrothermal process using Ti plate and H_2O_2, and NaOH	Volatile organic compound sensors (acetone, methanol, 2-butanone, toluene and 2-propanol)	92/2016
Rutile TiO_2 nanoflower films on FTO glass	Hydrothermal process using tetrabutyl titanate and HCl	Photoanodes for DSSCs	236/2017
TiO_2 and reduced TiO_2 nanoflowers on FTO glass	Hydrothermal process and dipping reduction process with $NaBH_4$	Photoanodes for superior photoelectrochemical water splitting	226/2017
Rutile-TiO_2 nanoflower thin film on FTO substrate	Hydrothermal method using titanium(IV) isopropoxide and HCl	Solar cells	69/2020
Rutile- phase TiO_2 nanoflowers	Hydrothermal method using titanium(IV) butoxide, HCl, and CTAB	—	237/2020
3D TiO_2 hierarchical nanoflowers	Template-free solvothermal alcoholysis reaction using titanium trichloride, NaOH, and ethanol	Photocatalysts in the degradation of organic pollutants in wastewater	34/2021

phase at high temperatures (~750 °C).[204] However, bulk TiO_2 has little photocatalytic ability compared to nano TiO_2 due to its low dimensionality and quantum size effect.[205] The TiO_2 nanostructures have been utilized not only for photocatalytic materials,[206–208] but also for solar cells,[209] gas sensors,[210,211] molecular sensors,[212] and lithium batteries[213,214] because of their high oxidation activity,[215] low toxicity,[216] non-polluting nature,[217] and low cost.[217]

Table 12 Synthesis methods and applications of flower-like hierarchical CuO nanostructures

Variety of formed nanostructures	Synthesis method	Application	Ref./year
CuO nanoflowers on Cu plates	Direct reaction between a Cu plate and a KOH solution at room temperature	Field emission for nano-electronic devices	263/2008
CuO nanoflowers	Hydrothermal method using $Cu(NO_3)_2\cdot 3H_2O$ and $NH_3\cdot H_2O$	H_2O_2 sensor	98/2010
CuO nanoflowers on the glass substrate	Low-temperature chemical bath method using copper nitrate and hexamethylenetetramine	Electrochemical pH sensor	264/2011
CuO nanoribbons and nanoflowers	Low-temperature, one-pot water bath method using $Cu(OAc)_2\cdot H_2O$ and NaOH	Supercapacitors	265/2013
CuO nanoflowers	Solution combustion method using cupric nitrate and glycine	Photocatalysts for the photodegradation of methyl orange	266/2013
CuO nanoplatelets and nanoflowers	Hydrothermal method	Catalysts for the degradation of methylene blue	267/2014
Hierarchical 3D-flower-like CuO nanostructure on copper foil	Chemical bath deposition method	Supercapacitors	268/2015
Hierarchical CuO nanoflowers on the surface of flexible Cu foil	Chemical deposition method	Supercapacitor electrodes	269/2016
Flower-like CuO nanostructures with porous nanosheets on an alumina tube	Hydrothermal method using $Cu(CH_3COO)_2\cdot H_2O$, $NH_3\cdot H_2O$ and NaOH	H_2S sensors	99/2017
CuO nano-flowered surfaces	Submerged photo-synthesis of crystallites	Antibacterial agents against Gram-positive (*Staphylococcus aureus*) bacteria and Gram-negative (*Escherichia coli* K12) bacteria	270/2017
CuO nanoflowers	Low temperature solution process using copper nitrate, HMTA, and NaOH	Adsorbent for the removal of Pb^{2+} in waste-water treatment	271/2017
Hierarchical flower-like CuO film on Cu foil	One-step solution route at room temperature using Cu foil, NaOH, and $(NH_4)_2S_2O_8$	Photocatalysts for the degradation of methylene blue	272/2017
CuO nanospindles and CuO nanoflowers	Green synthesis process using *Dodonaea angustifolia* extract	Anti-microbial agents against Gram-negative *E. coli* and Gram-positive *S. aureus*	77/2018
Hierarchical porous CuO/Cu nanoflowers	Alkaline solution oxidation process in a water bath using Cu powder, sodium hydroxide, and ammonium peroxydisulfate	Non-enzymatic H_2O_2 sensors	273/2018
Hierarchical CuO nanoflowers	Hydrothermal method using $CuSO_4\cdot 5H_2O$, CTAB, sodium citrate, and KOH	Non-enzymatic sensors for H_2O_2 and glucose	85/2019
Flower-shaped CuO nanostructures	Biosynthesis using $Cu(CH_3COO)_2$ and *Ocimum sanctum* (*Tulsi*) leaves-extracted eugenol (4-allyl-2-methoxyphenol)	Photocatalysts and antibacterial agents	78/2020
Co_3O_4, NiO and CuO nanoflowers	Hydrothermal method	Photodiode, photodetector, sensor, battery and supercapacitor applications	274/2020
CuO nanoflowers on a glass slide	Wet chemical method using Cu foil, $(NH_4)_2S_2O_8$, and NaOH	Inflammable gas sensors (acetone, ethanol, methanol, isopropyl alcohol, toluene, chloroform and ammonia gas)	275/2020
CuO nanoflowers	Hydrothermal method	Catalysts for the degradation of methylene blue in the presence of H_2O_2 in waste water	286/2021

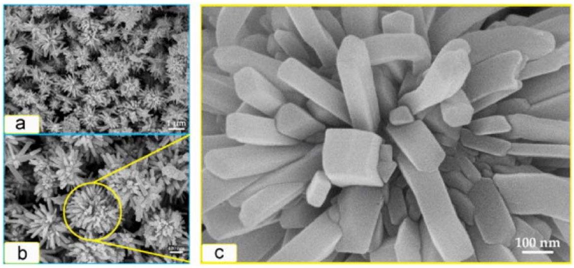

Fig. 10 FE-SEM images of CuO nanoflowers prepared at 170 °C for 24 h with different magnifications of: (a) 100 00×, (b) 200 00×, and (c) 1 000 00×. Reprinted with permission from ref. 129. Copyright © 2014 Elsevier Ltd. All rights reserved.

Over the past decade, various TiO_2 nanostructures have been investigated and used to form nanomaterials, such as nanosheets,[218] nanowalls,[219] nanorods,[220] nanowires,[221] nanotubes,[222] and nanobelts.[223] In particular, TiO_2 nanostructures with 3D dimensions, such as flowers and urchins, are promising candidates for many applications because of their properties.[224]

Our investigation (Table 11) shows that the most commonly used method for synthesizing TiO_2 nanoflowers is a hydrothermal method to synthesize nanomaterials by chemical reaction in aqueous media within a pressurized vessel (known as an autoclave).[225] Anatase and brookite TiO_2 nanoflowers are prepared using tetrabutyl titanate, NaCl and $NH_3 \cdot H_2O$.[93] Hierarchical 3D TiO_2 nanoflowers on Ti substrate are processed by the low temperature hydrothermal method.[92] TiO_2 and reduced TiO_2 nanoflowers on FTO glass are fabricated using hybrid technology combining hydrothermal and immersion reduction processes.[226]

Rutile TiO_2 3D nanoflowers are synthesized by the hydrothermal method in a saturated sodium chloride solution[74] and characterized by X-ray diffraction (XRD), whereby all the diffraction peaks indicate that the product is pure rutile TiO_2. The effects of the solvent on NF synthesis are investigated using FE-SEM. sample 1, synthesized in saturated NaCl solution, consists of partly agglomerating TiO_2 nanoflowers, with a diameter of 2–3 μm. The powder (sample 2) prepared by the hydrothermal method in anhydrous ethanol is stacked with uneven nanospheres. Furthermore, using deionized water as the solvent produces nanobulks with irregular shapes (sample 3). Sensors are fabricated using the as-synthesized TiO_2 samples and tested, to evaluate their ethanol gas-sensing ability and to investigate the influence of morphology on it. The gas response of the sensor, fabricated using partly agglomerated TiO_2 nanoflowers (sample 1) with a large surface area, is higher than that of the others.[227]

5.2.2. CuO nanoflowers. CuO, a p-type metal oxide semiconductor with a narrow bandgap (indirect bandgap of 1.2 eV (ref. 238) and direct bandgap of 3.2–3.3 eV (ref. 239–241)), has been intensively studied because of its unique characteristics,[242–244] and used in a wide range of applications as catalysts,[245] gas sensors,[246,247] lithium-ion battery electrodes,[248] and so on.[249,250] The microstructures and morphology of CuO nanomaterials significantly affect their physical and chemical properties.[251,252] Therefore, numerous CuO nanostructures with controlled morphologies have been researched, including nanoparticles,[253,254] nanorods,[255] nanowires[256] nanosheets,[257,258] nanotubes,[259,260] and nanoneedles.[261] Recently, nanoflowers have received considerable attention because of their unique morphologies.[262]

CuO nanoflowers are manufactured by various synthesis strategies: liquid phase synthesis, chemical deposition, hydrothermal method, photo-synthesis, and green synthesis (Table 12).

Their applications are also very diverse from hydrazine, H_2O_2, H_2S, and pH sensors to field emission for nano-electronic devices, supercapacitors, photocatalysts and absorbent for waste-water treatment, and antibacterial agents (Table 12).

For example, flower-like CuO nanostructures are synthesized using a wet chemical-assisted hydrothermal reaction,[129] with the formation mechanism illustrated in Fig. 4. The first nucleation seeds, formed by a mixed aqueous solution of Cu^{2+} and PEG, provide the nuclei for particle growth. PEG chains, nonionic surfactants composed of $H(-O-CH_2-CH_2)_n-OH$, absorb small seeds using the terminal OH bonds as soft templates when the nucleation seeds reach a critical dimension. Subsequently, they aggregate around the large seeds to form CuO flower nanostructures. Finally, the annealing process removes the PEG templates, forming flower-like CuO hierarchical nanorods. Fig. 10 shows FE-SEM images of the CuO nanoflowers obtained through hydrothermal treatment and calcination. Highly uniform nano-sized flowers (petals with 60–100 nm diameter and 500–700 nm length), consisting of many nanorods, are formed. The CuO nanoflowers are coated on SiO_2/Si substrates attached to Pt interdigitated electrodes to fabricate volatile gas sensors. The fabricated sensors show high selectivity and sensitivity toward ethanol vapor at approximately 230 °C (the optimized working temperature).

5.2.3. NiO nanoflowers. NiO nanostructures have been widely studied for decades and are considered promising candidates for many applications, such as gas sensors,[276] lithium-ion batteries,[277] magnetic materials,[278] and others.[279] The NiO nanostructures exist with various morphologies, such as, nanoflakes,[280] nanoparticles,[281] nanoplatelets,[282] nanowires,[283] nanowalls,[284] nanotubes,[285] and nanoflowers.[286] Among them, NiO nanoflowers have been extensively studied owing to their interesting architecture. Various morphologies of NiO nanoflowers have been fabricated using hydrothermal, microwave-assisted, solution plasma, solvothermal, and hard and soft template methods (Table 13). The NiO nanoflowers have been synthesized using various precursors in the presence/absence of surfactants/templates because the morphologies (petal size, thickness, porous/nonporous surface, and hollow structures) of the flower-shaped NiO nanostructures are influenced by the reaction conditions, including the type and amount of reagents (precursors, reducing agents, surfactants, template agents, and so on), reaction time, and temperature (Table 13). Cao *et al.* reported the synthesis of flower-like NiO nanostructures with three different morphologies using a template-free hydrothermal method by changing the volume of ammonia (25–28 wt%).[127] Sparse-type and close-type NiO

Table 13 Synthesis methods and applications of flower-like hierarchical NiO nanostructures

Variety of formed nanostructures	Synthesis method	Application	Ref./year
NiO nanoparticles and nanoflowers	Soft synthesis without organics at low temperature using Ni powder and water	—	291/2008
NiO with novel flower-like morphology	Calcination in a muffle furnace under a nitrogen atmosphere	Catalysts for CO oxidation	292/2009
Hierarchical porous NiO nanoflowers	Microwave-assisted fabrication and calcination	Supercapacitor	106/2010
NiO nanoflowers	Wet chemical process with a subsequent thermal treating process	Electrochemical sensors	293/2011
NiO nanodiscs and nanoflowers	Hydrothermal synthesis in a non-basic solution and calcination	Electrochemical test and water treatment	294/2011
NiO nanoflowers	Surfactant-free hydrothermal process and thermal decomposition	Li-ion batteries	295/2011
Porous NiO nanoflowers and nanourchins	Hydrothermal method using HMTA or urea as the precipitator in the absence or presence of a surfactant (PEG or PVP)	Catalysts for toluene combustion	96/2012
NiO nanoflowers	Solution plasma process	NO_2 gas sensor	296/2012
Flower shaped NiO nanostructures	Microwave and hydrothermal methods	—	105/2014
NiO hierarchical bundle-like nanoflowers	Hydrothermal-route assisted EG and subsequent thermal calcination	Gas sensors	297/2015
NiO nanoflowers	Template-less surfactant-free hydrothermal synthesis using nickel nitrate and HMTA	Photoelectrochemical hydrogen production	298/2015
3D hierarchical porous NiO nanoflowers	Solvothermal and post-calcination	Li-ion batteries	287/2016
3D flower-like NiO	Surfactant-assisted hydrothermal method	Ethanol gas sensors	299/2016
Flake–flower NiO architecture	Hydrothermal process and calcination using $Ni(NO_3)_2 \cdot 6H_2O$ and PVP	Ethanol gas sensors	300/2016
Rose-like, sphere-like, and plate–flower-like NiO nanostructures	Surfactant-assisted hydrothermal method and calcination using $Ni(NO_3)_2 \cdot 6H_2O$, or $NiCl_2 \cdot 6H_2O$, and PVP, or CTAB	Ethanol gas sensors	301/2017
Nanoneedle-assembled hierarchical and nanosheet-assembled hierarchical NiO nanoflowers	Hydrothermal method and subsequent calcination	Ethanol gas sensors	302/2017
Sparse-type and close-type NiO nanoflowers	Hydrothermal process assisted by CTAB or SDS	Ethanol gas sensors	97/2017
Porous NiO nanoflowers	Solvothermal method and calcination using nickel acetate tetrahydrate ($Ni(ac)_2 \cdot 4H_2O$) and urea	Li-ion batteries	100/2017
3D flower-like NiO hierarchical structures	Hydrothermal synthesis and calcination using $Ni(NO_3)_2 \cdot 6H_2O$, cetyltrimethyl ammonium bromide (CTAB) and ammonia, or $NiCl_2 \cdot 6H_2O$, $Na_2C_2O_4$, and ethylene glycol (EG)	Acetylene gas sensors	118/2018
3D hierarchical flower-like NiO nanostructures with three different morphologies	Template-free and low-cost hydrothermal method and subsequent calcinations with different volumes of ammonia (25%–28% wt%)	Ethanol gas sensors	127/2020
NiO nanoflowers	Polymer directed hydrothermal method and calcination using Pluronic F-127 block copolymer, $NiNO_3 \cdot 6H_2O$, and urea	Electrostatic adsorption of Congo red dye for wastewater treatment	303/2021

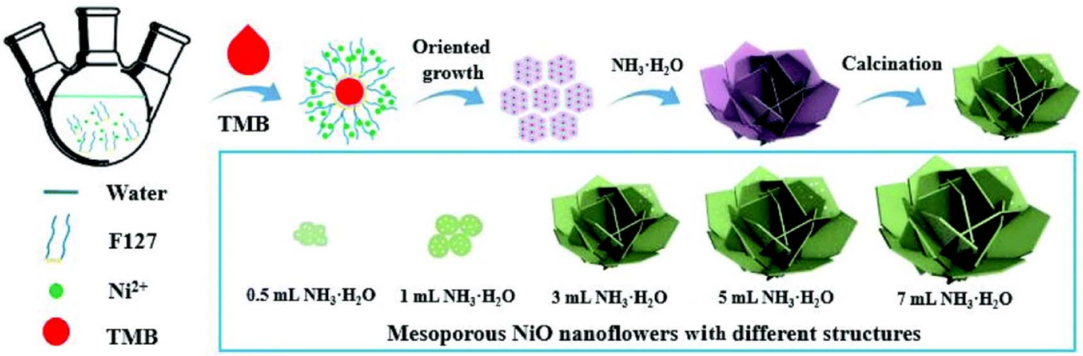

Scheme 4 Schematic illustration of the formation mechanism of NiO–NF-0.5, NiO–NF-1.0, NiO–NF-3.0, NiO–NF-5.0, and NiO–NF-7.0. Adapted with permission from ref. 286. Copyright © the Royal Society of Chemistry 2021.

nanoflowers are synthesized using a surfactant-assisted hydrothermal method with CTAB and SDS.[97] Additionally, porous NiO nanoflowers with different morphologies are synthesized by microwave-assisted fabrication[106] or solvothermal methods.[100,287] As shown in Table 13, these nanoflowers are primarily used for wastewater treatment, and as sensors, catalysts, and Li-ion batteries.

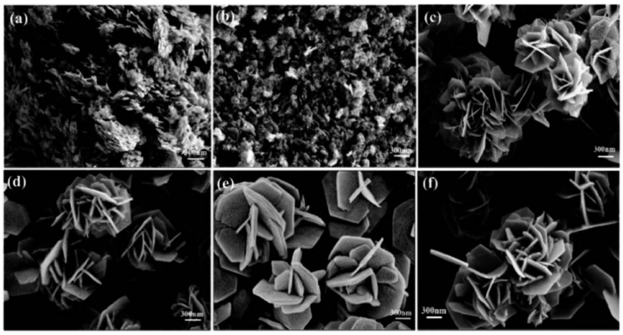

Fig. 11 FE-SEM images of (a) NiO–NF-0.5, (b) NiO–NF-1.0, (c) NiO–NF-3.0, (d) NiO–NF-5.0, (e) NiO–NF-7.0, and (f) NiO–NF-3.0 before annealing. Adapted with permission from ref. 286. Copyright © The Royal Society of Chemistry 2021.

As shown in Scheme 4,[286] Pluronic F127 acts as a micellar template for the fabrication of a lamellar structure. $Ni(NO_3)_2 \cdot 6H_2O$ is ultrasonically dissolved in water and mixed evenly under stirring in a water bath to form a homogeneous suspension. Subsequently, 1,3,5-trimethyl benzene (TMB), which acts as an interface-adjusting agent that avoids piling up of the lamellar structure, is slowly injected into the homogeneous suspension. The hydrophobic poly(phenylene oxide) segment of F127 can interact with TMB molecules through van der Waals interactions, while Ni^{2+} undergoes oriented attachment and self-assembles with the hydrophilic segment of F127. Addition of concentrated $NH_3 \cdot H_2O$ to the emulsion system promotes crystal growth. An Ni-based hydroxide precursor is generated through the hydrothermal process, and F127 and TMB are removed on decomposition to generate numerous mesopores during the high-temperature sintering process, forming NiO nanoflowers with mesoporous nanosheets. The synthesized samples are labeled NiO–NF-x, where x (0.5, 1, 3, 5, and 7 mL) is the volume of $NH_3 \cdot H_2O$. The FE-SEM images of the NiO–NF samples in Fig. 11 show the influence of the amount of $NH_3 \cdot H_2O$ on their morphology. The size range of the nanoflowers is 1–2 μm. On increasing the amount of $NH_3 \cdot H_2O$ to 3 mL, flower-like NiO–NF-3.0, composed of mesoporous hexagonal nanosheets, is formed (Fig. 11c). With increasing alkalinity, the stacked nanosheets become thicker (Fig. 11d and e)

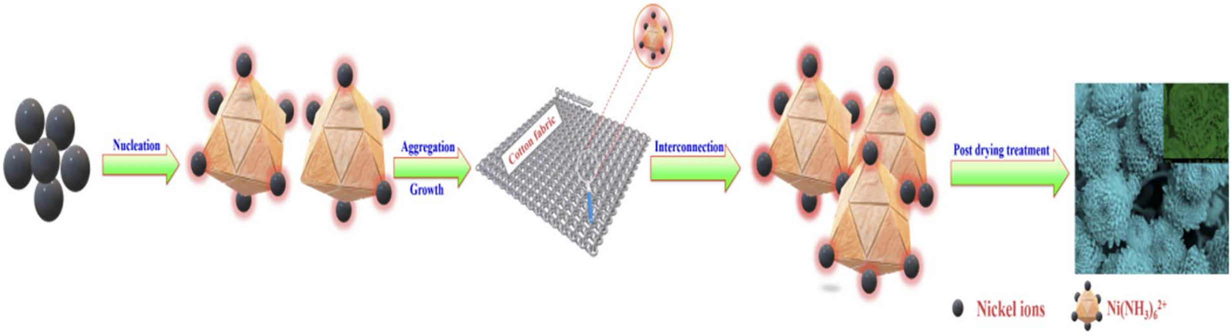

Fig. 12 Schematic representation of the growth process of the NiO_x on cotton cellulose. Reprinted with permission from ref. 288. Copyright © 2019, American Chemical Society.

Table 14 Synthesis methods and applications of flower-like hierarchical other metal oxide nanostructures

Compound	Variety of formed nanostructures	Synthesis method	Application	Ref./year
SnO_2	Super-hydrophobic 3D SnO_2 flowers with nanoporous petals	Controlled shape-preserving thermal oxidation process	—	304/2004
SnO	Nanoparticle-attached SnO nanoflowers	Free cation-induced decomposition of an intermediate product tin oxide hydroxide ($Sn_6O_4(OH)_4$)	Anodes for high-capacity lithium-ion rechargeable batteries	305/2009
α-Fe_2O_3 (hematite)	Porous α-Fe_2O_3 flower-like nanostructures	Solvothermal reactions and sequential calcinations	Lithium-ion batteries and photocatalysts	306/2008
CeO_2	CeO_2 nanoflowers with controlled shape (cubic, four-petaled, and starlike)	Rapid thermolysis of $(NH_4)_2Ce(NO_3)_6$ in oleic acid/oleylamine	Catalysts in CO oxidation	307/2008
MnO_2	Monodisperse 3D manganese oxide nanoflowers	Reduction of potassium permanganate ($KMnO_4$) in deionized water with formamide ($HCONH_2$) at 40 °C	Supercapacitor electrode material	308/2009
MnO_4	Homogenous manganate nanoflowers	Microwave-assisted hydrothermal synthesis	Nuclear decontamination uses	117/2019
Bi_2O_3	Large-area arrays of 1D nanowires and nanoflowers of Bi_2O_3	Oxidative metal vapor phase deposition technique	—	83/2007
	Nonstoichiometric $Bi_2O_{2.33}$ nanoflowers	One-step solvothermal route using $NaBiO_3$ precursor in aqueous solution with PVP	—	103/2014
MgO	Magnesium oxide nanoflowers	Chemical precipitation method, sequential calcinations, and surface modification with acacia gum	Adsorbents for the removal of divalent metallic species from synthetic waste water	309/2015
ZnO	Flower-like ZnO nanostructures	Hydrothermal method in the absence of surfactants or organic solvents	—	310/2007
	ZnO nanoflowers on Si substrate	Seed-layer assisted solution route	Optical, optoelectronic and sensing devices	311/2010
	ZnO nanoflowers	Solution plasma	—	312/2011
	Flower-like ZnO-on-ZnO nanorod arrays on a zinc substrate	Low-temperature hydrothermal synthesis	—	313/2013
	ZnO nanoflowers	Biosynthesis using *Bacillus licheniformis* MTCC 9555	Photocatalysts	314/2014
	Hierarchical ZnO nanoflowers	PEG-20000 assisted hydrothermal synthesis	H_2S gas sensors	95/2015
	Three types of 3D fluffy ZnO nanoflowers	Direct hydrothermal reaction with/without ultrasonic treatment	Photocatalysts	87/2020
	Single-crystalline ZnO nanoflowers	Hydrothermal method with post-annealing treatment	Ultraviolet photodetectors	315/2021
	ZnO nanoflowers	Bioinspired synthesis using *Withania coagulans* extract as a reducing agent	Antibacterial agents and bioethanol production	108/2021
CdO	CdO nanoflowers on soda lime glass, fused silica glass, Si and ITO-coated glass	Sol–gel method	Photodetection application	316/2019

due to the faster formation of Ni hydroxide facilitated by higher $NH_3 \cdot H_2O$ content. Moreover, the size of the mesopores on the nanosheets remains around 10 nm. Notably, NiO–NF-3.0 exhibits the smallest mesopores (primarily 9.5 nm) and the thinnest nanosheets (approximately 15 nm), indicating a higher number of active sites and promising electrocatalytic performance. In the electrochemical nitrogen reduction reaction, the NiO–NF-3.0 electrode materials exhibit excellent electrochemical properties in 0.1 M Na_2SO_4.

Multifunctional nanoflowers composed of partial hydroxide nickel oxide (NiO_x) are grown on cotton fabric using a chemical bath deposition technique to develop UV filters and flexible gas/chemical sensors.[288] Nickel sulfate hexahydrate and potassium persulfate are mixed at room temperature, followed by the addition of an ammonium hydroxide solution to the prepared precursor solution under vigorous stirring. Pre-treated cotton cellulose samples are dipped in the prepared precursor solutions and kept undisturbed for 96 h, followed by hot-air-oven drying at 80 ± 6 °C for 1 h. At the beginning of the growth process, the Ni dissolved in potassium persulfate is immediately hydrolyzed and reacts with ammonium hydroxide to generate $Ni(OH)_2$ nuclei with an electrostatic driving force, minimizing the surface energy of cotton cellulose, promoting the growth of nanosheets.[289,290] A high saturation level facilitates the formation and enhancement of nucleation sites, whereas a low saturation level facilitates crystal growth. On increasing the reaction time, the growth of nanosheets increases through further nucleation and assembly, forming nanostructured NiO_x-3D-green-button chrysanthemum flowers on the cotton fabric (Fig. 12). The ultraviolet protection factor (UPF) indicates the number of UV rays (both UV-A and UV-B) blocked by the material.[288] The UPF of the nanoflower modified on cotton fabric, measured using a UV transmittance analyzer by an *in vitro* method according to the AATCC 183:2004 standard, is 2000. According to chemical/gas sensing measurements, the selectivity response of the NiO_x-modified fabric is 12 431 toward trimethylamine at room temperature. Additionally, it exhibits good thermal stability and increased hydrophobicity compared to unmodified materials. Owing to these excellent features, the nanostructured cotton fabric can be used as a flame retardant, hydrophobic screen, and protective suit against gas leaks and UV rays.

5.2.4. Other-metal-oxide nanoflowers. There are many other-metal-oxide nanoflowers, including Sn, Fe, Ce, Mn, Bi, Mg, Zn, and Cd. They have been summarized in Table 14 according to their synthetic methods, structures, and applications.

5.2.5. Conclusion. The reported articles on metal oxide nanoflowers, the most published topic in nanoflower research, are mainly focused on TiO_2, CuO, NiO, and ZnO. Many other metal-oxide nanostructures have also been studied. The ZnO nanoflowers synthesized by surface treatment have been reported in many publications, such as, ZnO–TiO_2 core–shell,[317] Ag-/Pt-doped ZnO,[318,319] and C-coated ZnO nanoflowers.[320] Metal oxide nanoflowers have been synthesized using various methods; one-third of the preparation routes use hydrothermal or solvothermal methods (Tables 11–14) under mild reaction conditions. According to Tables 11–14, metal oxide nanoflowers can be applied for wastewater treatment, catalysis, nuclear decontamination, and used as gas sensors, antibacterial agents, photodetectors, and supercapacitors. Research on metal oxide nanoflowers has focused on controlling their morphology and size under various reaction conditions, including the types and amounts of reagents (precursors, reducing agents, surfactants, and template agents), reaction time, and temperature, to determine the optimal structures for different applications.

Flower-like NiO nanostructures with three different morphologies are synthesized by a modified hydrothermal method by changing the volume of ammonia (25–28% wt%).[127] Each product exhibits unique morphology and different gas sensing ability. Ni *et al.* compared the electrochemical performances of the synthesized CuO nanoflowers with previously reported CuO-based nanomaterials, including nanoflowers prepared under different synthesis conditions, for H_2O_2 determination and glucose biosensing.[85]

5.3. Alloy nanoflowers

Bimetallic nanoparticles composed of two different metal elements have recently attracted significant attention as catalysts owing to their alloy effects or synergistic effects, resulting in enhanced catalytic performance compared to that of their corresponding monometallic counterparts.[321–325]

Pd is the most commonly used anode catalyst for formic acid oxidation in direct formic acid fuel cells,[326–328] and according to a size-effect study of the electro-oxidation of formic acid, Pd nanoparticles with optimal binding energy show the highest activity.[329,330]

Hybrid catalysts, such as, PdNi,[331] PdCo,[332,333] PdCu,[334] and PdIr[335] exhibit enhanced formic acid oxidation compared to single-component catalysts because of their synergistic effects that can manipulate the binding energy of Pd. A similar effect is expected for bimetallic-alloy nanoflowers.

5.3.1. Au-based nanoflowers. Multibranched Au–Pd bimetallic nanoflowers have been synthesized through a seeded reduction method by Ma and co-workers,[336] whereby seed-

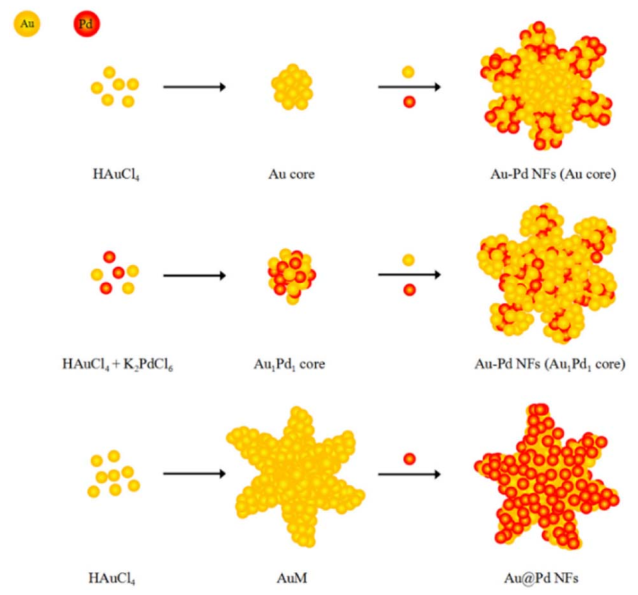

Scheme 5 Schematic illustration of the formation of three morphology-controlled Au–Pd nanoflowers (Au–Pd NFs) by seed-mediated growth. Adapted with permission from ref. 336. Published by MDPI. Copyright@ 2017 by Tao Ma *et al.*

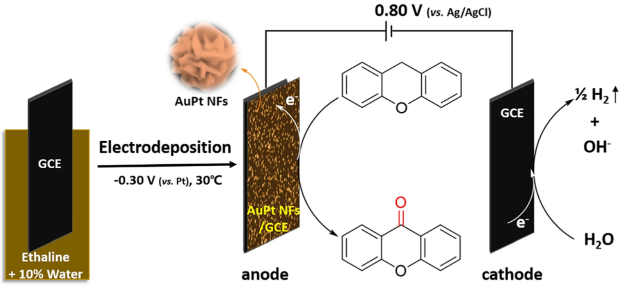

Fig. 13 Schematic illustration of the preparation of AuPt nanoflowers (AuPt NFs) and the electrochemical synthesis of xanthone from xanthene. Adapted with permission from ref. 341 Published by Springer Nature. Copyright © 2018, Aoqi Li *et al.*

mediated growth proceeds *via* two steps: (i) the reduction of a metal precursor to form uniform small seeds; and (ii) the reduction of another metal on the as-prepared seeds. The Au nanospheres are prepared as seeds in Au cores (∼16 nm size),[337] Au and Pd bimetallic nanoparticles (Au_1Pd_1 core, ∼20 nm size),[338] and Au nanostars (∼40 nm size).[337,339] Subsequently, Pd is deposited on these seed nanocrystals by a reduction process, forming Au–Pd nanoflowers with three different morphologies, as shown in Scheme 5. According to a recent study,[337] Au nanostars exhibit better catalytic activity than Au nanocages and nanoantennas, when 4-nitrophenol is reduced to its amino derivative, 4-aminophenol, with sodium borohydride ($NaBH_4$) at room temperature. The degradation of 4-nitrophenol is a crucial catalytic reaction in the fine-chemical and pharmaceutical industries owing to its convenient monitoring by UV-vis absorption spectroscopy.[340]

At a low potential of −0.30 V (*vs.* Pt) and a low temperature of 30 °C, flower-like AuPt alloy nanoparticles are synthesized by the one-step electrochemical reduction method.[341] In this method, deep eutectic solvents are used as shape-directing agents and solvents. Through the potentiostatic method, a standard three-electrode cell with a Pt wire counter electrode, a Pt quasi-reference electrode, and a GCE plate (15 mm × 10 mm × 1 mm) working electrode are used for the electrochemical-deposition synthesis of flower-like AuPt alloy nanoparticles in ethaline with 10% water (Fig. 13). Another promising strategy for electro-organic synthesis is mentioned next. The electrode modified with the as-prepared nanomaterials is utilized as the anode in the electrochemical oxidation reaction, using the GCE modified with AuPt nanoflowers, which is directly used to electrooxidize xanthene (XT) to xanthone (XO) with a high yield under a constant low potential (0.80 V *vs.* Ag/AgCl) at room temperature.

Imura *et al.* reported the preparation of bimetallic Au–Ag nanoflowers by reducing $HAuCl_4$ in a solution containing melamine (as the capping agent) and ascorbic acid (as the reducing agent), which are weakly adsorbed on the surface of the metal.[342] Bimetallic Au–Ag nanoflowers are obtained with a clean surface using a support (g-Al_2O_3)[38,343–347] and an extracting method (extracting the surface ligands with water).[348,349] A weakly adsorbing capping agent, adequate washing processes to remove capping agents from the metal surface, and a supporting method to inhibit aggregation are vital factors in obtaining surface-clean Au nanoflowers.[347] Bimetallic nanoflowers with clean surfaces are applied for the aerobic oxidation of 1-phenylethyl alcohol. Surface-clean Au nanoflowers and spherical Au–Ag nanoparticles of almost the same size and Au/Ag ratio exhibit lower rates for the oxidation of acetophenone than bimetallic nanoflowers.[347]

5.3.2. Pt-based nanoflowers.

Bimetallic alloyed $Pt_{71}Co_{29}$ lamellar nanoflowers (LNFs) with abundant active sites are fabricated *via* a one-pot solvothermal method in the presence of CTAC.[350] 1-Nitroso-2-naphthol (1-N-2-N) acts as a co-structure directing agent and coordinates with metal precursors to form stable complexes by controlling the size and morphology of nanomaterials,[351] whereas oleylamine acts as the solvent and reducing agent. A large number of PtCo nanoflowers with an average particle size of 20.4 nm are observed in the TEM image. The medium-magnification TEM images show each crystal assembled by many ultrathin nanoflakes with a flower-like architecture. The $Pt_{71}Co_{29}$ LNFs exhibit higher mass activity (MA, 128.29 mA mg^{-1}) for oxygen reduction compared to those of home-made $Pt_{48}Co_{52}$ nanodendrites, $Pt_{79}Co_{21}$ nanodendrites, and commercial Pt black, with values of 39.46, 49.42, and 22.91 mA mg^{-1}, respectively. The $Pt_{71}Co_{29}$ LNFs exhibit higher methanol oxidation (MA, 666.23 mA mg^{-1} and specific activity (SA), 2.51 mA cm^{-2}) than $Pt_{48}Co_{52}$ nanodendrites (MA, 213.91 mA mg^{-1}; SA, 1.99 mA cm^{-2}), $Pt_{79}Co_{21}$ nanodendrites (MA, 210.09 mA mg^{-1}; SA, 1.12 mA cm^{-2}), and Pt black (MA, 57.03 mA mg^{-1}; SA, 0.25 mA cm^{-2}).

A novel atmospheric microplasma induced liquid chemistry (AMILC) method has been applied for the controlled synthesis of 2D and 3D binary Pt_3Co nanoflowers by Wang *et al.*[352] As shown in the atmospheric microplasma (AMP) setup in Fig. 14, the electrolyte consists of 0.002 M chloroplatinic acid hydrate ($H_2PtCl_6 \cdot xH_2O$), 0.5 M sodium sulfate (Na_2SO_4), and variable molar concentrations of cobalt(II) sulfate heptahydrate ($CoSO_4 \cdot 7H_2O$) dissolved in distilled water (40 mL). Bimetallic Pt–Co nanostructures are generated on the cathodic Si

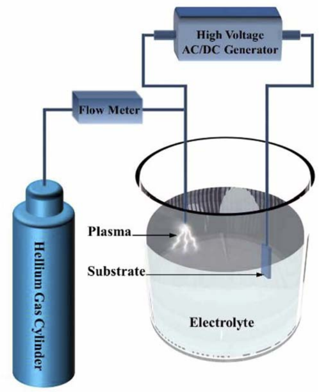

Fig. 14 Schematic diagram of the atmospheric microplasma-induced liquid chemistry synthesis method. Reprinted with permission from ref. 352. Copyright © 2020 IOP Publishing Ltd.

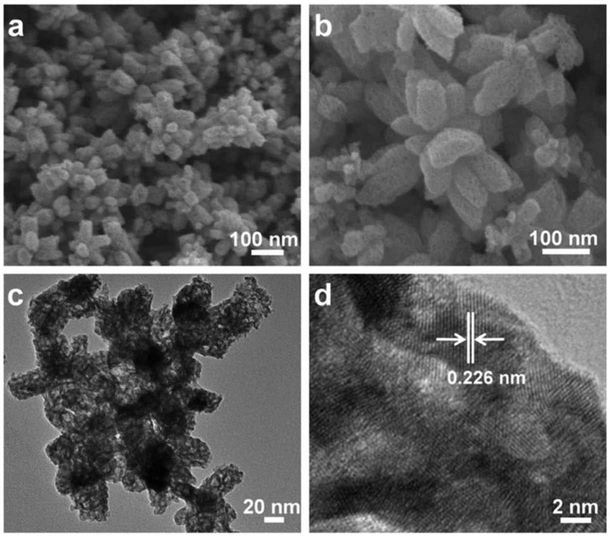

Fig. 15 SEM (a and b), TEM (c), and HR-TEM (d) images of the hnp–$Pt_{35}Cu_{65}$ alloy. Reprinted with permission from ref. 354. Copyright © 2017 Elsevier Inc.

substrate, half-inserted in the aqueous electrolyte and separated by at least 3 cm from the anodic capillary.

PtRu alloy nanoflower catalysts are synthesized by controlling their compositions through a solvothermal method and using oleylamine as a coordinating solvent, reductant, and surfactant, through the co-reduction of $H_2PtCl_6 \cdot 6H_2O$ and $RuCl_3 \cdot xH_2O$, without additional surfactants, reducing, or structure-directing agents.[353] These PtRu nanocatalysts exhibit different morphologies depending on the Pt/Ru ratio. The PtRu nanoflowers composed of nanodendrites exhibit excellent electrocatalytic properties toward methanol electro-oxidation through the normalization of the electrochemically active surface area for direct methanol fuel cells; these properties are derived from the synergetic effect between Pt and Ru and their unique 3D interconnected nanostructures.

Hierarchical nanoporous (hnp) PtCu alloy nanoflowers with different components are fabricated from a PtCuAl precursor alloy by selectively etching Al atoms, with different Pt and Cu ratios, by dissolving the Cu atoms partially.[354] In particular, the hnp–$Pt_{35}Cu_{65}$ sample exhibits superior catalytic activity compared to other PtCu catalysts with different Pt contents. The SEM images (Fig. 15a and b) reveal that each nanoflower consists of a cluster of nanorod-like leaves, approximately 50 nm in width and 100 nm in length. These leaves exhibit uniform interconnected nanopores measuring approximately 5 nm in size, spanning the entire sample. The TEM and HR-TEM images show flower-like structures with bimodal size distributions (Fig. 15c). Pores of various sizes corresponding to the bright region, confirm the formation of hierarchical nanoporous channels, whereas the dark skeleton is attributed to the interconnected nanoscale backbone. The HR-TEM image of hnp–$Pt_{35}Cu_{65}$ and the ordered lattice fringes are well-resolved in Fig. 15d; the hnp–$Pt_{35}Cu_{65}$ sample shows good structural stability in the hierarchical nanoporous flower-like architecture. The lattice spacing is determined to be 0.226 nm, indicating that it corresponds to the (1 1 1) crystal plane of the PtCu alloy.

5.3.3. Pd-based nanoflowers. A novel class of self-supported worm-like PdAg nanoflowers are fabricated with the assistance of CTAB under mild conditions.[125] Interestingly, the PdAg nanoflowers assemble to form a worm-like structure that can serve as a self-supported material to protect the relative supporters from severe corrosion and oxidation. The as-prepared Pd_1Ag_2 nanoflowers exhibit a narrow size distribution (29.27 ± 3.74 nm), which is much smaller than the average diameters of Pd_1Ag_1 (33.20 ± 4.23 nm) and Pd_1Ag_3 (32.48 ± 4.27 nm). Its homogeneous structure contains approximately 10 petals, exposing more surface-active area and increasing its activity towards ethylene glycol oxidation (EGOR).[358] Owing to its high active surface area of 42.36 $m^2 g^{-1}$, Pd_1Ag_2 nanoflowers display special electrocatalytic performances toward EGOR with mass and specific activities of 5545 mA mg^{-1} and 12.82 mA cm^{-2}, respectively, for direct ethylene glycol fuel cells, with 6.9

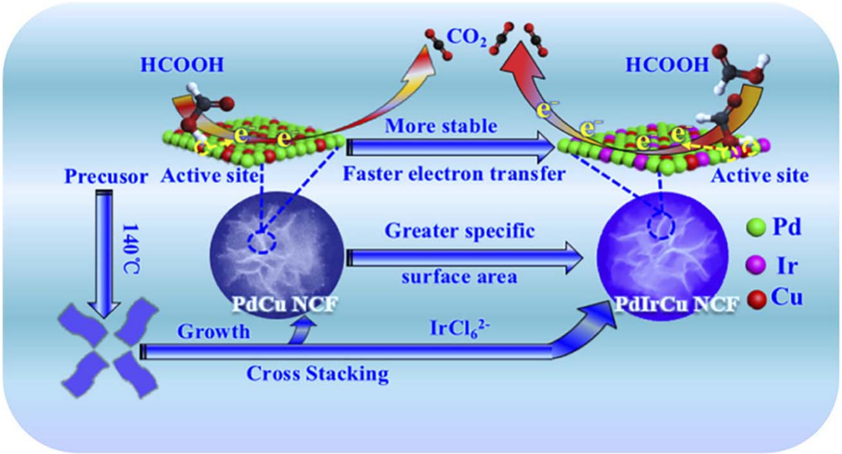

Fig. 16 Schematic illustration of the synthesis procedures and enhanced electrocatalytic performance mechanisms of the PdIrCu NCF catalyst. Reprinted with permission from ref. 360. Copyright © 2018, American Chemical Society.

and 2.1 times higher activity than that of commercial Pd/C, respectively.

Through a facile wet-chemical method, ultrafine 2D alloyed PdCu nanosheet-constructed 3D flowers are fabricated from a mixture of Na_2PdCl_4 and $CuCl_2 \cdot 2H_2O$ (metal precursors) in DMF (solvent), acetic acid (reducing agent), and $W(CO)_6$ (structural regulator).[359] As shown in TEM images, the flower-like Pd_2Cu nanoflowers consist of numerous ultrafine nanosheets. The optimal Pd_2Cu nanoflowers with a mass/specific activity value of 4714.1 mA mg^{-1}/13.7 mA cm^{-2} show significantly increased activity toward EGOR, with 4.4 and 6.85-fold increases relative to commercial Pd/C catalysts (1066.8 mA mg^{-1}/2.0 mA cm^{-2}). Pd_2Cu nanoflowers exhibit high long-term stability and are a novel class of cost-efficient electrocatalysts that are advantageous for fuel-cell reactions.

An Ir-alloyed ultrathin ternary PdIrCu nanosheet-composed flower (NCF) structure has been synthesized through a one-pot solvothermal reduction in the absence of any surfactant.[360] The Cu and Ir atoms together modify the electronic structure of Pd during synthesis, forming an unparalleled ultrathin NCF structure. The PdIrCu/C NCF catalyst exhibits significantly enhanced electrocatalytic activity compared to that of commercial Pd/C for formic acid electro-oxidation. Fig. 16 illustrates the preparation procedures and catalytic mechanism of PdCu and PdIrCu NCF for enhanced formic acid electro-oxidation. Initially, the precursor reactants are transformed into 2D NCFs, which are then cross-stacked into 3D NCFs. The enhanced electrocatalytic performance of PdIrCu/C NCF is attributed to the following: (1) a change in the electronic structure of Pd due to Pd, Ir, and Cu; easy formation of Ir–OH species at a lower potential by the unique surface chemistry of Ir, facilitating the oxidation of CO_{ad} and its removal from the active sites of catalysts, reducing the poisoning effect; (2) an increase in the specific surface area and formation of more available catalytic active sites by the ultrathin-nanosheet structure of PdIrCu/C; and (3) the enhancement of electroconductivity and promotion of the mass transport process in the electrocatalysis reaction by the unique 3D NCF structure.

5.3.4. Other-alloy nanoflowers. Other-alloy nanoflowers are fabricated using the reduction method, colloidal synthesis, and ultrasonication. The nanostructures and their applications as electrocatalysts for water splitting and fuel cells are summarized in Table 17.

5.3.5. Conclusion. Alloy nanoflowers are a recent research topic, with publications dating back to only 10 years; approximately 20–30 studies have been reported on Au-, Pt-, Pd-, Ni-, Mo-, and Ir-based alloy nanoflowers. The nanoflowers have been synthesized by various reduction methods,[341,342,354,355,361] the AMILC method,[352] solvothermal methods,[70,350,353,360] and so on.[115,116,336,357] Alloy nanoflowers primarily exhibit potential applications as electrocatalysts for water splitting and fuel cells (Tables 15–17) due to their alloy and synergistic effects.[321–325]

Table 15 Synthesis methods and applications of flower-like hierarchical Au-based alloy nanostructures

Compound	Variety of formed nanostructures	Synthesis method	Application	Ref./year
AuPt	AuPd nanoflowers on a polyamidoamine dendrimer-modified surface	Electrodeposition	Electrode materials, electrocatalysts	115/2006
AuAgCu	Hollow Au–Ag–Cu nanoflowers	Combined seed mediated and galvanic replacement method	Electrocatalysts for direct ethylene glycol fuel cells	116/2017

Table 16 Synthesis methods and applications of flower-like hierarchical Pt based alloy nanostructures

Compound	Variety of formed nanostructures	Synthesis method	Application	Ref./year
PtPd	Porous Pt–Pd alloy nanoflowers	One-pot cochemical reduction method in a poly(allylamine hydrochloride) based aqueous solution	Cathode electrocatalyst in direct alcohol fuel cells	355/2013
Pt_3Co	Pt_3Co nanoflowers	Solvothermal method without seeds and templates	Electrocatalysts in DMFCs	70/2014
PtAg	Multi-branched AgPt alloyed dendritic nanoflowers	One-pot successive aqueous coreduction strategy with the assistance of 3-aminopyrazine-2-carboxylic acid (Apzc) as a structure-directing agent	SERS	356/2017
PtPdAg	Porous ternary Pt–Pd–Ag alloy nanoflowers	Pd-seed mediated co-reduction	Cathode electrocatalyst in advancing fuel cell technology	357/2017

Table 17 Synthesis methods and applications of flower-like hierarchical other-alloy nanostructures

Compound	Variety of formed nanostructures	Synthesis method	Application	Ref./year
NiCo	NiCo nanoflowers	An amphiphilic polymer(Jeffamine)-assisted homogeneous polyol reduction method	Magnetorheological fluids	361/2014
MoWSe	$Mo_{1-x}W_xSe_2$ nanoflowers	Colloidal synthesis	Electrocatalysts for the hydrogen evolution reaction in both acidic and alkaline aqueous solutions	71/2017
IrCo IrNi	IrCo nanoflowers IrNi nanoflowers	Ultrasonication with $IrCl_3 \cdot xH_2O$, $Co(acac)_2$ or Ni(acac) and oleylamine, heated in a hot oil bath	Proton exchange membrane water electrolyzers	35/2019

Interestingly, research focuses on the morphologies and ratios of metals in the alloy system, because the latter can affect the former, thereby influencing catalyst performance. For instance, Zhang *et al.* reported that the formation of highly branched nanoflowers, can be induced by varying the Pt/Co ratio and controlling their size,[350] forming $Pt_{71}Co_{29}$ lamellar nanoflowers exhibiting higher mass activity for oxygen reduction than $Pt_{48}Co_{52}$ and $Pt_{79}Co_{21}$ nanodendrites.

5.4. Other nanoflowers

5.4.1. Silica nanoflowers. Porous silica (SiO_2) nanostructures have been intensely studied because of their unique features: high surface area, precise pore structure, tunable pore size, stability, high permeability, and biocompatibility.[362–369] However, research on the synthesis of silica nanomaterials with well-defined morphology and controllable size still has a long way to go. In particular, silica nanoflowers have been rarely reported.

Hierarchically structured spherical mesoporous silica nanoflowers (HSMNFs) with well-defined morphologies and uniform sizes are synthesized hydrothermally in a mixture of cyclohexane and water using CPB as the template. TEOS and urea are used as the source of inorganic silica and the hydrolysis additive, respectively.[120] The flower, with 200–500 nm size, approximately 10 nm petal thickness, contained 4.0 nm and *ca.* 40 nm mesopores and macropores, respectively, with up to 502 $m^2\ g^{-1}$ surface area. The nanoflower size, structure, and petal thickness strongly depend on the hydrothermal temperature and the molar ratio of Si to CPB; the optimal conditions are 120 °C (hydrothermal temperature) and 4.37 (molar ratio of Si to CPB). This material could be used for catalysis, adsorption, and controlled drug release in medicine because of its hierarchical porous structure, nanoflower morphology, and large surface area.

Dandelion flower-like silica nanoflowers with a uniform size, containing an accessible large surface area, have been synthesized through a visible-light-driven green chemistry method.[126] CTAB and urea are dissolved in water, while TEOS is added to a mixture of methyl phenyl ether and hexanol. Subsequently, both the solutions are mixed in a vial by stirring, followed by stirring under visible light (tungsten bulb) for 20 h at 90 °C. After cooling the mixed solution to room temperature, the products are collected and purified by filtration and washing, followed by air-drying and calcination (at 575 °C for 5 h under atmospheric conditions) to remove the structure-directing agent, CTAB. The TEM images indicate that the synthesized silica nanoflowers have a relatively narrow size distribution (with a diameter of 385 ± 5 nm), and the edges of the nanoflower are composed of elongated spikes oriented outwards in three dimensions (Fig. 17D–F).

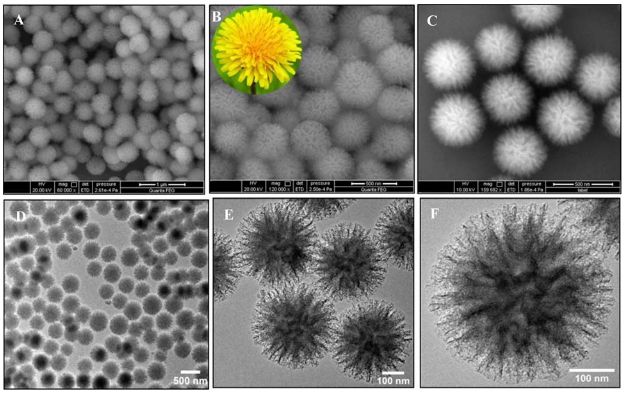

Fig. 17 (A–C) FE-SEM micrographs of SiO_2 nanomaterials at different magnifications, representing their hierarchical dandelion flower-like morphology. Photograph of a dandelion flower is presented in the inset of Fig. (B). TEM images of (D and E) a bunch of SNF and (F) a single SiO_2 nanoflower containing elongated spikes which assemble in a divergent way to form dandelion-like flowery morphology. Reprinted with permission from ref. 126. Copyright © 2019 Elsevier B.V. All rights reserved.

The SiO_2 nanoparticles are synthesized by modulating the chain length of alcohols from propanol to octanol, while maintaining the other reaction conditions, to investigate the effect of co-solvents on nanoflower morphology.

The TEM analysis indicates that the morphologies of SiO_2 nanoparticles are affected by the alcohol chain length. A noticeable flowery architecture encompassing elongated spikes is formed in higher chain-length alcohol co-solvents, which

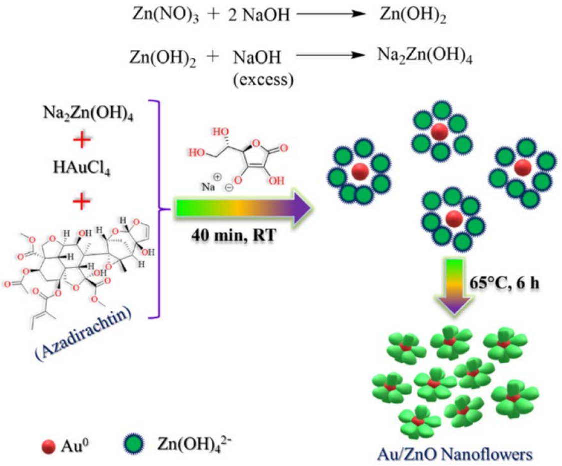

Scheme 6 Schematic chart of the fabrication procedure of Au/ZnO hybrid nanoflowers using *A. indica* (neem) leaf extract. Reprinted with permission from ref. 79. Copyright © 2021, American Chemical Society.

becomes persistent for hexanol to octanol. Additionally, the specific surface area gradually increases with increasing chain length of the alcohols (propanol to octanol), remaining almost constant beyond hexanol (Table 5). Amine-functionalized SiO_2 nanoflowers have been synthesized using (3-aminopropyl)triethoxysilane (SNF-1), *N*-[3-(trimethoxysilyl) propyl]ethylenediamine (SNF-2), and *N*1-(3-trimethoxysilyl propyl) diethylenetriamine (SNF-3), respectively, for use as a CO_2 adsorbent. Furthermore, chromogenic-functionalized SiO_2 nanoflower composites have been fabricated from amine-functionalized nanoflowers for the detection of CO_2.

5.4.2. Metal–metal oxide nanoflowers. Au/ZnO hybrid nanoflowers are fabricated by an easy, eco-friendly, and low-cost synthetic method employing *A. indica* (neem) leaf extract as a reducing and capping agent.[79] Some biomolecules in *A. indica* leaves (such as ascorbate, a natural reducing agent) reduce Au^{3+} ions to Au^0, attracting the negatively charged zincate ions to the active surface of Au^0. They deposit on the Au surface and grow as multiple ZnO petals *via* the thermal decomposition of sodium zincate [$Na_2Zn(OH)_4$] (Scheme 6).

The BET surface area of catalysts toward ZnO, Au, and Au/ZnO hybrid nanoflowers have been measured; the BET surface area of Au/ZnO nanoflowers is 19.23 $m^2\ g^{-1}$ for the reduction of 4-nitrophenol to 4-aminophenol, which is wider than that of the others (Table 18). Additionally, the activation energy of the Au/ZnO hybrid nanoflowers (32.46 ± 1.62 kJ mol^{-1}) is lower than that of ZnO (57.75 ± 2.85 kJ mol^{-1}) and Au (48.40 ± 2.41 kJ mol^{-1}). Thus, Au/ZnO hybrid nanoflowers exhibit higher catalytic activity for nitro reduction compared to ZnO and Au. Other metal–metal oxides have been developed as catalysts, electrode materials, and theranostic agents (Table 19).

5.4.3. Nanoflowers with core–shell structure. Different physical and chemical procedures have been used to fabricate core–shell nanoflower materials, including various modified hydrothermal/solvothermal processes, and templating methods, as shown in Tables 20 and 21. Most research has focused on the influence of constituents and active sites of the surface shell of nanoflowers and core–shell nanostructural features on the electrochemical, catalytic, and optical properties, to utilize them in gas sensors, catalysts, supercapacitors, lithium-ion batteries, biosensors, antibacterial agents, and for water splitting (Tables 20 and 21). This section introduces the synthetic strategies, morphologies, physical and chemical properties, and applications of core–shell nanoflowers.

5.4.3.1. Au-core nanoflowers. As mentioned in Section 5.3.1, Au-based Nanoflowers, Au@AuPd (Au–Pd NFs with Au cores, shown in Scheme 5), and Au@Pd (Au@Pd NFs) core–shell nanoflowers are fabricated by a seed-mediated reduction method, whereby Au nanoparticles as seeds induce the growth of a layer of Au and Pd petals and Pd nanoparticles decorated Au nanoflowers as seeds, respectively (Scheme 5).[336] The catalytic activities for 4-nitrophenol reduction are in the order of Au@Pd core–shell nanoflowers (Au@Pd NFs) > Au–Pd alloy nanoflowers (Au–Pd NFs (Au_1Pd_1 core)) > Au@AuPd (Au–Pd NFs (Au core)) core–shell nanoflowers. Thus, the content and reactive surfaces of Pd in the alloys affect their catalytic activities.[336]

Xu *et al.* reported the synthesis of Au@Pd core–shell nanoflowers through the reduction of Pd ions by hydroquinone on gold seeds.[371] Yin *et al.* synthesized Au@Pd core–shell mesoporous nanoflowers with Au nanoparticles coated with mesoporous Pd petals, using poly(styrene)-*b*-poly(ethylene oxide) (PS-*b*-PEO) as a polymeric micelle-assembled template to induce mesopores in Pd petals by the seed-growth method.[372] A facile one-pot synthesis of Au–Pd@Pd core–shell nanoflowers has also been performed in an aqueous polyallylamine solution.[373]

The Au@CdSe NFs are synthesized *via* one-pot heterogeneous nucleation and growth. Au nanoparticles are produced by injecting an $HAuCl_4$ solution into an alkyl amine (oleylamine or hexadecylamine) at room temperature, followed by increasing the temperature gradually to 150 °C or 300 °C,[128] adding trioctylphosphine oxide to the reaction mixture, and injecting

Table 18 Summary of the activation energy (E_a), pre-exponential factors (A), entropy of activation (ΔS), and surface area from the BET study for ZnO, Au, and Au/ZnO nanoflowers for the reduction of 4-nitrophenol to 4-aminophenol. Reprinted with permission from ref. 79. Copyright © 2021, American Chemical Society

System	E_a (kJ mol^{-1})	A (min^{-1})	ΔS (J mol^{-1} K^{-1})	Surface area ($m^2\ g^{-1}$)
ZnO	57.75 ± 2.85	2.36–2.54 ($\times 10^8$)	160.76 ± 4.82	7.79
Au	48.40 ± 2.41	1.39–1.62 ($\times 10^7$)	137.2 ± 4.11	8.64
Au/ZnO nanoflowers	32.46 ± 1.62	1.15–1.74 ($\times 10^5$)	98.5 ± 2.94	19.23

Table 19 Synthesis methods and applications of flower-like other metal–metal oxide nanostructures

Compound	Structure	Synthesis method	Application	Ref./year
$FeTiO_3$	Ilmenite $FeTiO_3$ nanoflowers	High-energy ball-milling of ilmenite and subsequent mild hydrothermal treatment in 1 M NaOH aqueous solution	Electrode materials for supercapacitors	60/2011
FeMnO	$Fe_{0.6}$ $Mn_{0.4}O$ nanoflowers	High-temperature thermal–decomposition reaction	Theranostic agent with T_1–T_2 dual-mode MRI for diagnostic purposes, and combined with magnetic hyperthermia for effective therapeutics	370/2016
$NiCo_2O_4$	$NiCo_2O_4$ nanoflowers	Microwave synthesis	Catalysts for the electro-oxidation reaction of methanol in DMFCs	73/2019

Table 20 Synthesis methods and applications of flower-like Au core nanostructures

Core	Shell	Structure	Synthesis method	Application	Ref./year
Au	Pd	Nanoflowers with an Au core and Pd petals	Seed-mediated growth method	Catalysts for Suzuki coupling reaction	371/2011
		Au@Pd core–shell mesoporous nanoflowers	Seed-mediated growth method	Catalysts of methanol oxidation reaction for DMFCs	372/2021
AuPd	Pd	Au–Pd@Pd core–shell nanoflowers	Polyallylamine-assisted water-based synthesis	Electrocatalyst for ethanol electro-oxidation	373/2015
Au	AgAu	Au@AgAu alloy nanoflowers	Deposition of $HAuCl_4$ on the surface of Au@Ag core–shell nanoparticles	Antibacterial agents	375/2018
Au	Rh	Au@Rh core–shell nanoflowers	Seeded growth	Electrocatalysts for the hydrogen evolution reaction	376/2021

CdO in oleic acid and Se in trioctylphosphine multiple times under stirring. As shown in Scheme 1, the CdSe clusters are adsorbed on the surface defects of the Au core and grow as multiple arms and branches after the injection. Using hexadecylamine instead of oleylamine or increasing the reaction temperature to 300 °C forms larger Au cores, improving the interface between the Au and CdSe domains to produce a core–shell structure. The Ag@CdSe nanoflowers are also prepared using the same synthetic strategy.

The Au@AgPd core–shell nanoflowers are synthesized by a seed-mediated reduction method. First, Au seeds with a narrow size distribution of 13.5 ± 1.0 nm are synthesized by the citrate reduction of $HAuCl_4 \cdot 4H_2O$. Subsequently, $AgNO_3$ and H_2PdCl_4 are co-reduced by L-ascorbic acid to grow on the surface of the Au seeds using CTAB, which assists the AgPd to bloom on the Au seed.[374] The size distribution of Au@AgPd nanoflowers is narrow, with a diameter of 38.4 ± 2.1 nm, branch length of 10.5 ± 1.3 nm, and width of 5.4 ± 0.7 nm. According to inductively coupled plasma mass spectrometry (ICP-MS) analysis, the weight percentages of Au, Ag, and Pd in the Au@AgPd nanoflowers are 14.2%, 40.6%, and 45.3%, respectively, consistent with the ratio of Au/Ag/Pd in the precursors. Compact branches are rarely observed on large Au cores, especially over 60 nm, whereas tiny Au seeds exhibit dense branches on their surface. The Au@AgPd nanoflowers could be applied for the *in situ* SERS monitoring of the catalytic reaction of 4-nitrothiophenol to 4-aminothiophenol.

5.4.3.2. ZnO-core nanoflowers. Harito *et al.* reported PbO_2-decorated $ZnO@TiO_2$ core–shell nanoflowers. First, a bicarbonate electrolyte produces flower shaped ZnO nanowires on the Zn plate surface by an electrochemical anodizing process[317] performed at a cell voltage of 5 V in 30 mM sodium bicarbonate, to produce the optimized uniform ZnO nanoflowers, according to FE-SEM analysis. Second, a layer of TiO_2 is coated on the surface of the ZnO nanoflowers *via* dip coating and calcination to enhance its properties for the photocatalytic degradation of organic dyes. Third, PbO_2 is deposited over the $ZnO@TiO_2$ core–shell nanoflowers using anodic electrodeposition, which is applied for the electrochemical oxidation of the dye. These nanoflowers can be used as catalysts for wastewater treatment.

5.4.3.3. Other core–shell nanoflowers. Other core–shell nanoflowers composed of Pd Ag, Fe, Mn, Ni, and Co have been reported for applications in catalysts, anode materials, sensors, and supercapacitors, as shown in Table 21.

5.4.3.4. Conclusion. Core–shell nanoflowers have been investigated in the past decade, with a small number of published papers. The introduced core–shell nanostructures have been fabricated using various modified hydrothermal or solvothermal processes, solution phase synthetic methods, and so on (see Tables 20 and 21). The components of the reported core–

Table 21 Synthesis methods and applications of flower-like other core–shell nanostructures

Core	Shell	Structure	Synthesis method	Application	Ref./year
Pd	Pt	Pd-core Pt-shell nanoflowers supported on carbon	Coreduction method	Catalysts for the oxygen reduction reaction of fuel cells	377/2018
		Pt deposited on Pd nanoflowers	Coreduction of Pd and Pt precursors with *N*,*N*-dimethylformamide and CTAC as the structure directing agent	Catalysts for methanol oxidation reaction of fuel cells	378/2020
Ag	NiO	NiO layer deposited on Ag nanoflower arrays on a Cu substrate	One-step solution-immersion process and subsequent RF-sputtering method	Anode materials for lithium-ion batteries	82/2015
Fe_3O_4	MnO_2	Fe_3O_4@MnO_2 core–shell nanoflowers	Solvothermal method	Colorimetric detection of phenol in wastewater	379/2015
$MnCo_2O_4$	$Ni(OH)_2$	$MnCo_2O_4$@$Ni(OH)_2$ multicomponent core–shell nanoflowers on Ni foam	Stepwise hydrothermal process	Supercapacitor electrodes	380/2016
Co_3O_4	$NiCo_2S_4$	Ultrathin $NiCo_2S_4$ shell on porous Co_3O_4 nanoflower array on a Ni-foam substrate	Stepwise hydrothermal process	Supercapacitors	381/2017
$NiCo_2O_4$	MnO_2	MnO_2@$NiCo_2O_4$ core–shell nanoflowers on Ni-foam	Hydrothermal process and calcination	Supercapacitors	382/2021

Table 22 Synthesis methods and applications of doped flower-like metal or metal-oxide-based nanostructures

Core	Doping	Structure	Synthesis method	Application	Ref./year
ZnO	Pt	Pt-doped on ZnO nanoflowers	One-step hydrothermal method	Solar cells and gas sensors	319/2010
	Ag	Ag-doped ZnO nanoflowers on the substrate	Low-temperature hydrothermal process	NO gas sensors	318/2018
SnO_2	Zn	Zn-doped SnO_2 nanoflowers	Hydrothermal method	Photoanode materials for dye-sensitized solar cells	384/2011
TiO_2	Ni	Ni-doped rutile TiO_2 nanoflowers	Acid treatment of the precursor hydrogen titanate nanowires and immersing the nanowires in an aqueous H_2SO_4 solution containing $NiSO_4$	Photocatalysts for wastewater treatment	37/2016
CeO_2	Fe	Porous Fe_x-doped $Ce_{1-x}O_2$ with flower-like morphology	Citric acid-assisted hydrothermal process	Catalysts for H_2S-selective oxidation	385/2020
Mo_2C	N	N-doped porous molybdenum carbide nanoflowers	Templating method and calcination using Pluronic F127, dopamine hydrochloride, and ammonium molybdate	Acetylcholinesterase (AChE) biosensors for detecting organophosphorus pesticides	386/2021

shell nanoflowers become increasingly complex from the simple bimetallic Au@Pd[371,372] and Pd@Pt[377,378] core–shell nanoflowers to the $NiCo_2O_4$@MnO_2 core–shell nanoflowers.[374] The composition ratio of the core–shell nanoflowers is one of the leading factors that affect the shape of the nanomaterial and its catalytic performance. For example, closely spaced and uniformly branched Au@AgPd core–shell nanoflowers are synthesized when the ratio of Pd/Ag is 1 : 1, exhibiting high catalytic activity owing to its small size, highly dispersed alloy shell, and defect abundance.[374] The size of Au@Rh nanoflowers increases with an increase in the amount of $RhCl_3$ added as the precursor. The $Au_{68}Rh_{32}$ nanoflowers with high Rh content exhibit high performance in the hydrogen evolution and plasmon-enhanced hydrogen evolution reactions.[376]

5.4.4. **Doped nanoflowers.** Yang *et al.* synthesized nickel-doped walnut-like MnO_2 nanoflowers using a template-less and surfactant-less hydrothermal method.[383] A strong Ni peak is observed in energy-dispersive spectroscopy (EDS) analysis, indicating the doping of Ni cations in the prepared nanoflowers. According to SEM images, the Ni-doped MnO_2 nanoflowers are composed of many interleaving thin nanosheets, and the diameter of the nanoflowers is approximately 5 μm. Their cyclic voltammograms, galvanostatic charge/discharge, and electrochemical impedance spectroscopy experiments indicate high specific capacitance (153.6 F g^{-1} at 1 A g^{-1}) and outstanding cycling stability (a capacitance retention of 103% after 1000 cycles). These properties are primarily attributed to their hierarchical walnut-like architecture. The Ni-doped MnO_2

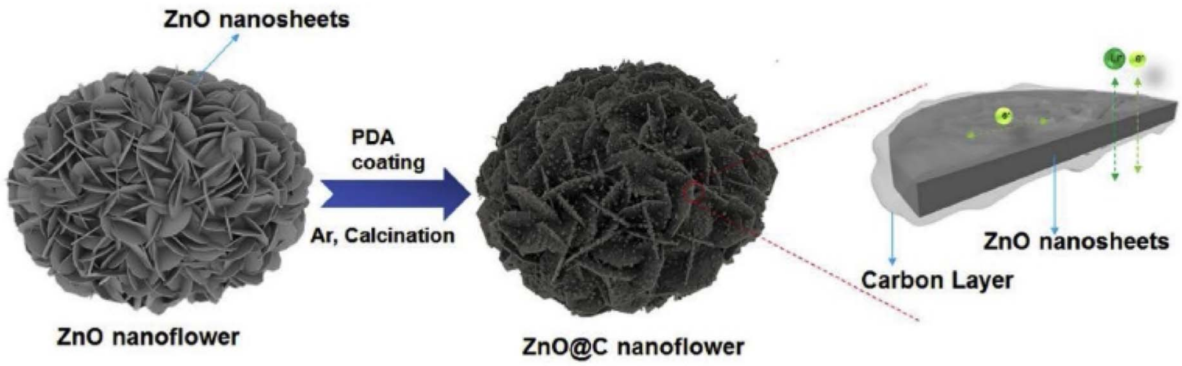

Scheme 7 Schematic illustration for the synthesis of ZnO@C nanoflowers. Reprinted with permission from ref. 320. Copyright © 2018 Elsevier B.V. All rights reserved.

nanomaterials have potential applications in supercapacitors owing to their excellent electrochemical performances (Table 22).

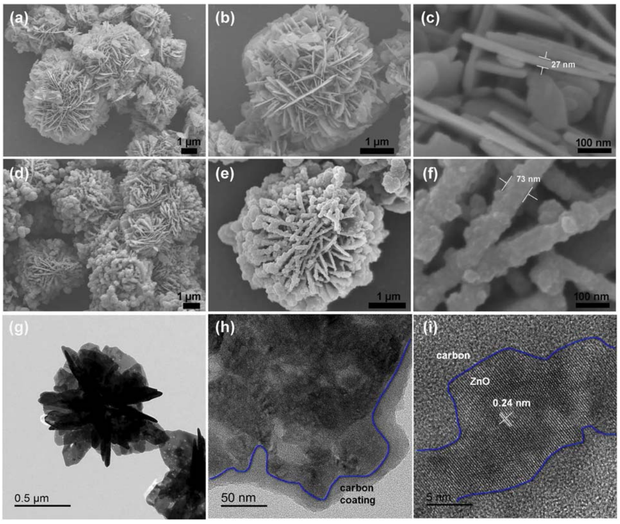

Fig. 18 SEM images at different magnifications: (a) low, (b) medium, and (c) high magnification images of pure ZnO nanoflowers; (d) low, (e) medium, and (f) high magnification images of ZnO@C nanoflowers. (g and h) TEM images and (i) HR-TEM image of ZnO@C nanoflowers. Reprinted with permission from ref. 320. Copyright © 2018 Elsevier B.V. All rights reserved.

5.4.5. Coated nanoflowers. Liu and colleagues have fabricated ZnO@C nanoflowers *via* a facile, fast, and low-cost synthetic route.[320] In the approach, $Zn(NO_3)_2 \cdot 6H_2O$ and $C_6H_5Na_3O_7 \cdot 2H_2O$ are mixed in an aqueous solution with controlled pH, followed by hydrothermal processing at 100 °C, assembling ZnO nanosheets into flower-shaped ZnO nanoparticles. Dopamine hydrochlorides are added to the suspension of ZnO nanoflowers and Tris-buffer (pH = 8) under magnetic stirring to form polydopamine (PDA)-coated ZnO nanoflowers (Scheme 7). The coated nanoflowers are carbonized under an Ar atmosphere to obtain C-layer-encapsulated ZnO nanoflowers. The SEM and TEM images (Fig. 18) indicate ZnO@C nanoflowers with diameters in the range of 2–6 μm, nanosheet petals with ~27 nm thickness, and a carbon layer with ~46 nm thickness. The ZnO@C nanoflower electrodes in lithium-ion batteries show a high capacity (approximately 1200 mA h g^{-1} at 0.1 A g^{-1} after 80 cycles), good cycling stability (638 and 420 mA h g^{-1} at 1 and 5 A g^{-1}, respectively, after 500 cycles), and excellent rate capability because of their micro–nano secondary architecture and chemical interactions between ZnO and the C layer (Table 23).

5.4.6. Nitride, sulfide, phosphide, selenide, and telluride nanoflowers. Nitride, sulfide, phosphide, selenide, and telluride nanoflowers combined with metals (Ti, Bi, Cd, V, Mo, and Zn) and bimetals (MnIn, NiCo, FeCo, and CuCo) are summarized in Table 24. Zn, Nd, Mo, Ru, and Co-doped or Au nanoparticles decorated with sulfide and selenide nanostructures are summarized in Tables 25 and 26, respectively.

Table 23 Synthesis methods and applications of coated flower-like metal or metal oxide nanostructures

Core	Coating	Structure	Synthesis method	Application	Ref./year
Au	SiO_2	Silica-coated Au nanoflowers on alumina	(1) Melamine assisted surfactant-free synthesis[134] (2) Addition of α-Al_2O_3 (ref. 38 and 347) (3) Silica coating using TEOS[387,388]	—	38/2017
Fe_3O_4	C	Fe_3O_4 nanoflowers coated by a black C layer	One-pot solvothermal route	Biosensors	39/2020

Table 24 Synthesis methods and applications of flower-like nitride, sulfide, phosphide, selenide, and telluride nanostructures

Compound	Structure	Synthesis method	Application	Ref./year
TiN	TiN nanoflower buds	Ammonialization of hydrothermally prepared titanium dioxide nanobuds	Pt-free counter electrodes for DSSC	40/2021
Bi_2S_3	Bi_2S_3 nanoflowers on Si substrates	Vapor deposition process	Nanoscale photodetectors and optical switches	60/2008
CdS CdSe	CdS and CdSe nanoflowers, branched nanowires, and nanotrees	Solvothermal method using $Cd(Ac)_2 \cdot 2H_2O$ and $CS(NH_2)_2$ or Na_2SeO_3 in a mixed solution made of diethylenetriamine and deionized water	Branched CdS nanowires can be applied as photocatalysts for the degradation of acid fuchsin	57/2006
VS_2	1T-VS_2 nanoflowers	Hydrothermal method using $Na_3VO_4 \cdot 12H_2O$ and CH_3CSNH_2	Electrocatalysts for the hydrogen evolution reaction	58/2017
MoS_2	MoS_2 nanoflowers	Green hydrothermal synthesis from ammonium molybdenum hydrate and thiourea without using any acids or bases	Photocatalysts for the degradation of methylene blue and crystal violet dyes under natural sunlight	389/2018
	MoS_2 nanoflowers	Hydrothermal method	Phase-change materials for thermal energy storage	390/2021
MnInS	$Mn_{0.4}In_{1.6}S_3$ nanoflower solid solutions	Hydrothermal method	Photocatalysts	41/2019
NiCoP	$Ni_{0.7}Co_{0.3}P$ nanoflowers	Hydrothermal–phosphorization method	Electrocatalysts for water splitting in alkaline media	42/2019
NiCoP FeCoP	NiCoP nanoflowers or FeCoP nanoflowers on Ni foam	Hydrothermal and low-temperature phosphating method	Supercapacitors	391/2021
CuCoP	Hydrangea-like $CuCoP_x$ nanoflowers	Solvothermal and phosphating method	Electrocatalysts for the methanol oxidation reaction	392/2021
ZnSe	Particle- and flower-shaped ZnSe nanocrystals	Green chemical approach	—	393/2008
	ZnSe rose-like nanoflowers or microspheres on Zn foil	Hydrothermal method	—	394/2014
$MoSe_2$	Colloidal $MoSe_2$ nanoflowers	Colloidal synthesis	—	88/2015
	$MoSe_2$ nanoflowers on carbon cloth	Chemical vapor deposition	Electrocatalysts	80/2018
Bi_2Se_3	Hierarchical Bi_2Se_3 nanoflowers	Hot-solution injection method at relatively low temperature (130 °C)	Photocatalysts in the presence of H_2O_2	43/2018
ZnTe	ZnTe nanoflowers, nanodots, and nanorods	High temperature-injection method using zinc stearate as precursors and trioctylphosphine or tributylphosphine as activating agents	—	44/2007

Table 25 Synthesis methods and applications of doped flower-like sulfide and selenide nanostructures

Core	Doping	Structure	Synthesis method	Application	Ref./year
CuS	Zn	Zn-doped CuS nanoflowers	Ethanol solvothermal process	Photoelectric and photocatalytic applications	101/2016
Bi_2Se_3	Nd	Nd^{III} doped Bi_2Se_3 nanoflowers	Hydrothermal synthesis	—	395/2009
	Mo	Mo-doped Bi_2Se_3 nanoflowers	Solvothermal method	Absorbents for the removal of organic dyes from wastewaters	102/2013
$MoSe_2$	Ru	Ru-doped $MoSe_2$ nanoflowers	Colloidal process	Catalysts of the hydrogen evolution reaction	89/2019
	Co	Homogeneously Co-doped and Co-edge doped $MoSe_2$ nanoflowers	Colloidal synthesis (1) Addition of the dopant atoms to the mixture at the beginning of the reaction (2) Hot injection method	Catalysts for the hydrogen evolution reaction at the cathode of an electrochemical water splitting cell	90/2020

Table 26 Synthesis methods and applications of nanoparticle-decorated flower-like sulfide and selenide nanostructures

Core	Surface	Structure	Synthesis method	Application	Ref./year
MoS_2	Au	MoS_2 nanoflowers decorated with Au nanoparticles	Hydrothermal process	Gas sensors	61/2021
Bi_2Se_3	Au	Au nanoparticles decorated Bi_2Se_3 nanoflowers	Colloidal synthesis method	Catalyst for the hydrogen evolution reaction	91/2019

6. Applications of nanoflowers

Several studies on the properties of nanoflowers have demonstrated promising potential in various applications as catalysts, sensors, supercapacitors, wastewater treatments, chemical reactions, and green energy sources.

6.1. Nanoflowers for catalysis

Nanoflowers with highly branched structures exhibit a reasonably large specific surface area and high specific activity (*i.e.*, activity per unit surface area) because of the high densities of the edges, corners, and stepped atoms on their branches.[139] Thus, the study of catalysis by nanoflowers is of special interest.

6.1.1. Chemical catalysts. Au nanoflowers are effective catalysts for the reduction of nitroaromatic pesticides, including pendimethalin, trifluralin, and *p*-nitrophenol, in the presence of $NaBH_4$. They show high efficiency and fast reaction.[139] Additionally, the morphologies of the Au nanomaterials strongly affect their catalytic activity. According to catalytic studies of Au nanoflowers, nanostars and nano-snowflakes show high catalytic activity toward the reduction of *p*-nitrophenol in aqueous solutions. The catalyst capacity varies according to the shape, in the following order: Au nanoflowers < Au nanostars < Au nanoflakes; Au nanoflakes, with sharp tips, have the highest reducing power due to the availability of more surface atoms for catalysis.[136]

The catalytic activities of Au–Pd nanoflowers for the reduction of 4-nitrophenol exhibit the following order: Au@Pd nanoflowers (AuPd alloy) > Au–Pd nanoflowers (Au_1Pd_1 core) > Au–Pd nanoflowers (Au core). This could be attributed to the different contents and exposed reactive surfaces of Pd in the alloys.[336]

Bimetallic Au–Ag nanoflower catalysts with a clean surface exhibit higher reaction rates for acetophenone formation than those with Au nanoflowers and spherical nanoparticles of almost the same size and Au/Ag ratio.[342] Additionally, the catalytic activities of flower-like NiO for the oxidation of CO[292] and Au@Pd core–shell nanoflowers for the Suzuki coupling reaction[371] have been studied.

Zhou *et al.* have reported on the utilization of nanoporous Pt–Cu alloy nanoflower catalysts for the hydrolytic dehydrogenation of NH_3BH_3, a promising hydrogen storage material.[354] The as-prepared hnp–PtCu catalysts exhibit better catalytic performance than pure Pt and Cu catalysts. Also, the hnp–$Pt_{35}Cu_{65}$ sample, characterized by its stable hierarchical nanoporous flower-like architecture, exhibits superior catalytic performance compared to other PtCu catalysts with different Pt contents. This confirms the significant influence of the Pt-to-Cu ratio on catalytic activity. Table 27 provides the turnover frequency (TOF) values and activation energy (E_a) of all catalysts in the hydrolytic dehydrogenation of NH_3BH_3. The values for the $Pt_{35}Cu_{65}$ sample are comparable to or higher than those reported for most Pt-based or other noble metal-based catalysts.

6.1.2. Electrocatalysts. Fuel cells are considered to be an efficient green energy source.[404] Their performance mainly relies on the electrocatalysis of the oxygen reduction reaction and fuel electro-oxidation (*e.g.*, methanol or ethanol oxidation reactions) by the cathode and anode.[405] The electrocatalytic activity and stability of Pt–Pd alloy nanoflowers for the ORR have been investigated by rotating disk electrode voltammetry, whereby the nanoflowers exhibit superior ORR activity, long-term durability, and methanol tolerance in acidic media due to their unique porous structure and alloy properties.[368] Additionally, the electrocatalytic mass-activity, specific activity, and durability of AuPd@Pd core–shell nanoflowers toward the ethanol oxidation reaction are significantly higher than that of commercial Pd black.[373]

Mesoporous NiO nanoflowers consisting of crossed nanosheets, are synthesized using Pluronic F127 as a micellar

Table 27 Catalytic activities and the E_a of catalysts in the hydrolysis of NH_3BH_3. Reprinted with permission from ref. 354. Copyright © 2017 Elsevier Inc[a]

Catalyst	TOF (mol H_2 mol_M^{-1} min^{-1}) M = Pt, Ru and Ag	E_a (kJ mol^{-1})	Ref.
RuCu nanoparticles/ graphene	135	30.39	396
Pd–Pt@PVP nanoparticles	125	51.7	397
hnp–$Pt_{35}Cu_{65}$ nanoflowers	108	40.5	354
$Ag_{0.3}Co_{0.7}$ nanoparticles/PAMAM	52.8	35.66	398
Pd–Pt (1 : 1) nanoparticles	51.9	—	399
PdPt cubic nanoparticles	50.02	21.8	400
$Pt_{0.65}Ni_{0.35}$ nanoparticles	44.3	39.0	401
PtPd spherical nanoparticles	22.51	57.3	400
RuCu (1 : 1)/γ-$A1_2O_3$	16.4	52	402
Cu nanoparticles/RGO	3.61	38.2	403

[a] PVP: poly(*N*-vinyl-2-pyrrolidone), PAMAM:multifunctional poly(amidoamine), RGO: reduced graphene oxide.

Table 28 Performance comparison of the other NiO electrodes for electrocatalytic ammonia synthesis. Adapted with permission from ref. 286. Copyright © the Royal Society of Chemistry 2021

Catalyst	Electrolyte	Yield (μg h^{-1} $mg^{-1}_{cat.}$)	FE (%)	Ref.
Pd nanoparticles	0.1 M PBS	4.5	8.2%	408
Pd–Ag–S nanosponges	0.1 M Na_2SO_4	9.73	18.41%	409
Mn_3O_4 nanocubes	0.1 M Na_2SO_4	11.6	3%	410
Fe_2O_3 nanorods	0.1 M Na_2SO_4	15.9	0.94%	411
NiO nanodots on graphene	0.1 M Na_2SO_4	18.6	7.8%	412
N-C@NiO nanosheets on graphite paper	0.1 M HCl	14.022	30.43%	413
NiO nanoflowers	0.1 M Na_2SO_4	16.16	9.17%	286

template (synthesis details can be found in Scheme 4).[286] The process of assembling the interface is controlled by adjusting the amount of $NH_3 \cdot H_2O$, which led to the ability to modify the thickness and dimensions of the mesoporous NiO nanosheets. These nanoflowers are utilized for electrochemical nitrogen reduction reaction (NRR), a sustainable method for NH_3 synthesis that offers a viable alternative to the industrial energy and Haber–Bosch process under ambient conditions.[406,407] NRR measurements demonstrate that NiO–NF-3.0, having the smallest mesopores and the thinnest nanosheets in all NiO–NF samples, exhibits excellent NRR performance, with an NH_3 yield of 16.16 μg h^{-1} $mg^{-1}_{cat.}$ and faradaic efficiency (FE) of 9.17% at −0.4 V *vs.* reversible hydrogen electrode in 0.1 M Na_2SO_4. X-ray photoelectron spectroscopy (XPS) confirms the presence of Ni^{2+} and Ni^{3+} in all NiO–NF samples, with NiO–NF-3.0 displaying the highest Ni^{3+} content, correlating with its superior electrochemical NRR performance. This can be attributed to the electropositivity promotion of NiO-NFs by Ni^{3+}, facilitating the adsorption of N_2 gas and enhancing the electrocatalytic properties. The NRR performances of the five different NiO–NF electrodes follow the order: NiO–NF-3.0 > NiO–NF-5.0 > NiO–NF-7.0 > NiO–NF-1.0 > NiO–NF-0.5. Interestingly, the abundance of Ni^{3+} in NiO-NFs also follows the same order, indicating that the activity in the NRR is influenced by the abundance of Ni^{3+}, enabling easier nitrogen adsorption compared to Ni^{2+}. These improved NRR performances are comparable to or even surpass those of reported catalysts containing noble metals, transition metal oxides, and NiO composite materials. Table 28 provides a summary of NRR performances for various recently reported catalysts, and the prepared NiO–NF-3.0 demonstrates comparable or superior performance to most of these catalysts.

6.1.3. Photocatalysts.

Synthetic dyes are widely used in the industry to dye fabrics, food, leather, plastics, and cosmetic products. It is estimated that 2–15% of the dye produced is eventually discharged into streams and rivers as wastewater.[220] Water pollution is a serious issue all over the world, especially in developing countries. To mitigate this problem, several researchers have recently synthesized photocatalysts with different types of nanomaterial structures to decompose organic pollutants in water bodies.

The photocatalytic activities of TiO_2 nanoflowers (TNF-T-t, $T =$ calcination temperature, $t =$ time of calcination) for the photo-oxidation of aqueous methylene blue under UV irradiation have been evaluated. The TNF-T-t (T = 400–800 °C, t = 1–5 h) photocatalysts show remarkable activity for the photo-oxidation at pH 6 under UV excitation (365 nm), with activities in the following order: TNF-700-1 > TNF-600-1 > TNF-500-1 > TNF-400-1∼P25 TiO_2 (the commercially available photocatalyst) TNF-800-1. Excessive rutile formation by prolonged calcination of the TNFs at 700 °C is detrimental to their dye-degradation performance, as it reduces the photocatalyst surface area and inhibits $OH^{\bullet}$ formation.[220] The MoS_2 nanoflowers exhibit almost 100% degradation of methylene blue and crystal violet under natural sun light.[415]

Three types of fluffy ZnO nanoflowers with different nanostructures: one with smooth edges (ZnO-0 generated *via* a hydrothermal process without ultrasonic treatment) and two with different jagged margins (ZnO-250 and ZnO-950 produced *via* ultrasonic treatment at 250 W and 950 W, respectively), have been evaluated as photocatalysts for the degradation of methyl orange. ZnO-0 exhibits the highest photocatalytic activity with a kinetic constant of 0.0478 min^{-1}.[324] The photocatalytic behavior of Bi_2Se_3 nanoflowers has been explored by degrading rhodamine B in the presence of H_2O_2, whereby the degradation rate of rhodamine B increases up to 93% after 2 h of visible-light irradiation.[43] The Ni-free rutile TiO_2 nanoflowers and Ni-doped rutile TiO_2 nanoflowers exhibit two and four times the photocatalytic activity of Degussa P25 TiO_2 powder, respectively, for the photodegradation of rhodamine B in water under Xe lamp illumination. This could be attributed to their higher specific surface areas (115 and 118 m^2 g^{-1} for Ni-free rutile TiO_2 nanoflowers and Ni-doped rutile TiO_2 nanoflowers, respectively) than Degussa P25 TiO_2 powder (50 m^2 g^{-1}), and Ni-doping that favors light harvesting and charge separation.[37]

Plasmonic Pd nanoflowers exhibit high photocatalytic activity for the Suzuki–Miyaura cross-coupling reactions under visible light irradiation.[156] Hierarchical flower-like TiO_2 superstructures show significantly higher photocatalytic activity than commercial Degussa P25 and tabular-shaped anatase TiO_2, due to a hierarchically porous structure, exposed {001} facets, and increased light harvesting ability.[218]

6.2. Sensors

Studies on the detection of industrially produced volatile organic compounds and toxic gases have attracted considerable attention because they cause environmental pollution, which seriously affects human safety. Semiconducting nanomaterials with large surface-area-to-volume ratios are potential candidates for gas-sensing applications.

A CuO nanoflower-based gas-sensing device has been reported to exhibit a very strong response for acetone vapor (250–2250 ppm concentration). The stability of the sensing device is maintained with a very small change (3.3% change in response) on repeating measurements for one month.[275] A hierarchical 3D TiO_2 nanoflower sensor exhibits high selectivity toward acetone at 60 °C with response magnitudes of 3.45% and 66.58% corresponding to response times of 33 s and 19 s and recovery times of 11 s and 37 s for 1 ppm and 700 ppm acetone, respectively.[92] Additionally, N-doped porous Mo_2C nanoflowers have been used to fabricate acetylcholinesterase biosensors for detecting organophosphorus pesticides.[386]

The NiO nanoflowers show excellent responses to NO_2 (among various gases, such as, H_2, NO_2, CO, toluene, NH_3, and H_2S) at 150 °C and 100 ppm due to the enhanced interaction between NO_2 and NiO owing to their mesoporous flower structure and large surface area.[379] The 530 nm-light-assisted Au@MoS_2 gas sensor utilizing the localized surface plasmon resonance (LSPR) effect of Au nanoparticles has been developed to detect NO_2 gas with a ppb-level detection limit and robust resistance to humidity interference.[61] By utilizing 530 nm light irradiation, the gas sensor can achieve a limit of detection as low as 10 ppb for NO_2, without requiring a specific operating temperature. Additionally, it demonstrates robust resistance to humidity, maintaining steady response values with only a slight drift of 6.5% across a wide range of humidity variations (10–90% relative humidity) because the illumination of light can decelerate the adsorption of H_2O molecules while facilitating the desorption of H_2O molecules.[414] The effective utilization of the LSPR enhances the absorption of visible light by MoS_2, leading to an increased surface carrier concentration. Table 29 provides a comparison of the gas-sensitive properties between the Au–MoS_2 gas sensor assisted by 530 nm light and other previously reported NO_2 sensors that utilize visible-light assistance. The prepared nanoflowers exhibit superior performance in terms of response value, detection limit, and recovery time when compared to other gas sensing materials.

6.3. Supercapacitors

The widespread applications of supercapacitors (also called electrochemical capacitors or ultracapacitors) in transportable electronics, uninterruptible power supplies, hybrid electric vehicles, and renewable energy sources have received significant attention from researchers owing to their high power densities, long cycle life, low cost, and fast charge–discharge rates compared to those of lithium-ion batteries and conventional capacitors.[422,423] Transition metal oxides with nanostructures exhibit immense potential as electrodes for supercapacitors because of their excellent pseudocapacitive behavior and relatively high electrical conductivity.[424–426]

Electrochemical tests of CuO nanoflowers fabricated on the surface of flexible Cu foil exhibit a high specific capacitance of 284.5 F g^{-1} at a current density of 0.5 mA cm^{-2} and high electrode cyclability (with a 20% loss in capacitance over 1000 cycles).[261] Among the three different morphologies of NiO nanomaterials (particle, honeycomb, and 3D nanoflower), NiO nanoflowers show the highest specific capacitance (364 F g^{-1} at 1 A g^{-1}), rate capability (64% capacitance retention from 1 A g^{-1} to 10 A g^{-1}), and cycling stability.[427] The Co_3O_4@$NiCo_2S_4$ core–shell nanoflower array show excellent electrochemical performance: 1234 F g^{-1} specific capacitance at a current density of 1 A g^{-1}, with a maximum energy density of 168 W h kg^{-1}, and approximately 11% loss of initial specific capacitance after 5000 cycles, owing to the unique configuration and strong synergistic effect of the porous Co_3O_4 core and the ultrathin $NiCo_2S_4$ shell.[381]

Nanoflower-like MCoP (M = Ni and Fe) composites on Ni foam, denoted as NF@MCoP, are synthesized through hydrothermal and low-temperature phosphating methods. NF@MCoP provides a larger electroactive area, shorter electron transfer distance, and faster electron conductivity due to its unique 3D structure, nanoflower morphology, and the conductive substrate, and exhibits enhanced electrochemical performance.[391] Optimization of the feeding molar ratio of M/Co, the amount of dimethyl sulfoxide (DMSO), and the hydrothermal time of Co precursors is carried out to improve the electrochemical capacitive performance of as-prepared NF@MCoP electrodes. The samples with a M/Co feeding molar ratio of 1 : 2 exhibits a higher specific capacitance compared to the other samples (1 : 1, 2 : 1, 1 : 1.5, and 1.5 : 1). The sample synthesized using 8 mL of DMSO demonstrates the highest specific capacitance, which aligns well with the cyclic voltammetry result. Extending the hydrothermal time to 6 hours results in a decrease in the electrochemical performance of nanoflower-like MCoP composites on Ni foam. The nanoflower-like composites show remarkable energy density, power density,

Table 29 Comparison of the gas-sensitive properties of visible-light-assisted NO_2 gas sensors. Reprinted with permission from ref. 61. Copyright © 2021, American Chemical Society. All rights reserved

Gas-sensing material	NO_2 (ppm)	Response value	Detection limit (ppb)	Recovery time	Excitation source	Ref.
ZnO–Ag nanoparticles	5	4.5	500	No	430 nm LED	415
CdS nanoflakes	5	89%	20	113 s	530 nm LED	416
WO_3	0.16	2.9	160	18.3 min	480 nm LED	417
CdSe quantum dots/ZnO	1	20	200	>60 min	535 nm LED	418
Au nanoparticles-ZnO nanorods	1	1.093	10 000	2500 s	495 nm LED	419
Black NiO	0.372	31.04%	57	No	480 nm LED	420
WO_3 nanofibers	0.4	1.49	160	>60 min	430 nm LED	421
Au–MoS_2 nanoflowers	1	8.1	10	27 s	530 nm LED	61

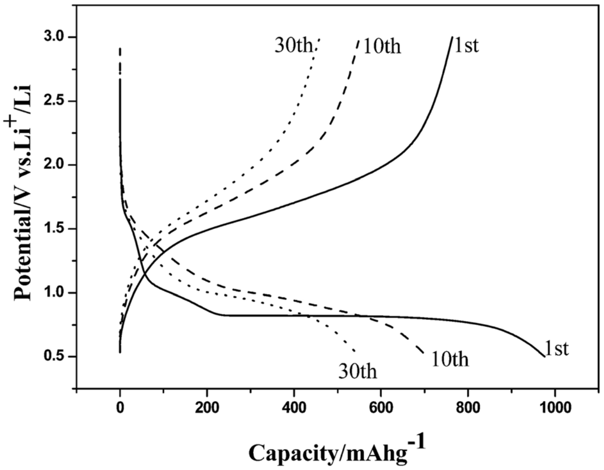

Fig. 19 The first (solid line), 10th (dashed line), and 30th (dotted line) charge–discharge curves of flower-like α-Fe_2O_3 nanostructures at a current density of 0.2 mA cm^{-2}. Reprinted with permission from ref. 306. Copyright © 2008, American Chemical Society. All rights reserved.

and long-term cycling stability. The area-specific capacitance values of NF@FeCoP and NF@NiCoP composites are measured to be 6.2 and 6.9 F cm^{-2}, respectively.

According to chronopotentiometry and cyclic voltammetry investigations, the hybrid battery–supercapacitor (HBS) devices display excellent capacitive performance, with 48.1 W h kg^{-1} at 2400 W kg^{-1} for NF@FeCoP and 33.3 W h kg^{-1} at 3746 W kg^{-1} for NF@NiCoP, along with high retention rates of 88% and 89% after 5000 cycles for NF@FeCoP and NF@NiCoP, respectively. The excellent performance of the NF@MCoP nanostructure can be attributed to several factors, including the highly reactive surface and short diffusion path provided by the nanoflower structure, the significant influence of DMSO on the morphology of NF@MCoP, and the low series resistance resulting from direct deposition on Ni foam.

6.4. Li-ion battery

Due to its high voltage, high capacity, long cycle life, and excellent safety performance,[428,429] the lithium-ion battery is an efficient energy storage device that has gained widespread use in portable electronics and is increasingly becoming the primary power source for electric vehicles.[280,430] To enhance the rate at which lithium ions intercalate and deintercalate in electrode materials, as well as to improve the capacity, cyclability, and safety, there has been significant focus on nano-sized electrode materials in recent years. Particularly, extensive research has been conducted on constructing 3D hierarchical nanostructures.[305,431–433] SnO nanoflowers have the potential to serve as effective anode materials in lithium-ion rechargeable batteries, exhibiting a high capacity of approximately 800 mA h g^{-1}, which is close to the theoretical value of 875 mA h g^{-1}.[305] In addition, the reversible capacities of metal oxide materials with 3D hierarchical nanostructures have been found to be significantly high when used as anode electrode materials in Li-ion batteries. This is primarily due to their large surface areas.[434,435] Hence, it is crucial to have precise control over the morphology during the preparation of the nanoflowers to ensure their effectiveness in applications related to lithium-ion rechargeable batteries.

Cao *et al.* studied the electrochemical properties of NiO electrodes in a lithium-ion battery. They found that the initial discharge capacity of the NiO nanoflowers is approximately 1300 mA h g^{-1}.[295]

The high surface area (71.9 m^2 g^{-1}) of the porous flower-like α-Fe_2O_3 nanostructures, as determined by the BET test, significantly enhances its performance in Li-ion battery applications.[306] Increasing the surface area or porosity of the hematite crystals improves the lithium intercalation performance.[306] In Fig. 19, the charge/discharge curves of the flower-like α-Fe_2O_3 nanostructures are compared for the first, tenth, and twentieth cycles. The initial discharge capacity is 974.43 mA h g^{-1}. Even after 10 and 30 cycles, the discharge capacities remain higher than that of graphite, with values of 705.5 and 548.47 mA h g^{-1},

Table 30 Summaries of the electrochemical properties of the NiO nanoflowers prepared in this work with other reported NiO nanostructures. Reprinted with permission from ref. 100. Copyright © 2016 Hydrogen Energy Publications LLC. Published by Elsevier Ltd. All rights reserved

Sample	Current density (mA g^{-1})	Potential range (V)	Initial capacity (mA h g^{-1})	Capacity retention (mA h g^{-1})	Ref.
NiO nanotubes	25	0.01–3.0	610	200 after 200 cycles	285
NiO microspheres	50	0.01–3.0	1570	80 after 30 cycles	437
Hollow NiO microspheres	100	0.02–3.0	1100	560 after 50 cycles	438
NiO nanospheres	100	0.01–3.0	1200	518 after 60 cycles	439
NiO–Ni nanocomposite	286	0.02–3	503	420 after 100 cycles	440
Three-dimensional porous NiO	200	0.05–3.0	800	520 after 30 cycles	441
Flower-like NiO microspheres	50	0.01–3.0	1104	105 after 30 cycles	442
Urchin-like NiO microspheres	50	0.01–3.0	1295	134 after 50 cycles	442
Electrospun NiO nanofibers	100	0.005–3.0	1280	583 after 100 cycles	443
Porous NiO nanoparticles	15	0.01–3.0	900	380 after 100 cycles	444
Hierarchical NiO nano/microspheres	100	0.01–3.0	1165	720 after 100 cycles	445
Hierarchical NiO microspheres	700	0.005–3.0	1452	598 after 100 cycles	446
Hollow NiO nanotubes	200	0.01–3.0	1072	600 after 100 cycles	447
NiO nanoflowers	100	0.01–3.0	1936.9	552 after 50 cycles	100

respectively. These flower-like nanostructures exhibit superior cycling performance compared to the previously reported α-Fe_2O_3 hollow spindles and microspheres (1313 and 1298 mA h g^{-1}) due to their higher surface area.[436]

Interestingly, the electrochemical properties of porous NiO nanoflowers are compared to those of similar NiO nanostructures (Table 30). The NiO nanoflower electrode demonstrates a favorable and consistent discharge capacity. Also, at a high current rate of 1C, the electrode exhibited an initial discharge capacity of 671.2 mA h g^{-1} and maintained a stable capacity of 306.8 mA h g^{-1} even after 80 cycles with a high coulombic efficiency of 98%. The produced NiO nanoflowers demonstrated promising outcomes as anode materials for Li-ion batteries, attributed to their high surface area and short diffusion length.[100]

7. Conclusion and future perspectives

Research related to flower-like hierarchical nanomaterials has developed considerably, with the exploration of synthetic technologies, growth mechanisms, particle size distributions, morphologies, chemical, physical, and optical properties to enhance catalytic, energy-related, and biomedical applications. Numerous types of inorganic-based nanoflowers have been synthesized through physical, chemical, biological, and hybrid methods: physical vapour deposition, solvothermal and hydrothermal processes, chemical vapour deposition, sol–gel, plant extract (green or bio synthesis), electrochemical deposition, galvanic displacement, microwave-assisted synthesis, high-energy ball-milling hydrothermal treatment, and the solution-immersion RF-sputtering method. In the last two decades, research related to flower-shaped hierarchical nanomaterials has progressed rapidly, and the number of related publications has gradually increased owing to their merits, such as high surface-to-volume ratio, strong adsorption capacity, high loading efficiency, and excellent catalytic activity.

Research on alloy and core–shell nanoflowers has particularly gained prominence, and flower-shaped nanostructure alloys and metal/metal oxide core–shell structures have been investigated for potential applications in the photo- and electrocatalysis of water splitting and fuel cells, owing to their composition and synergistic effects.

The modification of synthetic pathways, not by using surfactants, templates, or stabilizing agents, but rather by promoting reactions at lower temperatures and for shorter times has led to the development of simple, cost-effective, and eco-friendly synthetic routes for industrial-scale applications. Additionally, numerous studies have been conducted by controlling the reaction conditions (including the type and amount of reagents (precursors, reducing agents, surfactants, template agents), reaction time, temperature, and ratio of metals) to optimize the morphology and size distribution for specific applications. Numerous unique functionalities and potential applications have been reported.

Future research could focus on the development of uniform and monodisperse nanoflowers with high electrochemical, optical, and physical properties, suitable for various applications. Additionally, research on alloy, core–shell, and surface-treated nanoflowers is expected to expand multi-metallic compositions with modified structures. Furthermore, future studies on nanomaterials will potentially encompass the combination of multiple nanostructured materials, such as CoS nanoflowers wrapped in reduced graphene oxides,[448] nitrogen-doped graphene-encapsulated Ni–Cu alloy nanoflowers,[449] Pt nanoflower monolayers on single-walled carbon nanotube membranes,[450] and amorphous carbon nanotube–nickel oxide nanoflower hybrids.[451]

Author contributions

Conceptualization, H. J. and D. N. L.; methodology, S. J. L., H. J. and D. N. L.; validation, S. J. L. and H. J.; formal analysis, S. J. L.; investigation, S. J. L.; data curation, S. J. L. and D. N. L.; writing—original draft preparation, S. J. L.; writing—review and editing, H. J. and D. N. L.; supervision, D. N. L.; funding acquisition, S. J. L., H. J., and D. N. L. All authors have read and agreed to the published version of the manuscript.

Conflicts of interest

The authors declare no competing financial interest.

Acknowledgements

This research was supported by the Basic Science Research Program of the National Research Foundation of Korea (grants 2021R1A2C1004285 and 2019R1A2C2086770), by the Nano Material Technology Development Program through the NRF funded by the Ministry of Science, ICT, and Future Planning (2009-0082580), and by a Center for Women in Science, Engineering and Technology (WISET) grant funded by the Ministry of Science and ICT (MSIT) under the program for returners into R&D.

Notes and references

1 R. P. Feynman, *Eng. Sci.*, 1960, **23**, 22–36. **https://resolver.caltech.edu/CaltechES:23.5.1960Bottom**.
2 G. Binnig and H. Rohrer, *US Pat.*, US4343993A, 1982.
3 G. Binnig, H. Rohrer, C. Gerber and E. Weibel, *Appl. Phys. Lett.*, 1982, **40**, 178, DOI: **10.1063/1.92999**.
4 G. Binnig, H. Rohrer, C. Gerber and E. Weibel, *Phys. Rev. Lett.*, 1982, **49**, 57, DOI: **10.1103/PhysRevLett.49.57**.
5 G. Binnig, C. F. Quate and C. Gerber, *Phys. Rev. Lett.*, 1986, **56**, 930, DOI: **10.1103/PhysRevLett.56.930**.
6 G. Binnig, *US Pat.*, 4724318A, 1990.
7 X. Fan, N. Soin, H. Li, H. Li, X. Xia and J. Geng, *Energy Environ. Mater.*, 2020, **3**, 469–491, DOI: **10.1002/eem2.12071**.
8 M. Gaboardi, N. S. Amade, M. Aramini, C. Milanese, G. Magnani, S. Sanna, M. Ricco and D. Pontiroli, *Carbon*, 2017, **120**, 77–82, DOI: **10.1016/j.carbon.2017.05.025**.
9 T. Tang, T. Zhang, W. Li, X. Huang, X. Wang, H. Qiu and Y. Hou, *Nanoscale*, 2019, **11**, 7440–7446, DOI: **10.1039/C8NR09495K**.

10 G. Liu, W. Jin and N. Xu, *Chem. Soc. Rev.*, 2015, **44**, 5016–5030, DOI: 10.1039/C4CS00423J.
11 Y. Xiang, W. Zhu, W. Guo, F. Lou, B. Deng, D. Liu, Z. Xie, J. Li, D. Qu and H. Tang, *J. Alloys Compd.*, 2017, **719**, 347–352, DOI: 10.1016/j.jallcom.2017.05.217.
12 P. Nikolaev, M. J. Bronikowski, R. K. Bradley, F. Rohmund, D. T. Colbert, K. A. Smith and R. E. Smalley, *Chem. Phys. Lett.*, 1999, **313**, 91–97, DOI: 10.1016/S0009-2614(99)01029-5.
13 M. C. Wu, A. Sápi, A. Avila, M. Szabó, J. Hiltunen, M. Huuhtanen, G. Tóth, A. Kukovecz, Z. Kónya, R. Keiski, W. F. Su, H. Jantunen and K. Kordás, *Nano Res.*, 2011, **4**, 360–369, DOI: 10.1007/s12274-010-0090-9.
14 D. H. Nam, T. H. Kim, K. S. Hong and H. S. Kwon, *ACS Nano*, 2014, **8**(11), 11824–11835, DOI: 10.1021/nn505536t.
15 Y. Li and W. Shen, *Chem. Soc. Rev.*, 2014, **43**, 1543–1574, DOI: 10.1039/C3CS60296F.
16 C. Morita-Imura, T. Kobayashi, Y. Imura, T. Kawai and H. Shindo, *RSC Adv.*, 2015, **5**, 75889–75894, DOI: 10.1039/C5RA17369H.
17 R. Takahata, S. Yamazoe, K. Koyasu and T. Tsukuda, *J. Am. Chem. Soc.*, 2014, **136**, 8489–8491, DOI: 10.1021/ja503558c.
18 S. M. Alia, S. Shulda, C. Ngo, S. Pylypenko and B. S. Pivovar, *ACS Catal.*, 2018, **8**, 2111–2120, DOI: 10.1021/acscatal.7b03787.
19 R. Kumar, A. Kumar, N. Verma, V. Khopkar, R. Philip and B. Sahoo, *ACS Appl. Nano Mater.*, 2020, **3**, 8618–8631, DOI: 10.1021/acsanm.0c01284.
20 M. Hirasawa, T. Orii and T. Seto, *Appl. Phys. Lett.*, 2006, **88**, 093119, DOI: 10.1063/1.2182018.
21 K. Shoyama and F. Würthner, *J. Am. Chem. Soc.*, 2019, **141**, 13008–13012, DOI: 10.1021/jacs.9b06617.
22 R. Bhuvaneswari, V. Nagarajan and R. Chandiramouli, *J. Electron Spectrosc. Relat. Phenom.*, 2018, **227**, 15–22, DOI: 10.1016/j.elspec.2018.06.002.
23 B. Jiang, Y. Guo, J. Kim, A. E. Whitten, K. Wood, K. Kani, A. E. Rowan, J. Henzie and Y. Yamauchi, *J. Am. Chem. Soc.*, 2018, **140**, 12434–12441, DOI: 10.1021/jacs.8b05206.
24 Y. T. Tsai, S. J. Chang, I. T. Tang, Y. J. Hsiao and L. W. Ji, *IEEE Sens. J.*, 2018, **18**, 5559–5565, DOI: 10.1109/JSEN.2018.2830508.
25 S. Sharifi, S. Behzadi, S. Laurent, M. L. Forrest, P. Stroeve and M. Mahmoudi, *Chem. Soc. Rev.*, 2012, **41**, 2323–2343, DOI: 10.1039/c1cs15188f.
26 Y. Li, H. Wu and Z. Su, *Coord. Chem. Rev.*, 2020, **416**, 213342, DOI: 10.1016/j.ccr.2020.213342.
27 P. Shende, P. Kasture and R. S. Gaud, *Artif. Cells, Nanomed., Biotechnol.*, 2018, **46**(S1), 413–422, DOI: 10.1080/21691401.2018.1428812.
28 A. Guerrero-Martínez, S. Barbosa, I. Pastoriza-Santos and L. M. Liz-Marzán, *Curr. Opin. Colloid Interface Sci.*, 2011, **16**, 118–127, DOI: 10.1016/j.cocis.2010.12.007.
29 M. A. Mahmoud, R. Narayanan and M. A. El-Sayed, *Acc. Chem. Res.*, 2013, **46**, 1795–1805, DOI: 10.1021/ar3002359.
30 M. A. Mahmoud, B. Garlyyev and M. A. El-Sayed, *J. Phys. Chem. Lett.*, 2014, **5**, 4088–4094, DOI: 10.1021/jz502071v.
31 N. Soetan, H. F. Zarick, C. Banks, J. A. Webb, G. Libson, A. Coppola and R. Bardhan, *J. Phys. Chem. C*, 2016, **120**, 10320–10327, DOI: 10.1021/acs.jpcc.6b01238.
32 S. J. Lee, H. Jang and D. N. Lee, *Pharmaceutics*, 2022, **14**, 1887, DOI: 10.3390/pharmaceutics14091887.
33 Q. Liu, X. Guo, Y. Li and W. Shen, *J. Phys. Chem. C*, 2009, **113**, 3436–3441, DOI: 10.1021/jp8081744.
34 K. Seal, H. Chaudhuri, S. Basu, M. K. Mandal and S. Pal, *Arabian J. Sci. Eng.*, 2021, **46**, 6315–6331, DOI: 10.1007/s13369-020-04988-4.
35 F. Lv, W. Zhang, W. Yang, J. Feng, K. Wang, J. Zhou, P. Zhou and S. Guo, *Small Methods*, 2020, **4**, 1900129, DOI: 10.1002/smtd.201900129.
36 K. Gwon, J. D. Park, S. Lee, I. Han, J. S. Yu and D. N. Lee, *J. Ind. Eng. Chem.*, 2021, **99**, 264–270, DOI: 10.1016/j.jiec.2021.04.038.
37 L.-L. Lai, W. Wen and J.-M. Wu, *RSC Adv.*, 2016, **6**, 25511–25518, DOI: 10.1039/C6RA01752E.
38 Y. Imura, S. Koizumi, R. Akiyama, C. Morita-Imura and T. Kawai, *Langmuir*, 2017, **33**, 4313–4318, DOI: 10.1021/acs.langmuir.7b00974.
39 A. Moyano, E. Serrano-Pertierra, M. Salvador, J. C. Martínez-García, Y. Piñeiro, S. Yañez-Vilar, M. Gónzalez-Gómez, J. Rivas, M. Rivas and M. C. Blanco-López, *Biosensors*, 2020, **10**, 80, DOI: 10.3390/bios10080080.
40 S. Gnanasekar and A. N. Grace, *ACS Appl. Nano Mater.*, 2021, **4**, 8251–8261, DOI: 10.1021/acsanm.1c01447.
41 H. Liang, B. Guo, J. Huang, T. Feng, W. Wang, B. Dong and L. Cao, *ACS Appl. Nano Mater.*, 2019, **2**, 5245–5253, DOI: 10.1021/acsanm.9b01102.
42 K. Dai, X. Gao, L. Yin, Y. Feng, X. Zhou, Y. Zhao and B. Zhang, *Appl. Surf. Sci.*, 2019, **494**, 22–28, DOI: 10.1016/j.apsusc.2019.07.160.
43 D. Li, M. Fang, C. Jiang, H. Lin, C. Luo, R. Qi, R. Huang and H. Peng, *J. Nanopart. Res.*, 2018, **20**, 228, DOI: 10.1007/s11051-018-4342-z.
44 S. H. Lee, Y. J. Kim and J. Park, *Chem. Mater.*, 2007, **19**, 4670–4675, DOI: 10.1021/cm0711360.
45 J. B. Lee, S. Peng, D. Yang, Y. H. Roh, H. Funabashi, N. Park, E. J. Rice, L. Chen, R. Long, M. Wu and D. Luo, *Nat. Nanotechnol.*, 2012, **7**, 816–820, DOI: 10.1038/nnano.2012.211.
46 Y. Xiao, M. Zhang, F. X. Wang and G. B. Pan, *CrystEngComm*, 2012, **14**, 1933–1935, DOI: 10.1039/C2CE06401D.
47 S. Karan and B. Mallik, *J. Phys. Chem. C*, 2008, **112**, 2436–2447, DOI: 10.1021/jp709780a.
48 S. Chen, D. M. Koshy, Y. Tsao, R. Pfattner, X. Yan, D. Feng and Z. Bao, *J. Am. Chem. Soc.*, 2018, **140**(32), 10297–10304, DOI: 10.1021/jacs.8b05825.
49 Z. Xu, X. Zhuang, C. Yang, J. Cao, Z. Yao, Y. Tang, J. Jiang, D. Wu and X. Feng, *Adv. Mater.*, 2016, **28**, 1981–1987, DOI: 10.1002/adma.201505131.
50 Y. Zheng, S. Chen, K. A. I. Zhang, J. Zhu, J. Xu, C. Zhang and T. Liu, *ACS Appl. Mater. Interfaces*, 2021, **13**(11), 13328–13337, DOI: 10.1021/acsami.1c01348.

51 D. Shcharbin, I. Halets-Bui, V. Abashkin, V. Dzmitruk, S. Loznikova, M. Odabası, Ö. Acet, B. Önal, N. Özdemir, N. Shcharbina and M. Bryszewska, *Colloids Surf., B*, 2019, **182**, 110354, DOI: 10.1016/j.colsurfb.2019.110354.

52 S. W. Lee, S. A. Cheon, M. I. Kim and T. J. Park, *J. Nanobiotechnol.*, 2015, **13**, 54, DOI: 10.1186/s12951-015-0118-0.

53 J. Cui and S. Jia, *Coord. Chem. Rev.*, 2017, **352**, 249–263, DOI: 10.1016/j.ccr.2017.09.008.

54 D. Shcharbin, I. Halets-Bui, V. Abashkin, V. Dzmitruk, S. Loznikova, M. Odabaşı, Ö. Acet, B. Önal, N. Özdemir, N. Shcharbina and M. Bryszewska, *Colloids Surf., B*, 2019, **182**, 110354, DOI: 10.1016/j.colsurfb.2019.110354.

55 K. H. Kim, J.-M. Jeong, S. J. Lee, B. G. Choi and K. G. Lee, *J. Colloid Interface Sci.*, 2016, **484**, 44–50, DOI: 10.1016/j.jcis.2016.08.059.

56 Z.-F. Wu, Z. Wang, Y. Zhang, Y.-L. Ma, C.-Y. He, H. Li, L. Chen, Q.-S. Huo, L. Wang and Z.-Q. Li, *Sci. Rep.*, 2016, **6**, 22412, DOI: 10.1038/srep22412.

57 W. T. Yao, S. H. Yu, S. J. Liu, J. P. Chen, X. M. Liu and F. Q. Li, *J. Phys. Chem. B*, 2006, **110**(24), 11704–11710, DOI: 10.1021/jp060164n.

58 Y. Qu, M. Shao, Y. Shao, M. Yang, J. Xu, C. T. Kwok, X. Shi, Z. Lu and H. Pan, *J. Mater. Chem. A*, 2017, **5**, 15080–15086, DOI: 10.1039/C7TA03172F.

59 T. P. Nguyen and I. T. Kim, *Nanomaterials*, 2020, **10**, 1336, DOI: 10.3390/nano10071336.

60 T. Tao, A. M. Glushenkov, H. Liu, Z. Liu, X. J. Dai, H. Chen, S. P. Ringer and Y. Chen, *J. Phys. Chem. C*, 2011, **115**, 17297–17302, DOI: 10.1021/jp203345s.

61 P. Chen, J. Hu, M. Yin, W. Bai, X. Chen and Y. Zhang, *ACS Appl. Nano Mater.*, 2021, **4**, 5981–5991, DOI: 10.1021/acsanm.1c00847.

62 M. Y. A. Rahman, A. A. Umar, L. Roza and A. A. Salleh, *J. Exp. Nanosci.*, 2015, **10**, 925–936, DOI: 10.1080/17458080.2014.933494.

63 Y. Jiang, X.-J. Wu, Q. Li, J. Li and D. Xu, *Nanotechnology*, 2011, **22**, 385601, DOI: 10.1088/0957-4484/22/38/385601.

64 L. Lu, K. Ai and Y. Ozaki, *Langmuir*, 2008, **24**, 1058–1063, DOI: 10.1021/acssuschemeng.7b03425.

65 L. Storozhuk, M. O. Besenhard, S. Mourdikoudis, A. P. LaGrow, M. R. Lees, L. D. Tung, A. Gavriilidis and N. T. K. Thanh, *ACS Appl. Mater. Interfaces*, 2021, **13**, 45870–45880, DOI: 10.1021/acsami.1c12323.

66 A. Narayanaswamy, H. Xu, N. Pradhan, M. Kim and X. Peng, *J. Am. Chem. Soc.*, 2006, **128**, 10310–10319, DOI: 10.1021/ja0627601.

67 S. K. Kulkarni, *Nanotechnology: Principles and Practices*, Springer, Berlin/Heidelberg, Germany, 2015, pp. 55–133, DOI: 10.1007/978-3-319-09171-6.

68 X. Yu and C. Cao, *Cryst. Growth Des.*, 2008, **8**, 3951–3955, DOI: 10.1021/cg701001m.

69 S. B. Wategaonkar, R. P. Pawar, V. G. Parale, K. S. Pakhare, B. M. Sargar and R. K. Mane, *Macromol. Symp.*, 2020, **393**, 2000040, DOI: 10.1002/masy.202000040.

70 J. N. Zheng, L. L. He, C. Chen, A. J. Wang, K. F. Ma and J. J. Feng, *J. Power Sources*, 2014, **268**, 744–751, DOI: 10.1016/j.jpowsour.2014.06.109.

71 O. E. Meiron, V. Kuraganti, I. Hod, R. Bar-Ziv and M. Bar-Sadan, *Nanoscale*, 2017, **9**, 13998–14005, DOI: 10.1039/C7NR04922F.

72 A. Nagar, A. Kumar, S. Parveen, A. Kumar, H. Dhasmana, S. Husain, A. Verma and V. K. Jain, *Mater. Today*, 2020, **32**, 402–406, DOI: 10.1016/j.matpr.2020.02.087.

73 A. Y. Faid and H. Ismail, *ChemistrySelect*, 2019, **4**, 7896–7903, DOI: 10.1002/slct.201901580.

74 X. Gao, Y. Li, W. Zeng, C. Zhang and Y. Wei, *J. Mater. Sci.: Mater. Electron.*, 2017, **28**, 18781–18786, DOI: 10.1007/s10854-017-7827-0.

75 B. Zhang, H. Peng, L. Yang, H. Li, H. Nan, Z. Liang, H. Song, H. Su, C. Li and S. Liao, *J. Mater. Chem. A*, 2015, **3**, 973–977, DOI: 10.1039/C4TA04989F.

76 G. A. Molina, R. Esparza, J. L. Lopez-Miranda, A. R. Hernandez-Martinez, B. L. Espana-Sanchez, E. A. Elizalde-Pena and M. Estevez, *Colloids Surf., B*, 2019, **180**, 141–149, DOI: 10.1016/j.colsurfb.2019.04.044.

77 S. Andra, R. Ramoorthy and M. Muthalagu, *Res. Express*, 2018, **5**, 065043, DOI: 10.1088/2053-1591/aabb61.

78 H. Siddiqui, M. S. Qureshi and F. Z. Haque, *Nano-Micro Lett.*, 2020, **12**, 29, DOI: 10.1007/s40820-019-0357-y.

79 R. Biswas, B. Banerjee, M. Saha, I. Ahmed, S. Mete, R. A. Patil, Y. R. Ma and K. K. Haldar, *J. Phys. Chem. C*, 2021, **125**(12), 6619–6631, DOI: 10.1021/acs.jpcc.0c10149.

80 N. Masurkar, N. K. Thangavel and L. M. R. Arava, *ACS Appl. Mater. Interfaces*, 2018, **10**, 27771–27779, DOI: 10.1021/acsami.8b07489.

81 N. Arjona, M. Guerra-Balcazar, F. M. Cuevaz-Muniz, L. Alvarez-Contreras, J. Ledesma-Garcia and L. G. Arriaga, *RSC Adv.*, 2013, **3**, 15727–15733, DOI: 10.1039/C3RA41681J.

82 W. Zhao, N. Du, H. Zhang and D. Yang, *J. Power Sources*, 2015, **285**, 131–136, DOI: 10.1016/j.jpowsour.2015.03.088.

83 L. Kumari, J. H. Lin and Y. R. Ma, *Nanotechnology*, 2007, **18**, 295605, DOI: 10.1088/0957-4484/18/29/295605.

84 J.-H. Lee, *Sens. Actuators, B*, 2009, **140**(1), 319–336, DOI: 10.1016/j.snb.2009.04.026.

85 Y. Ni, Z. Sun, Z. Zeng, F. Liu and J. Qin, *New J. Chem.*, 2019, **43**, 18629, DOI: 10.1039/C9NJ04236A.

86 M. A. Khan, N. Nayan, M. K. S. Ahmad, S. C. Fhong, M. Tahir, R. A. Mohamed Ali and M. S. Mohamed Ali, *Molecules*, 2021, **26**, 2700, DOI: 10.3390/molecules26092700.

87 Y. Qu, R. Huang, W. Qi, M. Shi, R. Su and Z. He, *Catal. Today*, 2020, **355**, 397–407, DOI: 10.1016/j.cattod.2019.07.056.

88 S. Sun, S. Feng, M. Terrones and R. E. Schaak, *Chem. Mater.*, 2015, **27**, 3167–3175, DOI: 10.1021/acs.chemmater.5b01129.

89 K. Vasu, O. E. Meiron, A. N. Enyashin, R. Bar-Ziv and M. Bar-Sadan, *J. Phys. Chem. C*, 2019, **123**, 1987–1994, DOI: 10.1021/acs.jpcc.8b11712.

90 O. Zimron, T. Zilberman, S. R. Kadam, S. Ghosh, S. L. Kolatker, A. Neyman, R. Bar-Ziv and M. Bar-Sadan, *Isr. J. Chem.*, 2020, **60**, 624, DOI: 10.1002/ijch.201900162.

91 D. Li, J. Lao, C. Jiang, C. Luo, R. Qi, H. Lin, R. Huang, G. I. N. Waterhouse and H. Peng, *Int. J. Hydrogen Energy*, 2019, **44**, 30876–30884, DOI: 10.1016/j.ijhydene.2019.10.041.

92 B. Bhowmik, V. Manjuladevi, R. K. Gupta and P. Bhattacharyya, *IEEE Sens. J.*, 2016, **16**, 3488–3495, DOI: 10.1109/JSEN.2016.2530827.

93 B. Zhao, F. Chen, Q. Huang and J. Zhang, *Chem. Commun.*, 2009, 5115–5117, DOI: 10.1039/B909883F.

94 Y. Xu, J. Jin, X. Li, Y. Han, H. Meng, T. Wang and X. Zhang, *Mater. Res. Bull.*, 2016, **76**, 235–239, DOI: 10.1016/j.materresbull.2015.11.062.

95 W. Guo, X. Li, H. Qin and Z. Wang, *Phys. E*, 2015, **73**, 163–168, DOI: 10.1016/j.physe.2015.05.006.

96 G. Bai, H. Dai, J. Deng, Y. Liu and K. Ji, *Catal. Commun.*, 2012, **27**, 148–153, DOI: 10.1016/j.catcom.2012.07.008.

97 R. Miao, W. Zeng and Q. Gao, *Mater. Lett.*, 2017, **186**, 175–177, DOI: 10.1016/j.matlet.2016.09.127.

98 A. Gu, G. Wang, X. Zhang and B. Fang, *Bull. Mater. Sci.*, 2010, **33**, 17–20, DOI: 10.1007/s12034-010-0002-3.

99 Z. Li, J. Wang, N. Wang, S. Yan, W. Liu, Y. Q. Fu and Z. Wang, *J. Alloys Compd.*, 2017, **725**, 1136–1143, DOI: 10.1016/j.jallcom.2017.07.218.

100 Y. B. Mollamahale, Z. Liu, Y. Zhen, Z. Q. Tian, D. Hosseini, L. Chen and P. K. Shen, *Int. J. Hydrogen Energy*, 2017, **42**, 7202–7211, DOI: 10.1016/j.ijhydene.2016.05.193.

101 P. Wang, Y. Gao, P. Li, X. Zhang, H. Niu and Z. Zheng, *ACS Appl. Mater. Interfaces*, 2016, **8**, 15820–15827, DOI: 10.1021/acsami.6b04378.

102 M. Zhong, X. Meng, F. Wu, J. Li and Y. Fang, *Nanoscale Res. Lett.*, 2013, **8**, 451, DOI: 10.1186/1556-276X-8-451.

103 H. Guan, X. Zhang and Y. Xie, *J. Phys. Chem. C*, 2014, **118**, 27170–27174, DOI: 10.1021/jp509045d.

104 I. Bilecka and M. Niederberger, *Nanoscale*, 2010, **2**, 1358–1374, DOI: 10.1039/B9NR00377K.

105 G. A. Babu, G. Ravi, M. Navaneethan, M. Arivanandhan and Y. Hayakawa, *J. Mater. Sci.: Mater. Electron.*, 2014, **25**, 5231–5240, DOI: 10.1007/s10854-014-2293-4.

106 Y. Ren and L. Gao, *J. Am. Ceram. Soc.*, 2010, **93**, 3560–3564, DOI: 10.1111/j.1551-2916.2010.04090.x.

107 V. Makarov, A. Love, O. Sinitsyna, S. Makarova, I. Yaminsky, M. Taliansky and N. Kalinina, *Acta Naturae*, 2014, **6**, 35–44.

108 M. Hasana, M. Altaf, A. Zafar, S. G. Hassan, Z. Ali, G. Mustafa, T. Munawar, M. S. Saif, T. Tariq, F. Iqbal, M. Q. Khan, A. Mahmood, N. Mahmood and X. Shu, *Mater. Sci. Eng., C*, 2021, **119**, 111280, DOI: 10.1016/j.msec.2020.111280.

109 H. Zhang, W. Zhou, Y. Du, P. Yang and C. Wang, *Electrochem. Commun.*, 2010, **12**, 882–885, DOI: 10.1016/j.elecom.2010.04.011.

110 M. Q. Guo, H. S. Hong, X. N. Tang, H. D. Fang and X. H. Xu, *Electrochim. Acta*, 2012, **63**, 1–8, DOI: 10.1016/j.electacta.2011.11.114.

111 J. N. Tiwari, F. M. Pan and K. L. Lin, *New J. Chem.*, 2009, **33**, 1482–1485, DOI: 10.1039/B901534P.

112 Y. Zuo, L. Wu, K. Cai, T. Li, W. Yin, D. Li, N. Li, J. Liu and H. Han, *ACS Appl. Mater. Interfaces*, 2015, **7**, 17725–17730, DOI: 10.1021/acsami.5b03826.

113 J. Bi, *Mater. Lett.*, 2019, **236**, 398–402, DOI: 10.1016/j.matlet.2018.10.138.

114 L. I. Sun, L. L. Liu, L. H. Luo, Y. F. Wu, J. J. Shi, L. Cheng, X. Xu and Y. M. Guo, *J. Fuel Chem. Technol.*, 2016, **44**, 607–612, DOI: 10.1016/S1872-5813(16)30027-5.

115 L. Qian and X. Yang, *J. Phys. Chem. B*, 2006, **110**, 16672–16678, DOI: 10.1021/jp063302h.

116 H. Xu, B. Yan, K. Zhang, J. Wang, S. Li, C. Wang, Z. Xiong, Y. Shiraishi, Y. Du and P. Yang, *ACS Sustainable Chem. Eng.*, 2017, **5**, 10490–10498, DOI: 10.1021/acssuschemeng.7b02491.

117 D. Alby, F. Salles, A. Geneste, B. Prélot, J. Zajac and C. Charnay, *J. Hazard. Mater.*, 2019, **368**, 661–669, DOI: 10.1016/j.jhazmat.2019.01.064.

118 H. Zhang, W. G. Chen, Y. Q. Li, L. F. Jin, F. Cui and Z. H. Song, *Front. Chem.*, 2018, **6**, 472, DOI: 10.3389/fchem.2018.00472.

119 S. Borbón, S. Lugo and I. López, *Mater. Sci. Semicond.*, 2019, **91**, 310–315, DOI: 10.1016/j.mssp.2018.12.001.

120 H. Yang, S. Liao, C. Huang, L. Du, P. Chen, P. Huang, Z. Fu and Y. Li, *Appl. Surf. Sci.*, 2014, **314**, 7–14, DOI: 10.1016/j.apsusc.2014.06.128.

121 M. A. C., F. K. P., S. Singh and S. Baik, *Sci. Rep.*, 2016, **6**, 34894, DOI: 10.1038/srep34894.

122 C. Yang, X. Cui, Z. Zhang, S. W. Chiang, W. Lin, H. Duan, J. Li, F. Kang and C.-P. Wong, *Nat. Commun.*, 2015, **6**, 8150, DOI: 10.1038/ncomms9150.

123 R. Ma, B. Kang, S. Cho, M. Choi and S. Baik, *ACS Nano*, 2015, **9**, 10876–10886, DOI: 10.1021/acsnano.5b03864.

124 B. Zhang, P. Xu, X. Xie, H. Wei, Z. Li, N. H. Mack, X. Han, H. Xu and H. L. Wang, *J. Mater. Chem.*, 2011, **21**, 2495–2501, DOI: 10.1039/C0JM02837A.

125 H. Xu, B. Yan, K. Zhang, J. Wang, S. Li, C. Wang, Z. Xiong, Y. Shiraishi and Y. Du, *ChemElectroChem*, 2017, **4**, 2527–2534, DOI: 10.1002/celc.201700611.

126 S. Das, A. Samanta and S. Jana, *Chem. Eng. J.*, 2019, **374**, 1118–1126, DOI: 10.1016/j.cej.2019.05.114.

127 S. Cao, T. Han and L. Peng, *J. Mater. Sci.: Mater. Electron.*, 2020, **31**, 17291–17296, DOI: 10.1007/s10854-020-04283-w.

128 K. M. AbouZeid, M. B. Mohamed and M. S. El-Shall, *Small*, 2011, **7**, 3299–3307, DOI: 10.1002/smll.201100688.

129 N. H. Hung, N. D. Thanh, N. H. Lam, N. D. Dien, N. D. Chien and D. D. Vuong, *Mater. Sci. Semicond. Process.*, 2014, **26**, 18–24, DOI: 10.1016/j.mssp.2014.03.052.

130 S. Ye, F. Benz, M. C. Wheeler, J. Oram, J. J. Baumberg, O. Cespedes, H. K. Christenson, P. L. Coletta, L. J. C. Jeuken, A. F. Markham, K. Critchley and S. D. Evans, *Nanoscale*, 2016, **8**, 14932–14942, DOI: 10.1039/C6NR04045D.

131 J. Xie, Q. Zhang, J. Y. Lee and D. I. C. Wang, *ACS Nano*, 2008, **2**, 2473–2480, DOI: 10.1021/nn800442q.

132 C. Y. Song, B. Y. Yang, W. Q. Chen, Y. X. Dou, Y. J. Yang, N. Zhou and L. H. Wang, *J. Mater. Chem. B*, 2016, **4**, 7112–7118, DOI: **10.1039/C6TB01046F**.

133 B. K. Jena and C. R. Raj, *Langmuir*, 2007, **23**, 4064–4070, DOI: **10.1021/la063243z**.

134 B. K. Jena and C. R. Raj, *Chem. Mater.*, 2008, **20**, 3546–3548, DOI: **10.1021/cm7019608**.

135 S. Li, L. Zhang, T. Wang, L. Li, C. Wang and Z. Su, *Chem. Commun.*, 2015, **51**, 14338–14341, DOI: **10.1039/C5CC05676D**.

136 H. Ma, Z. Liu, Y. Wei and L. Jiang, *Colloids Surf., A*, 2019, **582**, 123889, DOI: **10.1016/j.colsurfa.2019.123889**.

137 L. Zhong, X. Zhai, X. Zhu, P. Yao and M. Liu, *Langmuir*, 2010, **26**, 5876–5881, DOI: **10.1021/la903809k**.

138 C. Y. Song, N. Zhou, B. Y. Yang, Y. J. Yang and L. H. Wang, *Nanoscale*, 2015, **7**, 17004–17011, DOI: **10.1039/C5NR04827C**.

139 K. Mao, Y. Chen, Z. Wu, X. Zhou, A. Shen and J. Hu, *J. Agric. Food Chem.*, 2014, **62**, 10638–10645, DOI: **10.1021/jf5034015**.

140 A. J. Wang, Y. F. Li, M. Wen, G. Yang and H. Y. Wang, *New J. Chem.*, 2012, **36**, 2286–2291, DOI: **10.1039/C2NJ40380C**.

141 Y. Wang, N. Shah and G. P. Huffman, *Energy Fuels*, 2004, **18**, 1429–1433, DOI: **10.1021/ef049959o**.

142 A. Fukuoka, J. Kimura, T. Oshio, Y. Sakamoto and M. Ichikawa, *J. Am. Chem. Soc.*, 2007, **129**, 10120–10125, DOI: **10.1021/ja0703123**.

143 S. H. Joo, J. Y. Park, C. K. Tsung, Y. Yamada, P. D. Yang and G. A. Somorjai, *Nat. Mater.*, 2009, **8**, 126–131, DOI: **10.1038/nmat2329**.

144 J. H. Yuan, K. Wang and X. H. Xia, *Adv. Funct. Mater.*, 2005, **15**, 803–809, DOI: **10.1002/adfm.200400321**.

145 J. Chen, B. Lim, E. P. Lee and Y. Xia, *Nano Today*, 2009, **4**, 81–95, DOI: **10.1016/j.nantod.2008.09.002**.

146 G. A. Somorjai, *Chemistry in Two Dimensions: Surfaces*, Cornell University Press, Ithaca, NY, 1981.

147 C. Wang, H. Daimon, T. Onodera, T. Koda and S. A. Sun, *Angew. Chem., Int. Ed. Engl.*, 2008, **47**, 3588–3591, DOI: **10.1002/anie.200800073**.

148 K. M. Bratlie, H. Lee, K. Komvopoulos, P. Yang and G. A. Somorjai, *Nano Lett.*, 2007, **7**, 3097–3101, DOI: **10.1021/nl0716000**.

149 N. V. Long, C. M. Thi, M. Nogami and M. Ohtaki, *New J. Chem.*, 2012, **36**, 1320–1334, DOI: **10.1039/C2NJ40027H**.

150 J. Zhang, H. Yang, J. Fang and S. Zou, *Nano Lett.*, 2010, **10**, 638–644, DOI: **10.1021/nl903717z**.

151 Z. W. Chen, M. Waje, W. Z. Li and Y. S. Yan, *Angew. Chem., Int. Ed. Engl.*, 2007, **46**, 4060–4063, DOI: **10.1002/anie.200700894**.

152 S. H. Sun, F. Jaouen and J. P. Dodelet, *Adv. Mater.*, 2008, **20**, 3900–3904, DOI: **10.1002/adma.200800491**.

153 A. Dandapat, A. Mitra, P. K. Gautam and G. A. De, *Nanomater. Nanotechnol.*, 2013, **3**, 11, DOI: **10.5772/56868**.

154 P. Dhanasekaran, K. Lokesh, P. K. Ojha, A. K. Sahu, S. D. Bhat and D. Kalpana, *J. Colloid Interface Sci.*, 2020, **572**, 198–206, DOI: **10.1016/j.jcis.2020.03.078**.

155 H. Kawasaki, T. Yonezawa, T. Watanabe and R. Arakawa, *J. Phys. Chem. C*, 2007, **111**, 16278–16283, DOI: **10.1021/jp075159d**.

156 M. Wang, X. Wang, J. Li and L. Liu, *J. Mater. Chem. A*, 2013, **1**, 8127, DOI: **10.1039/c3ta11997a**.

157 H. Heli, N. Sattarahmady, R. D. Vais and A. R. Mehdizadeh, *Sens. Actuators, B*, 2014, **192**, 310–316, DOI: **10.1016/j.snb.2013.10.124**.

158 R. Ojani, E. Hasheminejad and J. B. Raoof, *Energy*, 2015, **90**, 1122–1131, DOI: **10.1016/j.energy.2015.06.061**.

159 H. M. Ngo, N. D. Lai and I. Ledoux-Rak, *Nanoscale*, 2016, **8**, 3489–3495, DOI: **10.1039/C5NR07571H**.

160 T. L. Nguyen, V. H. Cao, T. H. Y. Pham and T. G. Le, *J. Chem.*, 2019, **2019**, 6235479, DOI: **10.1155/2019/6235479**.

161 E. Antolini, *Energy Environ. Sci.*, 2009, **2**, 915–931, DOI: **10.1039/B820837A**.

162 A. R. Siamaki, A. E. R. S. Khder, V. Abdelsayed, M. S. El-Shall and B. F. Gupton, *J. Catal.*, 2011, **279**, 1–11, DOI: **10.1016/j.jcat.2010.12.003**.

163 X. Q. Huang and N. F. Zheng, *J. Am. Chem. Soc.*, 2009, **131**, 4602–4603, DOI: **10.1021/ja9009343**.

164 H. Bai, M. Han, Y. Du, J. Bao and Z. Dai, *Chem. Commun.*, 2010, **46**, 1739–1741, DOI: **10.1039/B921004K**.

165 X. Huang, S. Tang, X. Mu, Y. Dai, G. Chen, Z. Zhou, F. Ruan, Z. Yang and N. Zheng, *Nat. Nanotechnol.*, 2011, **6**, 28–32, DOI: **10.1038/nnano.2010.235**.

166 S. Guo and E. Wang, *Nano Today*, 2011, **6**, 240–264, DOI: **10.1016/j.nantod.2011.04.007**.

167 Y. Xia, Y. Xiong, B. Lim and S. E. Skrabalak, *Angew. Chem., Int. Ed. Engl.*, 2008, **48**, 60–103, DOI: **10.1002/anie.200802248**.

168 X. Lu, M. Rycenga, S. E. Skrabalak, B. Wiley and Y. Xia, *Annu. Rev. Phys. Chem.*, 2009, **60**, 167–192, DOI: **10.1146/annurev.physchem.040808.090434**.

169 H. Zhang, M. Jin, Y. Xiong, B. Lim and Y. Xia, *Acc. Chem. Res.*, 2013, **46**, 1783–1794, DOI: **10.1021/ar300209w**.

170 A. Wang, F. F. Li, J. N. Zheng, H. X. Xi, Z. Y. Meng and J. J. Feng, *RSC Adv.*, 2013, **3**, 10355–10362, DOI: **10.1039/C3RA40556G**.

171 N. Ma, X. Liu, Z. Yang, G. Tai, Y. Yin, S. Liu, H. Li, P. Guo and X. S. Zhao, *ACS Sustainable Chem. Eng.*, 2018, **6**, 1133–1140, DOI: **10.1021/acssuschemeng.7b03425**.

172 K. K. Maniam and R. Chetty, *Fuel Cells*, 2013, **13**, 1196–1204, DOI: **10.1002/fuce.201200162**.

173 W. Guo, G. S. Luo and Y. J. Wang, *J. Colloid Interface Sci.*, 2004, **271**, 400–406, DOI: **10.1016/j.jcis.2003.08.056**.

174 K. Qi, Q. Y. Wang, W. T. Zheng, W. Zhang and X. Q. Cui, *Nanoscale*, 2014, **6**, 15090–15097, DOI: **10.1039/C4NR05761A**.

175 Z. Yin, H. Zheng, D. Ma and X. Bao, *J. Phys. Chem. C*, 2009, **113**, 1001–1005, DOI: **10.1021/jp807456j**.

176 I. Sarhid, I. Abdellah, C. Martini, V. Huc, D. Dragoe, P. Beaunier, I. Lampre and H. Remita, *New J. Chem.*, 2019, **43**, 4349–4355, DOI: **10.1039/C8NJ06370B**.

177 M. del C. Aguirre, *J. Appl. Electrochem.*, 2019, **49**, 795–809, DOI: **10.1007/s10800-019-01323-0**.

178 R. Jin, Y. C. Cao, E. Hao, G. S. Metraux, G. C. Schatz and C. A. Mirkin, *Nature*, 2003, **425**, 487–490, DOI: **10.1038/nature02020**.

179 C. Yang, X. Ciu, Z. Zhang, S. W. Chiang, W. Lin, H. Duan, J. Li, F. Kang and C. P. Wong, *Nat. Commun.*, 2015, **6**, 8150, DOI: **10.1038/ncomms9150**.

180 B. Wiley, Y. Sun and Y. Xia, *Acc. Chem. Res.*, 2007, **40**, 1067–1076, DOI: **10.1021/ar7000974**.

181 L. Zhang, Y. Zhao, Z. Lin, F. Gu, S. P. Lau, L. Li and Y. Chai, *Nanoscale*, 2015, **7**, 13420–13426, DOI: **10.1039/C5NR02611C**.

182 X. Liu, Z. Liu, S. Hao and W. Chu, *Mater. Lett.*, 2012, **80**, 66–68, DOI: **10.1016/j.matlet.2012.04.031**.

183 P. J. Rivero, A. Urrutia, J. Goicoechea, Y. Rodríguez, J. M. Corres, F. J. Arregui and I. R. Matías, *J. Appl. Polym. Sci.*, 2012, **126**, 1228–1235, DOI: **10.1002/app.36886**.

184 J. Li, D. Zhang, J. B. Guo and J. Wei, *Chin. J. Chem. Phys.*, 2014, **27**, 718–724, DOI: **10.1063/1674-0068/27/06/718-724**.

185 L. M. Chen and Y. N. Liu, *J. Raman Spectrosc.*, 2012, **43**, 986–991, DOI: **10.1002/jrs.3137**.

186 P. Manivasagan, J. Venkatesan, K. Sivakumar and S. K. Kim, *Crit. Rev. Microbiol.*, 2016, **42**, 209–221, DOI: **10.3109/1040841X.2014.917069**.

187 S. Preciado-Flores, D. A. Wheeler, T. M. Tran, Z. Tanaka, C. Jiang, M. Barboza-Flores, F. Qian, Y. Li, B. Chen and J. Z. Zhang, *Chem. Commun.*, 2011, **47**, 4129–4131, DOI: **10.1039/C0CC05517D**.

188 T. Jiang, B. Wang, L. Zhang and J. Zhou, *J. Alloys Compd.*, 2015, **632**, 140–146, DOI: **10.1016/j.jallcom.2015.01.164**.

189 M. S. Bootharaju, V. M. Burlakov, T. M. Besong, C. P. Joshi, L. G. AbdulHalim, D. M. Black, R. L. Whetten, A. Goriely and O. M. Bakr, *Chem. Mater.*, 2015, **27**, 4289–4297, DOI: **10.1021/acs.chemmater.5b00650**.

190 H. Zheng, D. Ni, Z. Yu, P. Liang and H. Chen, *Sens. Actuators, B*, 2016, **231**, 423–430, DOI: **10.1016/j.snb.2016.03.045**.

191 C. R. Rekha, V. U. Nayar and K. G. Gopchandran, *J. Sci.: Adv. Mater. Devices*, 2018, **3**(2), 196–205, DOI: **10.1016/j.jsamd.2018.03.003**.

192 D. Wu, M. Hu, Y. Zhang, J. Zhou and Z. Wang, *Appl. Surf. Sci.*, 2020, **505**, 144520, DOI: **10.1016/j.apsusc.2019.144520**.

193 H. B. Eral, D. J. C. M. 't Mannetje and J. M. Oh, *Colloid Polym. Sci.*, 2013, **291**, 247–260, DOI: **10.1007/s00396-012-2796-6**.

194 Z. Yang, T. C. Chiu and H. T. Chang, *Open Nanosci. J.*, 2007, **1**, 5–12, DOI: **10.2174/1874140100701010005**.

195 B. K. Jena, B. K. Mishra and S. Bohidar, *J. Phys. Chem. C*, 2009, **113**, 14753–14758, DOI: **10.1021/jp904689f**.

196 J. Bian, Z. Li, Z. Chen, X. Zhang, Q. Li, S. Jiang, J. He and G. Han, *Electrochim. Acta*, 2012, **67**, 12–17, DOI: **10.1016/j.electacta.2012.01.073**.

197 L. Wu, W. Wu, X. Jing, J. Huang, D. Sun, T. Odoom-Wubah, H. Liu, H. Wang and Q. Li, *Ind. Eng. Chem. Res.*, 2013, **52**, 5085–5094, DOI: **10.1021/ie303518z**.

198 Q. Chang, X. Shi, X. Liu, J. Tong, D. Liu and Z. Wang, *Nanophotonics*, 2017, **6**, 1151–1160, DOI: **10.1515/nanoph-2017-0010**.

199 Y. H. Chang, C. Liu, S. Rouvimov, T. Luo and S. P. Feng, *Chem. Commun.*, 2017, **53**, 6752–6755, DOI: **10.1039/C7CC02738A**.

200 Y. Tian, H. Liu, Y. Chen, C. Zhou, Y. Jiang, C. Gu, T. Jiang and J. Zhou, *Sens. Actuators, B*, 2019, **301**, 127142, DOI: **10.1016/j.snb.2019.127142**.

201 F. L. Jia, L. Z. Zhang, X. Y. Shang and Y. Yang, *Adv. Mater.*, 2008, **20**, 1050–1054, DOI: **10.1002/adma.200702159**.

202 S. Senapati, S. K. Srivastava, S. B. Singh and K. Biswas, *Cryst. Growth Des.*, 2010, **10**, 4068–4075, DOI: **10.1021/cg100740e**.

203 Z. Li, Z. Ma, Y. Wen, Y. Ren, Z. Wei, X. Xing, H. Sun, Y. W. Zhang and W. Song, *ACS Appl. Mater. Interfaces*, 2018, **10**, 26233–26240, DOI: **10.1021/acsami.8b06722**.

204 Y. L. Liao, W. X. Que, Q. Y. Jia, Y. C. He, J. Zhang and P. Zhong, *J. Mater. Chem.*, 2012, **22**, 7937–7944, DOI: **10.1039/C2JM16628C**.

205 Y. Wang, Y. He, Q. Lai and M. Fan, *J. Environ. Sci.*, 2014, **26**, 2139–2177, DOI: **10.1016/j.jes.2014.09.023**.

206 Z. Zhang, C. Wang, R. Zakaria and J. Y. Ying, *J. Phys. Chem. B*, 1998, **102**, 10871–10878, DOI: **10.1021/jp982948**.

207 M. Y. Guo, M. K. Fung, F. Fang, X. Y. Chen, A. M. C. Ng, A. B. Djurišić and W. K. Chan, *J. Alloys Compd.*, 2011, **509**, 1328–1332, DOI: **10.1016/j.jallcom.2010.10.028**.

208 X. Wang, S. Zhang, Y. Xie, H. Wang, H. Yu, Y. Shen, Z. Li, S. Zhang and F. Peng, *Int. J. Hydrogen Energy*, 2016, **41**, 20192–20197, DOI: **10.1016/j.ijhydene.2016.09.029**.

209 O. K. Varghese, M. Paulose and C. A. Grimes, *Nat. Nanotechnol.*, 2009, **4**, 592–597, DOI: **10.1038/nnano.2009.226**.

210 M. Ferroni, M. Carotta, V. Guidi, G. Martinelli, F. Ronconi, M. Sacerdoti and E. Traversa, *Sens. Actuators, B*, 2001, **77**, 163–166, DOI: **10.1016/S0925-4005(01)00688-8**.

211 M. Paulose, O. K. Varghese, G. K. Mor, C. A. Grimes and K. G. Ong, *Nanotechnology*, 2006, **17**, 398–402, DOI: **10.1088/0957-4484/17/2/009**.

212 H. Tokudome, Y. Yamada, S. Sonezaki, H. Ishikawa, M. Bekki and K. Kanehira, *Appl. Phys. Lett.*, 2005, **87**, 213901, DOI: **10.1063/1.2135392**.

213 Y. G. Guo, Y. S. Hu and J. Maier, *Chem. Commun.*, 2006, 2783–2785, DOI: **10.1039/B605090E**.

214 M. Minella, D. Versaci, S. Casino, F. Di Lupo, C. Minero, A. Battiato, N. Penazzi and S. Bodoardo, *Electrochim. Acta*, 2017, **230**, 132–140, DOI: **10.1016/j.electacta.2017.01.190**.

215 D. Y. Liang, C. Cui, H. H. Hu, Y. P. Wang, S. Xu, B. Ying, P. G. Li, B. Q. Lu and H. L. Shen, *J. Alloys Compd.*, 2014, **582**, 236–240, DOI: **10.1016/j.jallcom.2013.08.062**.

216 S. Jafari, B. Mahyad, H. Hashemzadeh, S. Janfaza, T. Gholikhani and L. Tayebi, *Int. J. Nanomed.*, 2020, **15**, 3447–3470, DOI: **10.2147/IJN.S249441**.

217 J. Roy, *J. Ind. Eng. Chem.*, 2022, **106**, 1–19, DOI: **10.1016/j.jiec.2021.10.024**.

218 M. A. Lara, M. J. Sayagués, J. A. Navío and M. C. Hidalgo, *J. Mater. Sci.*, 2018, **53**, 435–446, DOI: **10.1007/s10853-017-1515-6**.

219 D. Dahlan, S. K. Md Saad, A. U. Berli, A. Bajili and A. A. Umar, *Phys. E*, 2017, **91**, 185–189, DOI: 10.1016/j.physe.2017.05.003.

220 H. Z. Yao, W. Y. Fu, L. Liu, X. Li, D. Ding, P. Y. Su, S. Feng and H. B. Yang, *J. Alloys Compd.*, 2016, **680**, 206–211, DOI: 10.1016/j.jallcom.2016.04.133.

221 B. Babu, K. Mallikarjuna, C. V. Reddy and J. Park, *Mater. Lett.*, 2016, **176**, 265–269, DOI: 10.1016/j.matlet.2016.04.146.

222 J. Y. Su, L. Zhu, P. Geng and G. H. Chen, *J. Hazard. Mater.*, 2016, **316**, 159–168, DOI: 10.1016/j.jhazmat.2016.05.004.

223 D. P. Kumar, N. L. Reddy, M. Karthikeyan, N. Chinnaiah, V. Bramhaiah, V. D. Kumari and M. V. Shankar, *J. Colloid Interface Sci.*, 2016, **477**, 201–208, DOI: 10.1016/j.jcis.2016.05.014.

224 G. Liu, J. Y. Liao, A. Duan, Z. Zhang, M. Fowler and A. Yu, *J. Mater. Chem. A*, 2013, **1**, 12255–12262, DOI: 10.1039/C3TA12329D.

225 G. Huang, C.-H. Lu and H.-H. Yang, *Novel Nanomaterials for Biomedical, Environmental and Energy Applications*, ed. X. Wang and X. Chen, Elsevier, Amsterdam, 1st edn, 2019, chapter 3, pp. 89–109, DOI: 10.1016/B978-0-12-814497-8.00003-5.

226 W. Dong, H. Li, J. Xi, J. Mu, Y. Huang, Z. Ji and X. Wu, *J. Alloys Compd.*, 2017, **724**, 280–286, DOI: 10.1016/j.jallcom.2017.06.246.

227 L. Huang, T. M. Liu, H. J. Zhang, W. W. Guo and W. Zeng, *J. Mater. Sci.: Mater. Electron.*, 2012, **23**, 2024–2029, DOI: 10.1007/s10854-012-0697-6.

228 M. Liu, L. Piao, W. Lu, S. Ju, L. Zhao, C. Zhou, H. Li and W. Wang, *Nanoscale*, 2010, **2**, 1115–1117, DOI: 10.1039/C0NR00050G.

229 X. Yang, C. Jin, C. Liang, D. Chen, M. Wu and J. C. Yu, *Chem. Commun.*, 2011, **47**, 1184–1186, DOI: 10.1039/C0CC04216A.

230 Q. Xiang and J. Yu, *Chin. J. Catal.*, 2011, **32**, 525–531, DOI: 10.1016/S1872-2067(10)60186-6.

231 J. Y. Liao, B. X. Lei, D. B. Kuang and C. Y. Su, *Energy Environ. Sci.*, 2011, **4**, 4079–4085, DOI: 10.1039/C1EE01574E.

232 J. Harris, R. Silk, M. Smith, Y. Dong, W. T. Chen and G. I. N. Waterhouse, *ACS Omega*, 2020, **5**, 18919–18934, DOI: 10.1021/acsomega.0c02142.

233 A. Q. D. Faisal, *J. Mater. Sci.: Mater. Electron.*, 2015, **26**, 317–321, DOI: 10.1007/s10854-014-2402-4.

234 H. Xu, G. Li, G. Zhu, K. Zhu and S. Jin, *Catal. Commun.*, 2015, **62**, 52–56, DOI: 10.1016/j.catcom.2015.01.001.

235 Z. Song, H. Zhou, P. Tao, B. Wang, J. Mei, H. Wang, S. Wen, Z. Song and G. Fang, *Mater. Lett.*, 2016, **180**, 179–183, DOI: 10.1016/j.matlet.2016.05.178.

236 J. Ma, W. Ren, J. Zhao and H. Yang, *J. Alloys Compd.*, 2017, **692**, 1004–1009, DOI: 10.1016/j.jallcom.2016.09.134.

237 S. Shamsudin, M. K. Ahmad, N. Nafarizal, C. F. Soon, R. A. Rahim, D. A. Alakendram, M. Shimomura and K. Murakami, *Int. J. Integr. Eng.*, 2020, **12**, 197–205.

238 H. Siddiqui, M. S. Qureshi and F. Z. Haque, *Optik*, 2016, **127**, 2740–2747, DOI: 10.1016/j.ijleo.2015.11.220.

239 R. M. Mohamed, F. A. Harraz and A. Shawky, *Ceram. Int.*, 2014, **40**, 2127–2133, DOI: 10.1016/j.ceramint.2013.07.129.

240 R. Al-Gaashani, S. Radiman, N. Tabet and A. R. Daud, *J. Alloys Compd.*, 2011, **509**, 8761–8769, DOI: 10.1016/j.jallcom.2011.06.056.

241 X. Zhao, P. Wang, Z. Yan and N. Ren, *Opt. Mater.*, 2015, **42**, 544–547, DOI: 10.1016/j.optmat.2014.12.032.

242 M. Yin, C. K. Wu, Y. B. Lou, C. Burda, J. T. Koberstein, Y. M. Zhu and S. O'Brien, *J. Am. Chem. Soc.*, 2005, **127**, 9506–9511, DOI: 10.1021/ja050006u.

243 K. Zhou, R. Wang, B. Xu and Y. Li, *Nanotechnology*, 2006, **17**, 3939–3943, DOI: 10.1088/0957-4484/17/15/055.

244 Y. Xu, D. Chen and X. J. Jiao, *J. Phys. Chem. B*, 2005, **109**, 13561–13566, DOI: 10.1021/jp051577b.

245 J. Ramirez-Ortiz, T. Ogura, J. Medina-Valtierra, S. E. Acosta-Ortiz, P. Bosch, J. A. D. I. Reyes and V. H. Lara, *Appl. Surf. Sci.*, 2001, **174**, 177–184, DOI: 10.1016/S0169-4332(00)00822-9.

246 M. L. Zhong, D. C. Zeng, Z. W. Liu, H. Y. Yu, X. C. Zhong and W. Q. Qiu, *Acta Mater.*, 2010, **58**, 5926–5932, DOI: 10.1016/j.actamat.2010.07.008.

247 C. L. Hsu, J. Y. Tsai and T. J. Hsueh, *Sens. Actuators, B*, 2016, **224**, 95–102, DOI: 10.1016/j.snb.2015.10.018.

248 M. Wan, D. Jin, R. Feng, L. Si, M. Gao and L. Yue, *Inorg. Chem. Commun.*, 2011, **14**, 38–41, DOI: 10.1016/j.inoche.2010.09.025.

249 A. Ananth, S. Dharaneedharan, M. S. Heo and Y. S. Mok, *Chem. Eng. J.*, 2015, **262**, 179–188, DOI: 10.1016/j.cej.2014.09.083.

250 Udayabhanu, P. C. Nethravati, M. A. P. Kumar, D. Suresh, K. Lingaraju, H. Rajanaika, H. Nagabhushana and S. C. Sharma, *Mater. Sci. Semicond. Process.*, 2015, **33**, 81–88, DOI: 10.1016/j.mssp.2015.01.034.

251 R. C. Wang, S. N. Lin and J. Y. Liu, *J. Alloys Compd.*, 2017, **696**, 79–85, DOI: 10.1016/j.jallcom.2016.11.214.

252 X. Liu, J. Chen, P. Liu, H. Zhang, G. Li, T. An and H. Zhao, *Appl. Catal., A*, 2016, **521**, 34–41, DOI: 10.1016/j.apcata.2015.10.005.

253 D. Das, B. C. Nath, P. Phukon and S. K. Dolui, *Colloids Surf., B*, 2013, **101**, 430–433, DOI: 10.1016/j.colsurfb.2012.07.002.

254 T. Andana, M. Piumetti, S. Bensaid, L. Veyre, C. Thieuleux, N. Russo, D. Fino, E. A. Quadrelli and R. Pirone, *Appl. Catal., B*, 2017, **216**, 41–58, DOI: 10.1016/j.apcatb.2017.05.061.

255 R. Dang, X. Jia, X. Liu, H. Ma, H. Gao and G. Wang, *Nano Energy*, 2017, **33**, 427–435, DOI: 10.1016/j.nanoen.2017.01.024.

256 X. Wang, X. Wu, L. Yuan, K. Huang and S. Feng, *Mater. Des.*, 2017, **113**, 297–304, DOI: 10.1016/j.matdes.2016.10.029.

257 A. P. M. Udayan and S. N. Sawant, *J. Phys. Chem. Solids*, 2021, **150**, 109883, DOI: 10.1016/j.jpcs.2020.109883.

258 M. Fang, R. Zheng, Y. Wu, D. Yue, X. Qian, Y. Zhao and Z. Bian, *Environ. Sci.: Nano*, 2019, **6**, 105–114, DOI: 10.1039/C8EN00930A.

259 L. Zhang, Y. C. Zhu, Y. Y. Liang, W. W. Zhao, J. J. Xu and H. Y. Chen, *Anal. Chem.*, 2018, **90**, 5439–5444, DOI: 10.1021/acs.analchem.8b00742.

260 L. Xu, Q. Yang, X. Liu, J. Liu and X. Suna, *RSC Adv.*, 2014, **4**, 1449–1455, DOI: 10.1039/C3RA45598J.

261 S. Anantharaj, H. Sugime and S. Noda, *ACS Appl. Mater. Interfaces*, 2020, **12**, 27327–27338, DOI: 10.1021/acsami.0c08979.

262 C. X. Wang, W. Zeng, T. F. Li and Y. Q. Li, *Mater. Technol.*, 2014, **30**, 205–212, DOI: 10.1179/1753555714Y.0000000243.

263 L. Yu, G. Zhang, Y. Wu, X. Bai and D. Guo, *J. Cryst. Growth*, 2008, **310**, 3125–3130, DOI: 10.1016/j.jcrysgro.2008.03.026.

264 S. Zaman, M. H. Asif, A. Zainelabdin, G. Amin, O. Nur and M. Willander, *J. Electroanal. Chem.*, 2011, **662**, 421–425, DOI: 10.1016/j.jelechem.2011.09.015.

265 B. Heng, C. Qing, D. Sun, B. Wang, H. Wang and Y. Tang, *RSC Adv.*, 2013, **3**, 15719–15726, DOI: 10.1039/C3RA42869A.

266 M. Umadevi and A. Jegatha Christy, *Spectrochim. Acta, Part A*, 2013, **109**, 133–137, DOI: 10.1016/j.saa.2013.02.028.

267 J. Liao, H. Li, X. Zhang and D. Xiao, *Micro Nano Lett.*, 2014, **9**, 432–436, DOI: 10.1049/mnl.2014.0199.

268 S. K. Shinde, D. P. Dubal, G. S. Ghodakec and V. J. Fulari, *RSC Adv.*, 2015, **5**, 4443–4447, DOI: 10.1039/C4RA11164H.

269 J. Ye, Z. Li, Z. Dai, Z. Zhang, M. Guo and X. Wang, *J. Electron. Mater.*, 2016, **45**, 4237–4245, DOI: 10.1007/s11664-016-4587-1.

270 F. Nishino, M. Jeem, L. Zhang, K. Okamoto, S. Okabe and S. Watanabe, *Sci. Rep.*, 2017, **7**, 1063, DOI: 10.1038/s41598-017-01194-5.

271 G. Bhanjana, N. Dilbaghi, K. H. Kim and S. Kumar, *J. Mol. Liq.*, 2017, **244**, 506–511, DOI: 10.1016/j.molliq.2017.09.034.

272 F. Gao, L. Zhu, H. Li and H. Xie, *Mater. Res. Bull.*, 2017, **93**, 342–351, DOI: 10.1016/j.materresbull.2017.05.033.

273 R. Yuan, H. Li, X. Yin, L. Zhang and J. Lu, *J. Mater. Sci. Technol.*, 2018, **34**, 1692–1698, DOI: 10.1016/j.jmst.2017.11.030.

274 N. K. Yetim, N. Aslan, A. Sarıoğlu, N. Sarı and M. M. Koç, *J. Mater. Sci.: Mater. Electron.*, 2020, **31**, 12238–12248, DOI: 10.1007/s10854-020-03769-x.

275 S. Ganguly, R. Jha, P. K. Guha and C. Jacob, *J. Electron. Mater.*, 2020, **49**, 5070–5076, DOI: 10.1007/s11664-020-08246-z.

276 B. Miao, W. Zeng, L. Y. Lin and S. Xu, *Phys. E*, 2013, **52**, 40–45, DOI: 10.1016/j.physe.2013.03.006.

277 X. Yan, X. Tong, J. Wang, C. Gong, M. Zhang and L. Liang, *J. Alloys Compd.*, 2013, **556**, 56–61, DOI: 10.1016/j.jallcom.2012.12.124.

278 X. Li, W. Liu, J. Ma, Y. Wen and Z. Wu, *Appl. Catal., B*, 2015, **179**, 239–248, DOI: 10.1016/j.apcatb.2015.05.034.

279 Z. Skoufa, E. Heracleous and A. A. Lemonidou, *J. Catal.*, 2015, **322**, 118–129, DOI: 10.1016/j.jcat.2014.11.014.

280 Y. J. Mai, J. P. Tu, X. H. Xia, C. D. Gu and X. L. Wang, *J. Power Sources*, 2011, **196**, 6388–6393, DOI: 10.1016/j.jpowsour.2011.03.089.

281 S. G. Hwang, G. O. K. Kim, S. R. Yun and K. S. Ryu, *Electrochim. Acta*, 2012, **78**, 406–411, DOI: 10.1016/j.electacta.2012.06.031.

282 X. Wang, L. Li, Y. Zhang, S. Wang, Z. Zhang, L. Fei and Y. Qian, *Cryst. Growth Des.*, 2006, **6**, 2163–2165, DOI: 10.1021/cg060156w.

283 D. Su, H. S. Kim, W. S. Kim and G. Wang, *Chem.–Eur. J.*, 2012, **18**, 8224–8229, DOI: 10.1002/chem.201200086.

284 B. Varghese, M. V. Reddy, Z. Yanwu, C. S. Lit, T. C. Hoong, G. V. Subba Rao, B. V. R. Chowdari, A. T. S. Wee, C. T. Lim and C. H. Sow, *Chem. Mater.*, 2008, **20**, 3360–3367, DOI: 10.1021/cm703512k.

285 S. A. Needham, G. X. Wang and H. K. Liu, *J. Power Sources*, 2006, **159**, 254–257, DOI: 10.1016/j.jpowsour.2006.04.025.

286 M. Zhou, W. Xiong, H. Li, D. Zhang and Y. Lv, *Dalton Trans.*, 2021, **50**, 5835–5844, DOI: 10.1039/D1DT00213A.

287 Y. Pang, J. Zhang, D. Chen and X. Jiao, *RSC Adv.*, 2016, **6**, 30395, DOI: 10.1039/C5RA27715A.

288 D. K. Subbiah, K. Babu, A. Das and J. B. B. R. Rayappan, *ACS Appl. Mater. Interfaces*, 2019, **11**, 20045–20055, DOI: 10.1021/acsami.9b04682.

289 M. Tian, X. Hu, L. Qu, S. Zhu, Y. Sun and G. Han, *Carbon*, 2016, **96**, 1166–1174, DOI: 10.1016/j.carbon.2015.10.080.

290 L. Wang and H. Yu, *Springer Briefs in Molecular Science*, Springer Singapore, Singapore, 2018, DOI: 10.1007/978-981-10-6062-5.

291 M. A. Shah, *Nanoscale Res. Lett.*, 2008, **3**, 255–259, DOI: 10.1007/s11671-008-9147-z.

292 B. Zhao, X. K. Ke, J. H. Bao, C. L. Wang, L. Dong, Y. W. Chen and H. L. Chen, *J. Phys. Chem. C*, 2009, **113**, 14440–14447, DOI: 10.1021/jp904186k.

293 C. Xia, X. Yanjun and W. Ning, *Sens. Actuators, B*, 2011, **153**, 434–438, DOI: 10.1016/j.snb.2010.11.011.

294 X. Wang, L. Wan, T. Yu, Y. Zhou, J. Guan, Z. Yu, Z. Li and Z. Zou, *Mater. Chem. Phys.*, 2011, **126**, 494–499, DOI: 10.1016/j.matchemphys.2011.01.040.

295 F. Cao, F. Zhang, R. Deng, W. Hu, D. Liu, S. Song and H. Zhang, *CrystEngComm*, 2011, **13**, 4903, DOI: 10.1039/C1CE05237C.

296 P. Wu, J. H. Sun, Y. Y. Huang, G. F. Gu and D. G. Tong, *Mater. Lett.*, 2012, **82**, 191–194, DOI: 10.1016/j.matlet.2012.05.087.

297 S. Cao, W. Zeng, H. Long, J. Gong, Z. Zhu and L. Chen, *Mater. Lett.*, 2015, **161**, 275–277, DOI: 10.1016/j.matlet.2015.08.129.

298 A. Qurashi, Z. Zhang, M. Asif and T. Yamazaki, *Energy*, 2015, **40**, 15801–15805, DOI: 10.1016/j.ijhydene.2015.07.114.

299 J. Wang, W. Zeng and Z. Wang, *Ceram. Int.*, 2016, **42**, 4567–4573, DOI: 10.1016/j.ceramint.2015.11.150.

300 R. Miao and W. Zeng, *Mater. Lett.*, 2016, **171**, 200–203, DOI: 10.1016/j.matlet.2016.02.052.

301 S. Liu, W. Zeng and T. Chen, *Phys. E*, 2017, **85**, 13–18, DOI: 10.1016/j.physe.2016.08.016.

302 Y. Zhang and W. Zeng, *Mater. Lett.*, 2017, **195**, 217–219, DOI: 10.1016/j.matlet.2017.02.124.

303 S. Munkaila, J. Bentley, K. Schimmel, T. Ahamad, S. M. Alshehri and B. S. Bastakoti, *J. Mol. Liq.*, 2021, **324**, 114676, DOI: 10.1016/j.molliq.2020.114676.

304 A. Chen, X. Peng, K. Koczkur and B. Miller, *Chem. Commun.*, 2004, **17**, 1964–1965, DOI: **10.1039/B407313D**.

305 J. Ning, Q. Dai, T. Jiang, K. Men, D. Liu, N. Xiao, C. Li, D. Li, B. Liu, B. Zou, G. Zou and W. W. Yu, *Langmuir*, 2009, **25**, 1818–1821, DOI: **10.1021/la8037473**.

306 S. Zeng, K. Tang, T. Li, Z. Liang, D. Wang, Y. Wang, Y. Qi and W. Zhou, *J. Phys. Chem. C*, 2008, **112**, 4836–4843, DOI: **10.1021/jp0768773**.

307 H. P. Zhou, Y. W. Zhang, H. X. Mai, X. Sun, Q. Liu, W. G. Song and C. H. Yan, *Chem.–Eur. J.*, 2008, **14**, 3380–3390, DOI: **10.1002/chem.200701348**.

308 J. Ni, W. Lu, L. Zhang, B. Yue, X. Shang and Y. Lv, *J. Phys. Chem. C*, 2009, **113**, 54–60, DOI: **10.1021/jp806454r**.

309 V. Srivastava, Y. C. Sharma and M. Sillanpaa, *Ceram. Int.*, 2015, **41**, 6702–6709, DOI: **10.1016/j.ceramint.2015.01.112**.

310 L. Jiang, G. Li, Q. Ji and H. Peng, *Mater. Lett.*, 2007, **61**, 1964–1967, DOI: **10.1016/j.matlet.2006.07.167**.

311 Q. Li, H. Sun, M. Luo, W. Weng, K. Cheng, C. Song, P. Du, G. Shen and G. Han, *J. Alloys Compd.*, 2010, **503**, 514–518, DOI: **10.1016/j.jallcom.2010.05.043**.

312 G. Saito, S. Hosokai and T. Akiyama, *Mater. Chem. Phys.*, 2011, **130**, 79–83, DOI: **10.1016/j.matchemphys.2011.05.084**.

313 R. Shi, P. Yang, X. Dong, Q. Ma and A. Zhang, *Appl. Surf. Sci.*, 2013, **264**, 162–170, DOI: **10.1016/j.apsusc.2012.09.164**.

314 R. M. Tripathi, A. S. Bhadwal, R. K. Gupta, P. Singh, A. Shrivastav and B. R. Shrivastav, *J. Photochem. Photobiol., B*, 2014, **141**, 288–295, DOI: **10.1016/j.jphotobiol.2014.10.001**.

315 H. Wu, Z. Yuan, B. Wang, F. Nie, J. He, X. Wang and L. Liu, *Opt. Mater.*, 2021, **122**, 111683, DOI: **10.1016/j.optmat.2021.111683**.

316 J. K. Rajput, T. K. Pathak, H. C. Swart and L. P. Purohit, *Phys. Status Solidi A*, 2019, **216**, 1900093, DOI: **10.1002/pssa.201900093**.

317 C. Harito, S. Z. J. Zaidi, D. V. Bavykin, A. S. Martins, B. Yuliarto, F. C. Walsh and C. P. de Leon, *Adv. Nat. Sci.: Nanosci. Nanotechnol.*, 2020, **11**, 035018, DOI: **10.1088/2043-6254/abb238**.

318 Y. T. Tsai, S. J. Chang, L. W. Ji, Y. J. Hsiao, I. T. Tang, H. Y. Lu and Y. L. Chu, *ACS Omega*, 2018, **3**, 13798–13807, DOI: **10.1021/acsomega.8b01882**.

319 X. Y. Xue, Z. H. Chen, L. L. Xing, C. H. Ma, Y. J. Chen and T. H. Wang, *J. Phys. Chem. C*, 2010, **114**, 18607–18611, DOI: **10.1021/jp1070067**.

320 H. Liu, L. Shi, D. Li, J. Yu, H. M. Zhang, S. Ullah, B. Yang, C. Li, C. Zhu and J. Xu, *J. Power Sources*, 2018, **387**, 64–71, DOI: **10.1016/j.jpowsour.2018.03.047**.

321 W. Yu, M. D. Porosoff and J. G. Chen, *Chem. Rev.*, 2012, **112**, 5780–5817, DOI: **10.1021/cr300096b**.

322 J. Wang and H. Gu, *Molecules*, 2015, **20**, 17070–17092, DOI: **10.3390/molecules200917070**.

323 S. De, J. Zhang, R. Luque and N. Yan, *Energy Environ. Sci.*, 2016, **9**, 3314–3347, DOI: **10.1039/C6EE02002J**.

324 K. D. Gilroy, A. Ruditskiy, H. C. Peng, D. Qin and Y. Xia, *Chem. Rev.*, 2016, **116**, 10414–10472, DOI: **10.1021/acs.chemrev.6b00211**.

325 Y. Yan, J. S. Du, K. D. Gilroy, D. Yang, Y. Xia and H. Zhang, *Adv. Mater.*, 2017, **29**, 1605997, DOI: **10.1002/adma.201605997**.

326 C. Rice, S. Ha, R. I. Masel and A. Wieckowski, *J. Power Sources*, 2003, **115**, 229, DOI: **10.1016/S0378-7753(03)00026-0**.

327 Y. M. Zhu, Z. Khan and R. I. Masel, *J. Power Sources*, 2005, **139**, 15–20, DOI: **10.1016/j.jpowsour.2004.06.054**.

328 X. W. Yu and P. G. Pickup, *J. Power Sources*, 2008, **182**, 124–132, DOI: **10.1016/j.jpowsour.2008.03.075**.

329 W. P. Zhou, A. Lewera, R. Larsen, R. I. Masel, P. S. Bagus and A. Wieckowski, *J. Phys. Chem. B*, 2006, **110**, 13393, DOI: **10.1021/jp061690h**.

330 W. J. Zhou and J. Y. Lee, *J. Phys. Chem. C*, 2008, **112**, 3789, DOI: **10.1021/jp077068m**.

331 C. Y. Du, M. Chen, W. G. Wang, G. P. Yin and P. F. Shi, *Electrochem. Commun.*, 2010, **12**, 843, DOI: **10.1016/j.elecom.2010.03.046**.

332 D. Morales-Acosta, J. Ledesma-Garcia, L. A. Godinez, H. G. Rodriguez, L. Alvarez-Contreras and L. G. Arriaga, *J. Power Sources*, 2010, **195**, 461, DOI: **10.1016/j.jpowsour.2009.08.014**.

333 V. Mazumder, M. F. Chi, M. N. Mankin, Y. Liu, O. Metin, D. H. Sun, K. L. More and S. H. Sun, *Nano Lett.*, 2012, **12**, 1102, DOI: **10.1021/nl2045588**.

334 C. X. Xu, Y. Q. Liu, J. P. Wang, H. R. Geng and H. J. Qiu, *J. Power Sources*, 2012, **199**, 124, DOI: **10.1016/j.jpowsour.2011.10.075**.

335 X. Wang, Y. Tang, Y. Gao and T. H. Lu, *J. Power Sources*, 2008, **175**, 784–788, DOI: **10.1016/j.jpowsour.2007.10.011**.

336 T. Ma, F. Liang, R. Chen, S. Liu and H. Zhang, *Nanomaterials*, 2017, **7**, 239, DOI: **10.3390/nano7090239**.

337 T. Ma, W. Yang, S. Liu, H. Zhang and F. A. Liang, *Catalysts*, 2017, **7**, 38, DOI: **10.3390/catal7020038**.

338 Y. W. Lee, M. Kim, Y. Kim, S. W. Kang, J. H. Lee and S. W. Han, *J. Phys. Chem. C*, 2010, **114**, 7689–7693, DOI: **10.1021/jp9119588**.

339 Y. Han, X. Yang, Y. Liu, Q. Ai, S. Liu, C. Sun and F. Liang, *Sci. Rep.*, 2016, **6**, 22239, DOI: **10.1038/srep22239**.

340 R. S. Downing, P. J. Kunkeler and H. V. Bekkum, *Catal. Today*, 1997, **37**, 121–136, DOI: **10.1016/S0920-5861(97)00005-9**.

341 A. Li, W. Duan, J. Liu, K. Zhuo, Y. Chen and J. Wang, *Sci. Rep.*, 2018, **8**, 13141, DOI: **10.1038/s41598-018-31402-9**.

342 Y. Imura, R. Akiyama, S. Furukawa, R. Kan, C. Morita-Imura, T. Komatsu and T. Kawai, *Chem.–Asian J.*, 2019, **14**, 547–552, DOI: **10.1002/asia.201801711**.

343 S. Yamazoe, K. Koyasu and T. Tsukuda, *Acc. Chem. Res.*, 2014, **47**, 816–824, DOI: **10.1021/ar400209a**.

344 Z. Cao, H. Chen, S. Zhu, W. Zhang, X. Wu, G. Shan, U. Ziener and D. Qi, *Langmuir*, 2015, **31**, 4341–4350, DOI: **10.1021/acs.langmuir.5b00437**.

345 Z. Cao, H. Chen, S. Zhu, Z. Chen, C. Xu, D. Qi and U. Ziener, *Colloids Surf., A*, 2016, **489**, 223–233, DOI: 10.1016/j.colsurfa.2015.11.001.

346 C. M. Imura, T. Mori, Y. Imura and T. Kawai, *New J. Chem.*, 2016, **40**, 7048–7052, DOI: 10.1021/acsomega.1c01895.

347 Y. Imura, S. Furukawa, K. Ozawa, C. Morita-Imura, T. Kawai and T. Komatsu, *RSC Adv.*, 2016, **6**, 17222–17227, DOI: 10.1039/C5RA27146K.

348 J. A. Lopez-Sanchez, N. Dimitratos, C. Hammond, G. L. Brett, L. Kesavan, S. White, P. Miedziak, R. Tiruvalam, R. L. Jenkins, A. F. Carley, D. Knight, C. J. Kiely and G. J. Hutchings, *Nat. Chem.*, 2011, **3**, 551–556, DOI: 10.1038/nchem.1066.

349 Z. Niu and Y. Li, *Chem. Mater.*, 2014, **26**, 72–83, DOI: 10.1021/cm4022479.

350 L. Zhang, X. F. Zhang, X. L. Chen, A. J. Wang, D. M. Han, Z. G. Wang and J. J. Feng, *J. Colloid Interface Sci.*, 2019, **536**, 556–562, DOI: 10.1016/j.jcis.2018.10.080.

351 G. D. Rodrigues, L. R. de Lemos, L. H. M. da Silva and M. C. H. da Silva, *J. Chromatogr. A*, 2013, **1279**, 13–19, DOI: 10.1016/j.chroma.2013.01.003.

352 Y. Wang, B. Ouyang, B. Zhang, Y. Boluo, Y. Huang, R. V. Ramanujan, K. K. Ostrikov and R. S. Rawat, *J. Phys. D: Appl. Phys.*, 2020, **53**, 225201, DOI: 10.1088/1361-6463/ab7797.

353 M. Li, H. Zheng, G. Han, Y. Xiao and Y. Li, *Catal. Commun.*, 2017, **92**, 95–99, DOI: 10.1016/j.catcom.2017.01.014.

354 Q. Zhou, L. Qi, H. Yang and C. Xu, *J. Colloid Interface Sci.*, 2018, **513**, 258–265, DOI: 10.1016/j.jcis.2017.11.040.

355 G. Fu, K. Wu, J. Lin, Y. Tang, Y. Chen, Y. Zhou and T. Lu, *J. Phys. Chem. C*, 2013, **117**, 9826–9834, DOI: 10.1021/jp400502y.

356 S. S. Chen, X. X. Lin, A. J. Wang, H. Huang and J. J. Feng, *Sens. Actuators, B*, 2017, **248**, 214–222, DOI: 10.1016/j.snb.2017.03.129.

357 A. Chalgin, F. Shi, F. Li, Q. Xiang, W. Chen, C. Song, P. Tao, W. Shang, T. Deng and J. Wu, *CrystEngComm*, 2017, **19**, 6964–6971, DOI: 10.1039/C7CE01721A.

358 H. Xu, B. Yan, K. Zhang, C. Wang, J. Zhong, S. Li, Y. Du and P. Yang, *Colloids Surf., A*, 2017, **522**, 335–345, DOI: 10.1016/j.colsurfa.2017.03.015.

359 X. Guo, H. Shang, J. Guo, H. Xu and Y. Du, *Appl. Surf. Sci.*, 2019, **481**, 1532–1537, DOI: 10.1016/j.apsusc.2019.03.234.

360 H. M. An, Z. L. Zhao, L. Y. Zhang, Y. Chen, Y. Y. Chang and C. M. Li, *ACS Appl. Mater. Interfaces*, 2018, **10**, 41293–41298, DOI: 10.1021/acsami.8b13361.

361 I. Arief and P. K. Mukhopadhyay, *Phys. B*, 2014, **448**, 73–76, DOI: 10.1016/j.physb.2014.04.068.

362 H. J. Kim, S. J. Lee, S. Y. Park, J. H. Jung and J. S. Kim, *Adv. Mater.*, 2008, **20**, 3229–3234, DOI: 10.1002/adma.200800246.

363 F. Torney, B. G. Trewyn, V. S. Y. Lin and K. Wang, *Nat. Nanotechnol.*, 2007, **2**, 295–300, DOI: 10.1038/nnano.2007.108.

364 D. Zhao, Q. Huo, J. Feng, B. F. Chmelka and G. D. Stucky, *J. Am. Chem. Soc.*, 1998, **120**, 6024–6036, DOI: 10.1021/ja974025i.

365 W. Pan, J. Ye, G. Ning, Y. Lin and J. Wang, *Mater. Res. Bull.*, 2009, **44**, 280–283, DOI: 10.1016/j.materresbull.2008.06.006.

366 J. S. Kang, J. Lim, W. Y. Rho, J. Kim, D. S. Moon, J. Jeong, D. Jung, J. W. Choi, J. K. Lee and Y. E. Sung, *Sci. Rep.*, 2016, **6**, 30829, DOI: 10.1038/srep30829.

367 J. E. Lee, N. Lee, H. Kim, J. Kim, S. H. Choi, J. H. Kim, T. Kim, I. C. Song, S. P. Park, W. K. Moon and T. Hyeon, *J. Am. Chem. Soc.*, 2010, **132**, 552–557, DOI: 10.1021/ja905793q.

368 N. K. Mal, M. Fujiwara and Y. Tanaka, *Nature*, 2003, **421**, 350–353, DOI: 10.1038/nature01362.

369 L. Wang, X. Liu, Y. Jiang, P. Liu, L. Zhou, L. Ma, Y. He, H. Li and J. Gao, *Catalysts*, 2019, **9**(12), 1026, DOI: 10.3390/catal9121026.

370 X. L. Liu, C. T. Ng, P. Chandrasekharan, H. T. Yang, L. Y. Zhao, E. Peng, Y. B. Lv, W. Xiao, J. Fang, J. B. Yi, H. Zhang, K. H. Chuang, B. H. Bay, J. Ding and H. M. Fan, *Adv. Healthcare Mater.*, 2016, **5**, 2092–2104, DOI: 10.1002/adhm.201600357.

371 J. Xu, A. R. Wilson, A. R. Rathmell, J. Howe, M. Chi and B. J. Wiley, *ACS Nano*, 2011, **5**, 6119–6127, DOI: 10.1021/nn201161m.

372 S. Yin, Z. Wang, S. Liu, S. Jiao, W. Tian, Y. Xu, X. Li, L. Wang and H. Wang, *Nanoscale*, 2021, **13**, 3208–3213, DOI: 10.1039/D0NR08758K.

373 X. Qiu, Y. Dai, Y. Tang, T. Lu, S. Wei and Y. Chen, *J. Power Sources*, 2015, **278**, 430–435, DOI: 10.1039/C8CC02816H.

374 Y. Lai, L. Dong, R. Liu, S. Lu, Z. He, W. Shan, F. Geng, Y. Cai and J. Liu, *Chin. Chem. Lett.*, 2020, **31**, 2437–2441, DOI: 10.1016/j.cclet.2020.04.050.

375 W. Yan, L. Yang, H. Wang, J. Zhang and W. Shen, *Nanoscale*, 2018, **10**, 15661–15668, DOI: 10.1039/C8NR04196B.

376 M. P. D. S. Rodrigues, A. H. B. Dourado, L. D. O. Cutolo, L. S. Parreira, T. V. Alves, T. J. A. Slater, S. J. Haigh, P. H. C. Camargo and S. I. C. de Torresi, *ACS Catal.*, 2021, **11**, 13543–13555, DOI: 10.1021/acscatal.1c02938.

377 A. T. N. Nguyen and J. H. Shim, *Appl. Surf. Sci.*, 2018, **458**, 910–916, DOI: 10.1016/j.apsusc.2018.07.161.

378 Y. Ren, X. Yang, L. Li, C. Li, X. Zhang, Z. Lu and X. Yu, *Catal. Lett.*, 2020, **150**, 3415–3423, DOI: 10.1007/s10562-020-03242-8.

379 Y. Xiong, S. Chen, F. Ye, L. Su, C. Zhang, S. Shen and S. Zhao, *Anal. Methods*, 2015, **7**, 1300–1306, DOI: 10.1039/C4AY02687J.

380 Y. Zhao, L. Hu, S. Zhao and L. Wu, *Adv. Funct. Mater.*, 2016, **26**, 4085–4093, DOI: 10.1002/adfm.201600494.

381 M. Wang and X. Zhang, *ChemistrySelect*, 2017, **2**, 9537–9545, DOI: 10.1002/slct.201700746.

382 N. Zhang, C. Xu, H. Wang, J. Zhang, Y. Liu and Y. Fang, *J. Mater. Sci.: Mater. Electron.*, 2021, **32**, 1787–1799, DOI: 10.1007/s10854-020-04947-7.

383 Y. Yang, T. Liu, L. Zhang, S. Zhao, W. Zeng, S. Hussain, C. Deng, H. Pan and X. Peng, *J. Mater. Sci.: Mater. Electron.*, 2016, **27**, 6202–6207, DOI: 10.1007/s10854-016-4550-1.

384 X. Dou, D. Sabba, N. Mathews, L. H. Wong, Y. M. Lam and S. Mhaisalkar, *Chem. Mater.*, 2011, **23**, 3938–3945, DOI: 10.1021/cm201366z.

385 X. Zheng, Y. Li, Y. Zheng, L. Shen, Y. Xiao, Y. Cao, Y. Zhang, C. Au and L. Jiang, *ACS Catal.*, 2020, **10**, 3968–3983, DOI: 10.1021/acscatal.9b05486.

386 L. Zhou, X. Zhou, C. Zhao, Y. Liu, Y. Li, L. Ma, Y. He, Y. Jiang and J. Gao, *Microchem. J.*, 2021, **165**, 106169, DOI: 10.1016/j.microc.2021.106169.

387 Y. Imura, S. Hojo, C. Morita and T. Kawai, *Langmuir*, 2014, **30**, 1888–1892, DOI: 10.1021/la403681w.

388 Y. Lu, Y. Yin, Z.-Y. Li and Y. Xia, *Nano Lett.*, 2002, **2**, 785–788, DOI: 10.1021/nl025598i.

389 H. K. Sadhanala, S. Senapati, K. V. Harika, K. K. Nanda and A. Gedanken, *New J. Chem.*, 2018, **42**, 14318–14324, DOI: 10.1039/C8NJ01731J.

390 S. Santhosh, M. Sathish, S. Iyer, S. Kalluri and A. Madhavan, *Mater. Lett.*, 2021, **302**, 130343, DOI: 10.1016/j.matlet.2021.130343.

391 X. Sun, P. Yang, S. Wang, C. Jin, M. Ren and H. Xing, *Langmuir*, 2021, **37**, 10403–10412, DOI: 10.1021/acs.langmuir.1c00737.

392 F. Zhao, H. Yang, K. Qin, G. Cui and Q. Liu, *J. Taiwan Inst. Chem. Eng.*, 2021, **126**, 244–251, DOI: 10.1016/j.jtice.2021.06.054.

393 Q. Dai, N. Xiao, J. Ning, C. Li, D. Li, B. Zou, W. W. Yu, S. Kan, H. Chen, B. Liu and G. Zou, *J. Phys. Chem. C*, 2008, **112**, 7567–7571, DOI: 10.1021/jp7120559.

394 Q. Zeng, S. Xue, S. Wu, K. Gan, L. Xu, J. Han, W. Zhou and R. Zou, *Ceram. Int.*, 2014, **40**, 2847–2852, DOI: 10.1016/j.ceramint.2013.10.029.

395 A. Alemi, A. Babalou, M. Dolatyari, A. Klein and G. Meyer, *Z. Anorg. Allg. Chem.*, 2009, **635**, 2053–2057, DOI: 10.1002/zaac.200900028.

396 N. Cao, K. Hu, W. Luo and G. Z. Cheng, *J. Alloys Compd.*, 2014, **590**, 241–246, DOI: 10.1016/j.jallcom.2013.12.134.

397 M. Rakap, *J. Power Sources*, 2015, **276**, 320–327, DOI: 10.1016/j.jpowsour.2014.11.146.

398 D. D. Ke, Y. Li, J. Wang, L. Zhang, J. D. Wang, X. Zhao, S. Yang and S. Han, *Int. J. Hydrogen Energy*, 2016, **41**, 2564–2574, DOI: 10.1016/j.ijhydene.2015.11.142.

399 Z. Zhang, Y. Jiang, M. Chi, Z. Yang, C. Wang and X. Lu, *RSC Adv.*, 2015, **5**, 94456–94461, DOI: 10.1039/C5RA18698F.

400 A. J. Amali, K. Aranishi, T. Uchida and Q. Xu, *Part. Part. Syst. Charact.*, 2013, **30**, 888–892, DOI: 10.1002/ppsc.201300100.

401 X. J. Yang, F. Y. Cheng, J. Liang, Z. L. Tao and J. Chen, *Int. J. Hydrogen Energy*, 2009, **34**, 8785–8791, DOI: 10.1016/j.ijhydene.2009.08.075.

402 G. P. Rachiero, U. B. Demirci and P. Miele, *Int. J. Hydrogen Energy*, 2011, **36**, 7051–7065, DOI: 10.1016/j.ijhydene.2011.03.009.

403 Y. Yang, Z.-H. Lu, Y. Hu, Z. Zhang, W. Shi, X. Chen and T. Wang, *RSC Adv.*, 2014, **4**, 13749–13752, DOI: 10.1039/C3RA47023G.

404 H. Ahmed, P. Adebayo, M. Ahmed and A. I. Atbab, *J. Energy Technol. Policy*, 2023, **13**, 1, DOI: 10.7176/JETP/13-1-07.

405 A. Morozan, B. Jousselme and S. Palacin, *Energy Environ. Sci.*, 2011, **4**, 1238–1254, DOI: 10.1039/C0EE00601G.

406 S. Zhang, C. Zhao, Y. Liu, W. Li, J. Wang, G. Wang, Y. Zhang, H. Zhang and H. Zhao, *Chem. Commun.*, 2019, **55**, 2952–2955, DOI: 10.1039/C9CC00123A.

407 T. L. Frölicher, E. M. Fischer and N. Gruber, *Nature*, 2018, **560**, 360–364, DOI: 10.1038/s41586-018-0383-9.

408 J. Wang, L. Yu, L. Hu, G. Chen, H. Xin and X. Feng, *Nat. Commun.*, 2018, **9**, 1795, DOI: 10.1038/s41467-018-04213-9.

409 H. Wang, S. Liu, H. Zhang, S. Yin, Y. Xu, X. Li, Z. Wang and L. Wang, *Nanoscale*, 2020, **12**, 13507–13512, DOI: 10.1039/D0NR02884C.

410 X. Wu, L. Xia, Y. Wang, W. Lu, Q. Liu, X. Shi and X. Sun, *Small*, 2018, **14**, 1803111, DOI: 10.1002/smll.201803111.

411 X. Xiang, Z. Wang, X. Shi, M. Fan and X. Sun, *ChemCatChem*, 2018, **10**, 4530–4535, DOI: 10.1002/cctc.201801208.

412 K. Chu, Y. Liu, J. Wang and H. Zhang, *ACS Appl. Energy Mater.*, 2019, **2**, 2288–2295, DOI: 10.1021/acsaem.9b00102.

413 Y. Chen, B. Wu, B. Sun, N. Wang, W. Hu and S. Komarneni, *ACS Sustainable Chem. Eng.*, 2019, **7**, 18874–18883, DOI: 10.1021/acssuschemeng.9b04024.

414 M. Reddeppa, B.-G. Park, G. Murali, S. H. Choi, N. D. Chinh, D. Kim, W. Yang and M.-D. Kim, *Sens. Actuators, B*, 2020, **308**, 127700, DOI: 10.1016/j.snb.2020.127700.

415 Q. Zhang, G. Xie, M. Xu, Y. Su, H. Tai, H. Du and Y. Jiang, *Sens. Actuators, B*, 2018, **259**, 269–281, DOI: 10.1016/j.snb.2017.12.052.

416 H.-Y. Li, J.-W. Yoon, C.-S. Lee, K. Lim, J.-W. Yoon and J.-H. Lee, *Sens. Actuators, B*, 2018, **255**, 2963–2970, DOI: 10.1016/j.snb.2017.09.118.

417 C. Zhang, A. Boudiba, P. De Marco, R. Snyders, M.-G. Olivier and M. Debliquy, *Sens. Actuators, B*, 2013, **181**, 395–401, DOI: 10.1016/j.snb.2013.01.082.

418 A. S. Chizhov, M. N. umyantseva, R. B. Vasiliev, D. G. Filatova, K. A. Drozdov, I. V. Krylov, A. M. Abakumov and A. M. Gaskov, *Sens. Actuators, B*, 2014, **205**, 305–312, DOI: 10.1016/j.snb.2014.08.091.

419 C. Chen, Q. Zhang, G. Xie, M. Yao, H. Pan, H. Du, H. Tai, X. Du and Y. Su, *Mater. Res. Express*, 2020, **7**, 015924, DOI: 10.1088/2053-1591/ab6b64.

420 X. Geng, D. Lahem, C. Zhang, C.-J. Li, M.-G. Olivier and M. Debliquy, *Ceram. Int.*, 2019, **45**, 4253–4261, DOI: 10.1016/j.ceramint.2018.11.097.

421 L. Giancaterini, S. M. Emamjomeh, A. De Marcellis, E. Palange, A. Resmini, U. Anselmi-Tamburini and C. Cantalini, *Sens. Actuators, B*, 2016, **229**, 387–395, DOI: 10.1016/j.snb.2016.02.007.

422 S. Boukhalfa, K. Evanoff and G. Yushin, *Energy Environ. Sci.*, 2012, **5**, 6872, DOI: 10.1039/C2EE21110F.

423 X. F. Sun, Y. L. Xu, J. Wang and S. C. Mao, *Int. J. Electrochem. Sci.*, 2012, **7**, 3205–3214.

424 P. Lin, Q. J. She, B. L. Hong, X. A. J. Liu, Y. N. Shi, Z. Shi, M. S. Zheng and Q. F. Dong, *J. Electrochem. Soc.*, 2010, **157**, A818, DOI: 10.1149/1.3425624.

425 X. Zhang, W. Shi, J. Zhu, W. Zhao, J. Ma, S. Mhaisalkar, T. L. Maria, Y. Yang, H. Zhang, H. H. Hng and Q. Yan, *Nano Res.*, 2010, **3**, 643–652, DOI: 10.1007/s12274-010-0024-6.

426 T. Zhu, J. S. Chen and X. W. Lou, *J. Mater. Chem.*, 2010, **20**, 7015–7020, DOI: 10.1039/C0JM00867B.

427 Y. Yang, Y. Liang, Z. Zhang, Y. Zhang, H. Wu and Z. Hu, *J. Alloys Compd.*, 2016, **658**, 621–628, DOI: 10.1016/j.jallcom.2015.10.253.

428 F. Y. Cheng, Z. L. Tao, J. Liang and J. Chen, *Chem. Mater.*, 2008, **20**, 667–681, DOI: 10.1021/cm702091q.

429 B. Dunn, H. Kamath and J. M. Tarascon, *Science*, 2011, **334**, 928–935, DOI: 10.1126/science.12127.

430 L. Gu, W. Xie, S. Bai, B. Liu, S. Xue, Q. Li and D. He, *Appl. Surf. Sci.*, 2016, **368**, 298–302, DOI: 10.1016/j.apsusc.2016.01.270.

431 Y. Li, B. Tan and Y. Wu, *Nano Lett.*, 2008, **8**, 265–270, DOI: 10.1021/nl0725906.

432 F. Cheng, Z. Tao, J. Liang and J. Chen, *Chem. Mater.*, 2008, **20**, 667–681, DOI: 10.1021/cm702091q.

433 L. Chun, X. Wu, X. Lou and Y. Zhang, *Electrochim. Acta*, 2010, **55**, 3089–3092, DOI: 10.1016/j.electacta.2010.01.016.

434 S. K. Cheah, E. Perre, M. Rooth, M. Fondell, A. Hårsta, L. Nyholm, M. Boman, T. Gustafsson, J. Lu, P. Simon and K. Edstr€om, *Nano Lett.*, 2009, **9**(9), 3230–3233, DOI: 10.1021/nl9014843.

435 C. M. Doherty, R. A. Caruso, B. M. Smarsly, P. Adelhelm and C. J. Drummond, *Chem. Mater.*, 2009, **21**, 5300–5306, DOI: 10.1021/cm9024167.

436 S. Y. Zeng, K. B. Tang, T. W. Li, Z. H. Liang, D. Wang, Y. K. Wang and W. W. Zhou, *J. Phys. Chem. C*, 2007, **111**, 10217–10225, DOI: 10.1021/jp0719661.

437 L. Liu, Y. Li, S. Yuan, M. Ge, M. Ren, C. Sun and Z. Zhou, *J. Phys. Chem. C*, 2010, **114**, 251–255, DOI: 10.1021/jp909014w.

438 X. H. Huang, J. P. Tu, C. Q. Zhang and F. Zhou, *Electrochim. Acta*, 2010, **55**, 8981–8985, DOI: 10.1016/j.electacta.2010.08.039.

439 G. Zhang, Y. Chen, B. Qu, L. Hu, L. Mei, D. Lei, Q. Li, L. Chen and Q. Li, *Electrochim. Acta*, 2012, **80**, 140–147, DOI: 10.1016/j.electacta.2012.06.107.

440 X. Li, A. Dhanabalan and C. Wang, *J. Power Sources*, 2011, **196**, 9625–9630, DOI: 10.1016/j.jpowsour.2011.06.097.

441 C. Wang, D. Wang, Q. Wang and H. Chen, *J. Power Sources*, 2010, **195**, 7432–7437, DOI: 10.1016/j.jpowsour.2010.04.090.

442 J. H. Pan, Q. Huang, Z. Y. Koh, C. Jin, D. Neo, X. Z. Wang and Q. Wang, *ACS Appl. Mater. Interfaces*, 2013, **5**, 6292–6299, DOI: 10.1021/am401330g.

443 V. Aravindan, P. S. Kumar, J. Sundaramurthy, W. C. Ling, S. Ramakrishna and S. Madhavi, *J. Power Sources*, 2013, **227**, 284–290, DOI: 10.1016/j.jpowsour.2012.11.050.

444 F. Zhang, D. Jiang and X. Zhang, *Nano-Struct. Nano-Objects*, 2016, **5**, 1–6, DOI: 10.1016/j.nanoso.2015.12.002.

445 Q. Wang, Y.-F. Xu, G.-L. Xu, H. Su, S.-Y. Shen, T.-T. Tu and L. Huang, *J. Alloys Compd.*, 2015, **648**, 59–66, DOI: 10.1016/j.jallcom.2015.06.221.

446 P. Lv, H. Zhao, Z. Zeng, C. Gao, X. Liu and T. Zhang, *Appl. Surf. Sci.*, 2015, **329**, 301–305, DOI: 10.1016/j.apsusc.2014.12.170.

447 L. Liu, Y. Guo, Y. Wang, X. Yang, S. Wang and H. Guo, *Electrochim. Acta*, 2013, **114**, 42–47, DOI: 10.1016/j.electacta.2013.09.152.

448 Y. Zhao, Q. Pang, Y. Meng, Y. Gao, C. Wang, B. Liu, Y. Wei, F. Du and G. Chen, *Chem.–Eur. J.*, 2017, **23**, 13150–13157, DOI: 10.1002/chem.201702399.

449 B. Liu, H. Q. Peng, J. Cheng, K. Zhang, D. Chen, D. Shen, S. Wu, T. Jiao, X. Kong, Q. Gao, S. Bu, C. S. Lee and W. Zhang, *Small*, 2019, **15**, 1901545, DOI: 10.1002/smll.201901545.

450 L. Su, W. Jia, L. Zhang, C. Beacham, H. Zhang and Y. Lei, *J. Phys. Chem. C*, 2010, **114**, 18121–18125, DOI: 10.1021/jp107636r.

451 D. Banerjee, U. K. Ghorai, N. S. Das, B. Das, S. Thakur and K. K. Chattopadhyay, *ACS Omega*, 2018, **3**, 6311–6320, DOI: 10.1021/acsomega.8b00798.